1-1-2012

Force and Torque Modeling for the Drilling of Bone for use in Orthopaedic Haptic Simulation Systems

Troy MacAvelia
Ryerson University

FORCE AND TORQUE MODELING FOR THE DRILLING OF BONE FOR USE IN ORTHOPAEDIC HAPTIC SIMULATION SYSTEMS

by

Troy MacAvelia

Bachelor of Engineering, Ryerson University, 2008

A thesis

presented to Ryerson University

in partial fulfillment of the

requirements for the degree of

Master of Applied Science

in the program of

Mechanical Engineering

Toronto, Ontario, Canada, 2012

Author's Declaration

I hereby declare that I am the sole author of this thesis. This is a true copy of the thesis, including any required final revisions, as accepted by my examiners.

I authorize Ryerson University to lend this thesis to other institutions or individuals for the purpose of scholarly research.

I further authorize Ryerson University to reproduce this thesis by photocopying or by other means, in total or in part, at the request of other institutions or individuals for the purpose of scholarly research.

I understand that my thesis may be made electronically available to the public

Abstract

Force and Torque Modeling for the Drilling of Bone for use in Orthopaedic Haptic Simulation Systems

Master of Applied Science, Mechanical Engineering

Ryerson University, Toronto, 2012

Troy MacAvelia

The advent of haptic simulation systems for orthopaedic surgery procedures has provided surgeons with a tool for training and preoperative planning. This is especially true for procedures involving the drilling of bone which requires a great amount of adroitness and experience. One of the potential difficulties with the drilling of bone is the lack of consistent material evacuation from the drill's flutes as the material tends to clog. This clogging leads to significant increases in force and torque experienced by the surgeon which has not been appropriately addressed by current simulation systems. This thesis proposes several force and torque prediction models that account for this phenomenon. Each of the models was calibrated via experimentation and their accuracy was substantiated through an experimental validation process. As an example of the application of the models, a finite element simulation investigating the effect of drilling forces and moments on the dynamic response of a femur bone was studied.

Acknowledgements

I would like to thank my supervisors Dr. Ahmad Ghasempoor and Dr. Farrokh Janabi-Sharifi for their invaluable guidance, encouragement, and support throughout the duration of my graduate studies. I would also like to thank all of the Mechanical and Industrial Engineering Department staff and faculty, as well as the Ryerson community as a whole, for making my six year tenure here as a student educational and enjoyable. Specifically, I would like send special thanks to Lynn Reynolds, Mimi Lam, and Shirley Dacanay for not only their continued encouragement throughout my academic program but also for their friendship.

I received a lot of additional support during this project. I would like to thank Dr. Rad Zdero and the staff at St. Michael Hospital for their donation of human bone specimens and for allowing me to perform experiments using their facilities. I would also like to thank Devin Ostrom and Alan Mechin for providing technical support and advice regarding my experimental set-up and data collection. Additionally, I would like to acknowledge Meisam Salahi and Salman Jan for their hard work and dedication working as research assistances on this project.

I would like to give a big thanks to my colleagues Akbar Assa and Aleksandar Vakanski for their exceptional guidance, assistance, and camaraderie throughout my time as a graduate student in the RMAL laboratory.

Finally, my deepest thanks go to my parents Tim MacAvelia and Jan MacAvelia, my step mother Dr. Fiona Gilchrist, and my brother Jeff MacAvelia for their unyielding support, encouragement, and love throughout my entire academic career.

Contents

Author's Declaration ..... **ii**
Abstract ..... **iii**
Acknowledgements ..... **iv**
List of Tables ..... **viii**
List of Figures ..... **x**
Nomenclature ..... **xv**
1 Introduction **1**
2 Review of the Literature **5**
2.1 Orthopaedic Haptic Simulation Systems 5
2.2 Geometric and Material Properties of Human Bone 7
2.2.1 Cortical Bone 7
2.2.2 Cancellous Bone 8
2.3 Mechanics of Drilling 9
2.4 Drill Thrust Force and Torque Prediction Modeling 11
2.5 The Drilling of Bone 16
2.6 Force and Torque Prediction Modelling for Haptic Rendering 22
3 Drilling of Bone: Force and Torque Modelling **28**
3.1 Cutting Force and Torque Modeling 29
3.2 Chip-evacuation Force and Torque Modeling 31
3.2.1 Empirical Model 33
3.2.2 Artificial Neural Network 38
3.3 Finite Element Modeling 40
3.3.1 Human Femur Bone Model Acquisition 41
3.3.2 Boundary Conditions 42
3.3.3 Load Application 42
3.3.4 Meshing 44
3.3.5 Mesh Sensitivity Analysis 45
4 Experimentation **47**
4.1 Design of Experiments 47

4.1.1 Experiment Classification 47
4.1.2 Experimental Procedure 48
4.1.3 Model Parameter Definition 50
4.1.4 Model Calibration Procedure 52
4.2 Experimental Set-up 54
4.2.1 CNC Drill 54
4.2.2 Transducer and Data Acquisition 55
4.2.3 Drill Bit 56
4.2.4 Bone Specimen 56
4.3 Drill Misalignment 57
4.4 Data Test for Normality 62
4.4.1 Motivation and Procedure 62
4.4.2 Data Collection 63
4.4.3 Median Rank Test 64
4.4.4 Chi Square Test 66
4.5 Data Processing 69
4.5.1 Data Isolation 69
4.5.2 Data Normalization 71
4.5.3 Data Filtering 71
5 Results and Discussion 75
5.1 Empirical Chip-Evacuation Model Calibration 75
5.2 Empirical Chip-Evacuation Model Validation 78
5.3 Empirical Chip-Evacuation Model Sensitivity Analysis 82
5.4 Artificial Neural Network Training 83
5.4.1 Network Neuron Sensitivity Analysis 86
5.5 Artificial Neural Network Validation 89
5.6 Empirical Chip-Evacuation Model Calibration – Human Bone Drilling 92
5.7 Empirical Chip-Evacuation Model Validation – Human Bone Drilling 95
5.8 Comparison of Results 97
5.8.1 Empirical Model versus Artificial Neural Network 97
5.8.2 Drilling of Bovine Bone versus Drilling of Human Bone 98

5.8.3 Empirical Model Comparisons to the Literature 99
5.9 Empirical Model Implementation into FEA Simulation 100
5.9.1 FEA Simulation Solution and Post-Processing 100
6 Conclusion and Future Work 104
6.1 Summary of Contributions 104
6.2 Concluding Remarks 104
6.3 Future Work 105
Appendix A – Basic Calculations 106
Appendix B – Normality Test Data 107
Appendix C – Experimental Data 110
References 115

List of Tables

Table 2-1: Elastic moduli of a typical adult femur cortical bone. Subscript 1: radial direction relative to long axis of bone, 2: tangential direction, 3: longitudinal direction [24]. 8
Table 2-2: Shear moduli of a typical adult femur cortical bone. Subscript 1: radial direction relative to long axis of bone, 2: tangential direction, 3: longitudinal direction [24]. 8
Table 2-3: Poisson's ratio of a typical adult femur cortical bone. Subscript 1: radial direction relative to long axis of bone, 2: tangential direction, 3: longitudinal direction [24]. 8
Table 2-4: Strength of the cortical bone of a human femur [24]. 8
Table 2-5: The ranges of material properties for a typical adult femur cancellous bone [25]..... 9
Table 3-1: Material properties of cortical and cancellous bone used in finite element simulation [24, 25]. 42
Table 4-1: List of selected feed rates and spindle speeds 51
Table 4-2: Chi Square test for normality using the initial cutting force data. 67
Table 4-3: Chi Square test for normality using the exponential constant data. 68
Table 4-4: Summary of low-pass filter tuning parameters based on increasing feed rate. 73
Table 5-1: The results of nonlinear least-squares optimization used to determine the coefficients of friction for all calibration operating parameters. 77
Table 5-2: Coefficients of the power law model. 78
Table 5-3: The operating parameters used for validation experiments. 79
Table 5-4: The coefficients of determination, R^2, for the force and torque models for each of the four validation experiments. 81
Table 5-5: Force and torque prediction model sensitivity to the coefficients of friction μ_f and μ_w. 82
Table 5-6: The experiment operating parameters used to train the ANN. 84
Table 5-7: Operating parameters used for network sensitivity and validation. 87
Table 5-8: The coefficients of determination, R2, for the force and torque network outputs for each of the four validation experiments. 90
Table 5-9: Specification data for each of the 16 human femur bone specimen used for experimentation. 93
Table 5-10: Experiment operating parameters used to calibration of the human bone drilling model. 93
Table 5-11: The results of nonlinear least-squares optimization used to determine the coefficients of friction for the drilling of human bone for all calibration operating parameters. 94
Table 5-12: The constants of the power law model. 94
Table 5-13: The coefficients of determination, R^2, for the force and torque models for each of the two validation experiments. 96
Table 5-14: The maximum deflection at the mid-diaphysis, proximal end, and distal end using the two models. 102

Table 5-15: The maximum equivalent stress at the mid-diaphysis, proximal end, and distal end using the two models. 103
Table B-1: The exponential constant, *p*, and the initial cutting force (F_o) for all normality test data. 107
Table B-2: The initial cutting force and standardized cutting force used for a Chi Square test for normality. 108
Table B-3: The exponential constant, p, and standardized exponential constant used for a Chi Square test for normality. 109

List of Figures

Figure 2-1: Schematic diagram of an orthopaedic haptic simulation system displaying the virtual and real world components. 6
Figure 2-2: Picture of a handheld haptic drilling tool as used in orthopaedic haptic simulation systems [21]. 6
Figure 2-3: Cross-section of a human femur bone indicating the various materials of which it is composed. 7
Figure 2-4: A standard twist drill and associated nomenclature. 9
Figure 2-5: Tool-to-workpiece interaction that occurs during an orthogonal cutting process [27]. 10
Figure 2-6: The various forms of cutting experienced at the different locations of the drill [26]. 11
Figure 2-7: a) Free body diagram of a drill tip displaying the tangential forces, b) Free body diagram of a drill tip displaying the perpendicular and ploughing forces, and c) Area of material contact when cutting [11]. 13
Figure 2-8: Free body diagram of the cutting forces as they act on the tip of a drill bit [10]. 15
Figure 2-9: Experimental results relating feed with a) thrust pressure, b) torque, and c) specific cutting energy using three different types of drill bits [9]. 17
Figure 2-10: Experimental results relating hole depth with a) torque and b) specific cutting energy using a 3.18mm diameter drill bit [9]. 18
Figure 2-11: Experimental results relating the drill's rotational speed with a) thrust force and b) torque [13]. 19
Figure 2-12: Experimental results relating a) spindle speed with feed rate at two different locations of the bone and b) drilling strength and triaxial strength [31]. 20
Figure 2-13: Experimental results indicating the three way relationship between spindle speed, thrust force, and power consumption [32]. 21
Figure 2-14: Pictorial representation of formulation parameters; a) infinitesimally small bone layer thickness, *dx*; b) material transition [12]. 22
Figure 2-15: Experimental results used to validate the proposed model at the exit of the cortical bone [12]. 23
Figure 2-16: The simulated results based on the purposed model for drilling a) unicortical and b) bicortical. The experimental results obtained drilling c) unicortical, and d) bicortical [15]. 25
Figure 2-17: Free body diagram of the forces acting on the tip of a drill bit [16]. 26
Figure 3-1: Drilling thrust force and torque verses depth for the drilling of 6061 T-6 Aluminium alloy at a feed of 0.16 mm/rev and 112 RPM [34]. 28
Figure 3-2: Example of experimental data collected from the drilling of bovine bone. 29
Figure 3-3: Plot comparing Allotta's force prediction model with raw experimental data collected drilling bovine bone. 30

Figure 3-4: Plots comparing Allotta's a) force and b) torque prediction models with raw experimental data collected drilling bovine bone. 31
Figure 3-5: Chip formation resulting in the drilling of a) bovine bone and b) AISI 316 stainless steel. 32
Figure 3-6: The two forms of material removed by drilling bovine bone: a) clogged material and b) evacuated material. 32
Figure 3-7: A drill penetrating cortical bone with the hatched area indicating a differential chip section, *dz'*. 33
Figure 3-8: A cross-section of a typical twist drill bit. 34
Figure 3-9: Force balance on differential bone chip section. 35
Figure 3-10: A single neuron artificial neural network. 39
Figure 3-11: The three solid bodies used to form the model of a human femur bone; a) cancellous bone distal, b) cancellous bone proximal, and c) cortical bone. 41
Figure 3-12: Boundary conditions applied to the femur bone model in ANSYS. 42
Figure 3-13: Applied force and torque locations on the femur bone model: a) mid-diaphysis, b) distal end, and c) proximal end. 43
Figure 3-14: The three common element shapes used for 3D FEA analysis; a) tetrahedral, b) hexahedral, and c) pentahedral. 44
Figure 3-15: A screen shot of the default element shape and size as established by ANSYS. 44
Figure 3-16: A plot of the values obtained via a mesh sensitivity analysis. 45
Figure 3-17: Plot of mesh size vs. maximum deflection indicating the mesh size cut-off value. 46
Figure 4-1: The orthopaedic drill penetrating a cross-section of a bone a) bi-cortically, and b) unicortically. 49
Figure 4-2: The 60x magnification image of the orthopaedic twist drill used for experimentation: a) the face, heel, and root contact lengths, b) the contact length of the wall, c) the cross-section area, and d) the angle between the flute face and cutting plane. 52
Figure 4-3: Experimental set-up depicted: a) schematically and b) pictorially. 54
Figure 4-4: Screen shot of the Microsoft Excel data acquisition user interface. 55
Figure 4-5: A stainless steel, 2.7mm diameter orthopaedic surgical drill bit used for experiments. 56
Figure 4-6: Bovine femur bone specimen loaded in the vice ready for experimentation. 57
Figure 4-7: Drilling coordinate system. 57
Figure 4-8: An example of data collected for x-, y-, and z-axis forces. 58
Figure 4-9: An example of data collected for x-, y-, and z-axis torques. 59
Figure 4-10: Exaggeration of drill axis and sensor axis misalignment. 60
Figure 4-11: Displacement measurements in the x-, y-, and z-directions collected while simulating a drilling experiment. 61
Figure 4-12: Exaggeration of drill shaft axis, sensor axis, and drill path axis misalignment. 62
Figure 4-13: The results of a median rank normality test using initial cutting force data. 65
Figure 4-14: The results of a median rank normality test using the exponential constant data. 65

Figure 4-15: Resulting histogram based on initial cutting force data. 66
Figure 4-16: Resulting histogram based on exponential constant data. 68
Figure 4-17: An example of the raw a) force and b) torque data obtained experimentally. 70
Figure 4-18: An example of a) force and b) torque data after signal isolation. 70
Figure 4-19: An example of a) force and b) torque data after normalizing the signals. 71
Figure 4-20: Simulink schematic of the low-pass band filter used to filter experiential signal data. 73
Figure 4-21: Example of raw experimental a) force and b) torque data signals overlaid by their corresponding filtered signals. 74
Figure 4-22: An example of a complete data set a) before filtering and b) after filtering. 74
Figure 5-1: A complete set of experimental data collected using a feed rate of 2.0mm/sec and a spindle speed of 1500RPM. 76
Figure 5-2: A sample data set with outliers removed collected using a feed rate of 2.0mm/sec and a spindle speed of 1500RPM. 77
Figure 5-3: Trial one of the comparison of experimental validation data versus predicted empirical model for force and torque using a feed rate of 1.75mm/sec and spindle speed of 1250RPM. 80
Figure 5-4: Trial two of the comparison of experimental validation data versus predicted empirical model for force and torque using a feed rate of 1.75mm/sec and spindle speed of 1250RPM. 80
Figure 5-5: Trial one of the comparison of experimental validation data versus predicted empirical model for force and torque using a feed rate of 2.0mm/sec and spindle speed of 1000RPM. 80
Figure 5-6: Trial two of the comparison of experimental validation data versus predicted empirical model for force and torque using a feed rate of 2.0mm/sec and spindle speed of 1000RPM. 81
Figure 5-7: Schematic of the initial design of the neural network. 84
Figure 5-8: Plot of mean square error versus time for neural network training, validation, and testing. 85
Figure 5-9: Plots of the linear regression results for network training, validation, testing, and the total. 85
Figure 5-10: A schematic of a multi-neuron hidden layer artificial neural network. 86
Figure 5-11: Plots of neuron sensitivity validation displaying the results of a) a single neuron network using validation parameters 1, b) a ten neuron network using validation parameters 1, c) a single neuron network using validation parameters 2, and d) a ten neuron network using validation parameters 2. 88
Figure 5-12: Plot depicting validation MSE versus number of hidden layer neurons using validation 1 parameters. 89
Figure 5-13: Plot depicting validation MSE versus number of hidden layer neurons using validation 2 parameters. 89

Figure 5-14: Trial one of the comparison of experimental validation data versus the predicted artificial neural network output for force and torque using a feed rate of 1.75mm/sec and spindle speed of 1250RPM. 90
Figure 5-15: Trial two of the comparison of experimental validation data versus the predicted artificial neural network output for force and torque using a feed rate of 1.75mm/sec and spindle speed of 1250RPM. 91
Figure 5-16: Trial one of the comparison of experimental validation data versus the predicted artificial neural network output for force and torque using a feed rate of 2.0mm/sec and spindle speed of 1500RPM. 91
Figure 5-17: Trial two of the comparison of experimental validation data versus the predicted artificial neural network output for force and torque using a feed rate of 2.0mm/sec and spindle speed of 1500RPM. 91
Figure 5-18: Human femur bone specimen loaded in to vice prior to experimentation. 92
Figure 5-19: Trial one of the comparison of experimental validation data versus the predicted empirical model for force and torque using a feed rate of 2.0mm/sec and spindle speed of 1250RPM. 95
Figure 5-20: Trial two of the comparison of experimental validation data versus the predicted empirical model for force and torque using a feed rate of 2.0mm/sec and spindle speed of 1250RPM. 95
Figure 5-21: Raw experimental force and torque data with a comparision of the empirical model and ANN results. 97
Figure 5-22: Plot comparing the experimental results of the drilling of bovine bone with the output of several thrust force prediction models. 100
Figure 5-23: The result of the FEA simulation using the presented force and torque models while drilling mid-diaphysis. 101
Figure 5-24: The result of the FEA simulation using Allotta's [12] force and torque models while drilling mid-diaphysis. 102
Figure 5-25: Plot of the resulting maximum equivalent stress comparing dynamic loading versus static loading. 103
Figure C-1: Processed experimental data for the drilling of bovine bone using a feed rate of 1.0mm/sec and a spindle speed of 1000RPM. 110
Figure C-2: Processed experimental data for the drilling of bovine bone using a feed rate of 1.5mm/sec and a spindle speed of 1100RPM. 110
Figure C-3: Processed experimental data for the drilling of bovine bone using a feed rate of 1.5mm/sec and a spindle speed of 1250RPM. 111
Figure C-4: Processed experimental data for the drilling of bovine bone using a feed rate of 1.75mm/sec and a spindle speed of 1500RPM. 111
Figure C-5: Processed experimental data for the drilling of bovine bone using a feed rate of 2.0mm/sec and a spindle speed of 1500RPM. 112

Figure C-6: Processed experimental data for the drilling of human bone using a feed rate of 1.75mm/sec and a spindle speed of 1000RPM. 112
Figure C-7: Processed experimental data for the drilling of human bone using a feed rate of 1.75mm/sec and a spindle speed of 1250RPM. 113
Figure C-8: Processed experimental data for the drilling of human bone using a feed rate of 2.0mm/sec and a spindle speed of 1000RPM. 113
Figure C-9: Processed experimental data for the drilling of human bone using a feed rate of 2.0mm/sec and a spindle speed of 1500RPM. 114
Figure C-10: Processed experimental data for the drilling of human bone using a feed rate of 2.25mm/sec and a spindle speed of 1500RPM. 114

Nomenclature

a	Drill's feed
a_0-a_3	Coefficients of the power law
A	Cross-sectional area of the hole
b	Neural network bias
b_0-b_3	Coefficients of the power law
B	Feed anticipated at a thrust pressure of 1 N/mm^2
C	Length of chisel edge
C'	Experimental Constant
C_1	Experimental Constant
C_2	Experimental Constant
C_D	Experimental Constant
C_f	Experimental Constant
C_N	Experimental Constant
C_T	Experimental Constant
d'	Drill bit web thickness
dw	Surface element thickness
dx	Infinitesimally small bone layer thickness
dz'	Differential chip section
D	Drill bit diameter
D'	Experimental Constant
f	Drill feed rate
f_{pass}	Pass frequency

f_s	Sampling frequency
f_{stop}	Stop frequency
F	Drilling thrust force
$F_{i,j}^{H}$	Horizontal force component at voxel *i,j*
$F_{i,j}^{T}$	Tangential force component at voxel *i,j*
$F_{i,j}^{V}$	Vertical force component at voxel *i,j*
F_0	Cutting force
F_1	Orthogonal cutting force
F_2	Chisel edge ploughing force
F_c	Chip-evacuation force
F_{exp}	Experimental force signal
F_{ff}	Frictional force caused by flute face
F_{fn}	Force normal to flute face
F_{fwi}	Frictional force between bone chip and wall of the hole
F_{hf}	Frictional force caused by flute heel
F_{hn}	Force normal to flute heel
F_H	Principle cutting force
F_{Model}	Chip-evacuation force model
F_p	Perpendicular cutting force
F_{rad}	Radial force component
F_{rf}	Frictional force caused by flute root
F_{rn}	Force normal to flute root
F_t	Tangential cutting force
F_{tang}	Tangential force component

F_{thrust}	Thrust force component
F_T	Transverse force
F_V	Vertical force
F_{wf}	Frictional force caused by the wall
F_{wn}	Force normal to the wall of the hole
g	Neural network output
h	Neural network input
H_B	Brinell hardness
j	Number of discretized bins
k	Number of parameters estimated from the data
K_H	Horizontal linear function of radius from surface element
K_T	Tangential linear function of radius from surface element
K_V	Vertical linear function of radius from surface element
l	Length of the drill tip cone
l_f	Length of flute face
l_h	Length of flute heel
$l_{i,j}$	Distance of element from rotational centre for bending
l_r	Length of flute root
l_w	Length of contact area between chip and wall of the hole
m	Web thickness to diameter ratio
m'	Experimental Constant
n	Number of cutting lips
N	Drill's spindle speed
p	Exponential constant used to test for normality
P	Axial thrust pressure

P_o	Initial axial cutting pressure
q	Chisel edge length to drill diameter ratio
r	Radial distance from the drill's axis of rotation
$r_{i,j}$	Distance of element from the q-axis
R	Radius of the drill bit
R^2	Coefficient of determination
R_a	Unitary ultimate tensile load
s	Neural network net input
S	Cross-sectional area of drill flute
S_μ	Model sensitivity
S_{μ_f}	Model sensitivity to the coefficient of friction μ_f
S_{μ_w}	Model sensitivity to the coefficient of friction μ_w
SS_{err}	Residual sum of squares
SS_{tot}	Total sum of squares
t	Depth of cut
T	Cutting torque
T_0	Cutting torque
T_c	Chip-evacuation torque
T_{exp}	Experimental torque signal
T_{Model}	Chip-evacuation torque model
T_{radius}	Radial torque component
T_{tang}	Tangential torque component
T_{thrust}	Thrust torque component
u	Specific cutting energy
u_1	Specific cutting energy of cortical bone

u_2	Specific cutting energy of cancellous bone
v	Tool velocity in orthogonal cutting
w	Neural network weight
x'	Sensitivity of penetrating ability
x_1	Experimental Constant
x_2	Experimental Constant
x_b	Depth of remaining material
y	Observed data set value
$\overline{y}$	Arithmetic mean
$\hat{y}$	Predicted data set value
y'	Experimental Constant
y_1	Experimental Constant
y_2	Experimental Constant
z	Ratio relating drill depth to diameter
z'	Distance from material surface to drill tip
α	Rake angle
α_p	Angle formed between the perpendicular cutting force and half the orthogonal cutting force
β	Drill bit point angle
η	Constant relating axial pressure to lateral pressure
θ	Angle formed between the flute face and plane formed across the flute
$\theta_{i,j}$	Half the point angle
μ_f	Coefficient of friction between bone chip and drill flute
μ_w	Coefficient of friction between bone chip and wall of the hole
v	Chi square degrees of freedom

ρ	Material density
φ	Shear angle
ω	Rotational velocity
2D	Two Dimensional
3D	Three Dimensional
ANN	Artificial Neural Network
BMD	Bone Mineral Density
CL	Confidence Limit
CNC	Computer Numerically Controlled
CT	Computer Tomography
FE	Finite Element
FEA	Finite Element Analysis
GUI	Graphic User Interface
ISA	Industrial Standard Architecture
MRI	Magnetic Resonance Imaging
MSE	Mean Square Error

1 Introduction

Technological and procedural advancements in the field of medicine have made many surgical practices achievable today that only a few years ago were considered impossible. The downside to these innovations is the large emphasis they have placed on the experience and training of the surgeons as the procedures have increased in complexity. This is especially true for orthopaedic surgeons as surgical practices range greatly in difficulty. Orthopaedic surgeries encompass seemingly basic procedures of anchoring fixation plates to long bones to more advanced spinal procedures where there exists the potential of nerve damage [1]. Additionally, unlike surgeons in other fields of medicine, orthopaedic surgeons often have to handle bulky tools and work on the patient at skewed and irregular positions. Finally, many orthopaedic practices involve the cutting or drilling of bone which requires a great amount of dexterity as bone does not respond like many other materials [2-5]. Many of these skills can only be learned through repetitious practice and it is for this reason that the field of orthopaedics places a great deal of importance on surgeon training.

A surgeon's training initiates in residency where the surgeon begins to hone their skills through an array of different methods including: mock surgeries on animals, dissection of cadavers, and even practices directly in the operating room on live patients [6]. Unfortunately, many financial, ethical, and accessibility issues arise with these current training methods. To overcome similar adversities, various other industries have developed virtual environments where their practitioners can gain the experience they need without incorporating the costs and risks associated with real life training [7]. By removing many of the financial, ethically, and availability issues associated with traditional surgical training practices, a simulated training environment would provide an ideal learning tool for novice orthopaedic surgeons.

The nature of virtual simulation is to accurately reproduce the human senses associated with the act being simulated. As this applies to surgical simulation, the main two human senses of interest are sight and touch. For sight, the surgeon must physically see the effect of their hands and tools as they manipulate different areas of the environment and ultimately make contact with different parts of the virtual patient's anatomy. This involves a graphical representation of the

area of interested of the virtual patient as well as surgical tools connected to the simulator that can be physically manipulated by the surgeon and reflected in the virtual environment. For touch, the surgeon must be provided with a physical response or feedback based on the virtual tasks being conducted. This requires that the surgeon's tools be grounded to the simulator in order to provide meaningful force and/or torque response based on the mechanics of the surgical procedure being performed. The field of research dealing with the sense of touch is referred to as haptics.

Several orthopaedic haptic simulation systems have been developed in recent years and are currently being utilized by the medical industry. Most of these systems are specifically tailored to one of the two major bone removal techniques of orthopaedic surgery: sawing [8] and drilling [14]. As is the nature of any haptic system, the precision of its output feedback is of the utmost importance. Many of the systems currently available on the market strive to generate a suitable force and torque response based on inherent operating parameters such as tool velocity. The modeling of this feedback is relatively straightforward in systems concerned with the sawing of bone as a great amount of literature exists on the sawing of metals and woods; these concepts have been appropriately modified to address the sawing of bone. Unfortunately, this is not the case with systems focused on drilling procedures as chip-evacuation becomes an issue. Unlike metals, the cutting of bone results in the formation of discontinuous chips which, as they attempt to evacuate the flutes, tend to cluster together and block the removal of additional material [9]. This phenomenon of bone clogging has yet to be properly modeled for the use in orthopaedic haptic simulation systems and is the focus of our contribution.

As only a few studies have been conducted on the subject of bone drilling, exploration in the area of drilling metals has provided a solid foundation for expanding these concepts to the drilling of bone. Early models were developed for the predication of thrust force and torque for the drilling of metals through orthogonal cutting principles with shearing as the means of material failure [10, 11]. Later works attempted to adopt these models to the cutting of bone by using appropriate material properties and by accounting for the transition zone between cortical and cancellous bone [12]. Additional research focused on the interrelationship among thrust pressure, torque, feed rate, spindle speed, and specific cutting energy when drilling bone [9, 13]. These studies suggested that the above parameters could be described by a power function.

Furthermore, the effect of drill bit flute clogging was examined and identified as a serious concern when drilling bone and it was shown experimentally that drill flute clogging caused a significant increase in drilling thrust pressure, torque, and specific cutting energy as the drill progressed through the bone [9].

In more recent years, several orthopaedic haptic simulation systems have been developed and implemented utilizing force/torque prediction models to provide the required feedback. The prediction model developed in [12] was employed in one such simulation system and provided a value for force and torque as a function of geometric and material constants, and feed rate [14]. In another work, an empirical formulation based exclusively on spindle speed, feed rate, and material density was utilized to generate haptic feedback [15]. Later, another haptic platform was created that employed a spring-damper model to provide predicted force/torque feedback [15]. Finally, in another work, a unique analytic formulation was developed to provide force response. This model provided a force output based on the penalty method which accounted for the depth of the drill bit but was independent of the operating parameters [16].

The shortcomings of each model developed to date are that they all make the assumption that the cutting force and torque are constant and are, thus, independent of time and hole depth. In addition, each model is lacking any effect due to flute clogging. The omission of drilling dynamics and the clogging effect from the force feedback models presented in the literature has motivated this study to improve the accuracy of force/torque prediction in drilling of bone.

The main contribution of this work is to develop more complete force/torque models that account for interaction dynamics and the discontinuous chip clogging effect present during the drilling of bone. Model parameters are identified via a set of experiments using non-linear least squares regression and power law formulation. The developed models are also validated through a set of additional experiments. Several R-squared values are presented as measurement of the models' precision. This new formulation will provide more accurate and meaningful sensory feedback for orthopaedic haptic simulation systems.

The organization of this report is as follows. An investigation into the pertinent literature will be presented in Chapter 2. Chapter 3 will develop an empirical model for predicting chip-evacuation force and torque for the drilling of bone and outline the procedure for its calibration.

Additionally, artificial neural network and finite element models will be established in this chapter. Chapter 4 will explain the experimental setup and procedure for the calibration and validation of the empirical and neural network models for the drilling of bovine bone. Also, Chapter 4 will present the results of a test for normality and the data processing procedures. The results of the empirical and neural network models' calibration and validation for the drilling of bovine bone will be presented in Chapter 5. Chapter 5 will also deliver the results of calibration and validation experiments for empirical models developed for the drilling of human bone. This will be followed by a comparison of all the presented models and an assessment of their improvement over currently used models from the literature. The final section of Chapter 5 will apply the presented models in a finite element simulation where the resulting deflection and equivalent stress will be revealed. This report will conclude with Chapter 6 which will summarize all of the findings and contributions of our research as well as propose future works in this area of study.

2 Review of the Literature

The objective of this research was to develop force and torque prediction models for the drilling of bone to be used for orthopaedic surgery haptic simulation systems. An overview of current orthopaedic haptic simulation systems was presented including the general requirements and limitations of systems presently available. The general make-up and material structure of human bones were explored highlighting the material and geometric properties. The drilling process was reviewed which included the drilling of metals and bone. Finally, state of the art force and torque models used in current orthopaedic haptic simulation systems were investigated.

2.1 Orthopaedic Haptic Simulation Systems

The advent of haptic simulation systems for orthopaedic surgery procedures has provided surgeons with an excellent tool for training and preoperative planning purposes. This is especially true for practices involving the drilling of bone as execution of these procedures generally requires a great amount of adroitness and experience due to difficulties arising from vibration and drill bit breakage [16]. To properly simulate these procedures in a virtual environment, two of the five senses need to be accurately duplicated: the sense of sight and the sense of touch. For this reason, these are the two major areas of focus of current orthopaedic simulation systems. In the literature these two topics have been categorized into graphic rendering (the accurate replication of sight) and haptic rendering (the accurate replication of touch). Once rendered, the visual image and haptic sensation are relayed from the digital environment to the real world via feedback hardware. Bridging these two forms of rendering is a third area of interest – collision detection. A schematic of the overall system is depicted in Figure 2-1.

Of the three areas of interest in orthopaedic simulation systems, a much greater emphasis has been placed on graphic rendering and collision detection as these simulation systems require real-time processing where graphics computation can be bulky [14]. This work focuses on the contributions to haptic rendering and, thus, graphic rendering and collision detection will not be further discussed. For additional information regarding graphic rendering and collision detection refer to [14-20].

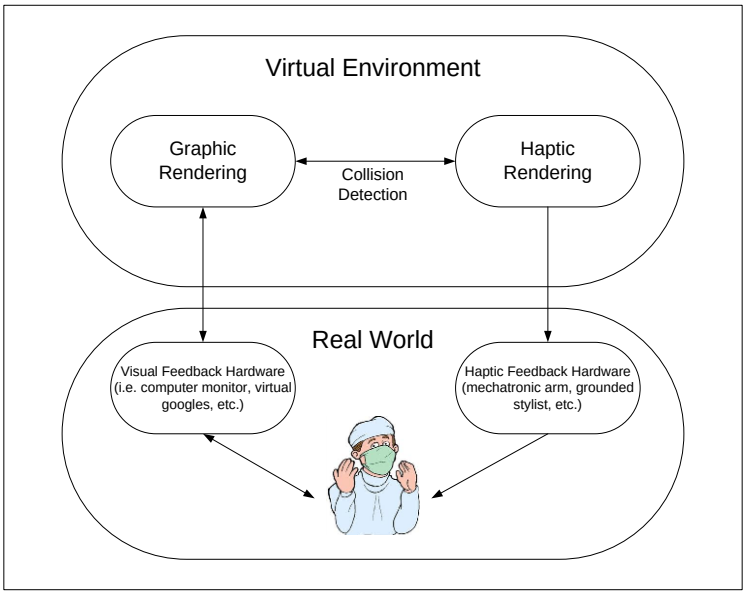

Figure 2-1: Schematic diagram of an orthopaedic haptic simulation system displaying the virtual and real world components.

The haptic rendering process for orthopaedic surgical simulation systems has received much less attention from research groups than that of graphic rendering process. Essentially, a collision detection algorithm determines if tool-to-bone contact has occurred in the virtual world and, if so, provides a force response in the real world through some form of haptic hardware. Generally, this haptic hardware is in the form of a stylist pen or resembles the surgical tool in which the system is simulating. An example of a haptic tool being used in simulation is shown in Figure 2-2.

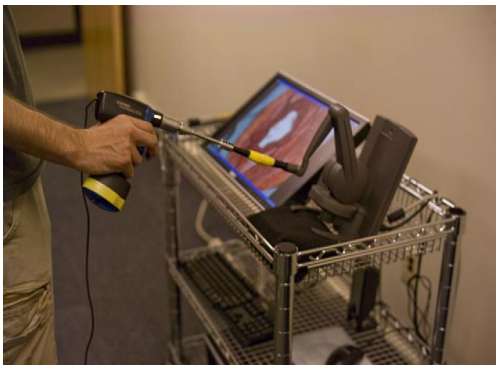

Figure 2-2: Picture of a handheld haptic drilling tool as used in orthopaedic haptic simulation systems [21].

The magnitude of the force delivered to the haptic tool is determined by a force prediction model which interprets the user inputs, such as tool velocity and location, and calculates the

appropriate force response. To provide meaningful feedback it is crucial that the force prediction model providing the haptic response is accurate. The force prediction models utilized by various haptic simulation systems currently available will be discussed at length later in this chapter.

2.2 Geometric and Material Properties of Human Bone

Bones are the firm organs that make up the skeleton and come in a large variety of shapes and sizes. They are both strong and light in weight. Each bone is composed of two main types of bone mineral: Compact (cortical) bone and Trabecular (cancellous) bone. Figure 2-3 displays a picture of a typical bone cross-section highlighting the locations of the cortical and cancellous bone. Since both of these materials vary in structure and density, bone is considered to be an anisotropic, heterogeneous material [22]. With that being said, many experimentally determined approximations have been substantiated for the material properties of both cortical and cancellous bone.

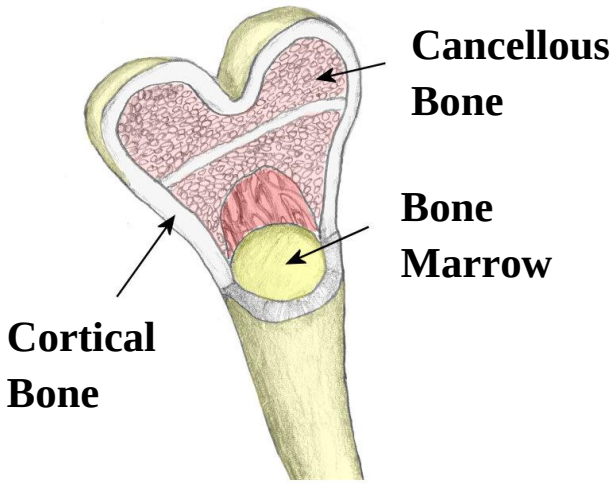

Figure 2-3: Cross-section of a human femur bone indicating the various materials of which it is composed.

2.2.1 Cortical Bone

The cortical bone is composed mainly of the mineral hydroxyapatite (compact bone) tissue which forms the hard outer layer of the bone [23]. The thickness of this outer layer varies depending on which bone, the location on the bone, as well as, the age, sex, and weight of the patient. The cortical bone provides the bone with its strength and acts to protect the marrow, blood vessels, cancellous bone, etc. inside. As the name compact bone would suggest, cortical bone has low porosity (5-30%) and accounts for 80% of the total bone mass of an adult skeleton

[23]. Wet cortical bone has a density of 1990 kg/m^3. The mechanical properties of elastic moduli, shear moduli, and Poisson's ratio of a typical human femur cortical bone are presented in Tables 2-1, 2-2, and 2-3, respectively. Additionally, Table 2-4 displays the strength properties of a human femur cortical bone.

Modulus of Elasticity	Femur Tension[GPa]	Femur Compression [GPa]
E_1	12.0	11.7
E_2	13.4	11.7
E_3	20.0	18.2

Table 2-1: Elastic moduli of a typical adult femur cortical bone. Subscript 1: radial direction relative to long axis of bone, 2: tangential direction, 3: longitudinal direction [24].

	Shear Modulus of Elasticity [GPa]
G_{12}	12.0
G_{13}	13.4
G_{23}	20.0

Table 2-2: Shear moduli of a typical adult femur cortical bone. Subscript 1: radial direction relative to long axis of bone, 2: tangential direction, 3: longitudinal direction [24].

Poisson's Ratio	Femur Tension	Femur Compression
ν_{12}	0.38	0.63
ν_{13}	0.22	-
ν_{23}	0.24	-
ν_{21}	0.42	0.63
ν_{31}	0.37	0.38
ν_{32}	0.35	0.38

Table 2-3: Poisson's ratio of a typical adult femur cortical bone. Subscript 1: radial direction relative to long axis of bone, 2: tangential direction, 3: longitudinal direction [24].

Mode	Orientation	Breaking Strength [MPa]	Yield Stress [MPa]	Ultimate Strain
Tension	**Longitudinal**	133	114	0.031
	Tangential	52	-	0.007
Compression	**Longitudinal**	205	-	-
	Tangential	130	-	-
	Shear	67	-	-

Table 2-4: Strength of the cortical bone of a human femur [24].

2.2.2 Cancellous Bone

Cancellous bone is composed of interconnected irregular arrays of plate- and rod-like elements called trabeculae [23]. The spaces between the trabeculae arrays are filled with bone marrow. The cancellous bone accounts for the remaining 20% of the overall bone mass but occupies nearly 10 times more surface area than that of the cortical bone. Cancellous bone is

highly porous with a porosity of 30-90% [23]. Since cancellous bone is highly heterogeneous, only ranges of mechanical and strength properties have been reported. The material property ranges for a typical adult femur are presented in Table 2-5.

Material Property	Range	Mean	Standard Deviation
Wet Apparent Density [g/cm^3]	0.14-1.00	0.50	0.16
Modulus of Elasticity [GPa]	0.044-1.531	0.389	0.270
Ultimate Strength [MPa]	0.56-22.9	7.56	4.00

Table 2-5: The ranges of material properties for a typical adult femur cancellous bone [25].

2.3 Mechanics of Drilling

A vast amount of research has been done in the past several decades in examining the material removal process of drilling. Drilling is a machining process in which a revolving cutting tool is fed along its axis of rotation into a stationary workpiece producing a hole [26]. During the drilling process, material is removed via two principle modes: orthogonal cutting along the cutting lips and ploughing (occurring along the chisel edge located at the drill bit's tip) [11]. Figure 2-4 depicts a standard twist drill and the general drill bit nomenclature.

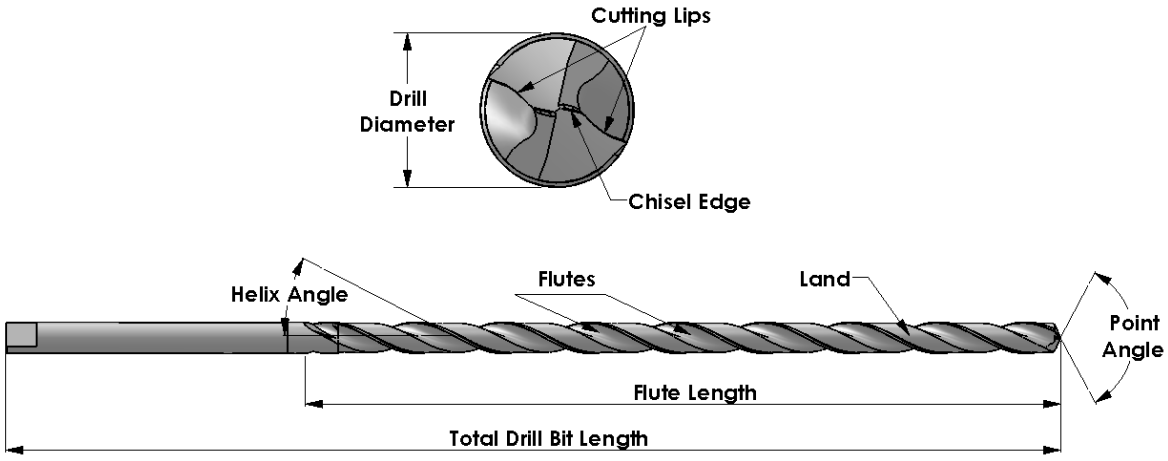

Figure 2-4: A standard twist drill and associated nomenclature.

Orthogonal cutting is a simple-to-analyse two-dimensional material removal process utilized mainly in milling, planing, and lathing operations. Orthogonal cutting occurs when the cutting edge is perpendicular to the relative velocity between the workpiece and tool [26]. During

orthogonal cutting, shear is the main means of material failure [11]. Figure 2-5 displays the basic tool-to-workpiece interaction experienced during orthogonal cutting where v is the velocity of the tool, α is the rake angle, φ is the shear angle, and t is the depth of cut. Notice the primary shear zone indicated in the figure. It is at this shear zone along the length of the cutting lips where the majority of the force is required to remove the material.

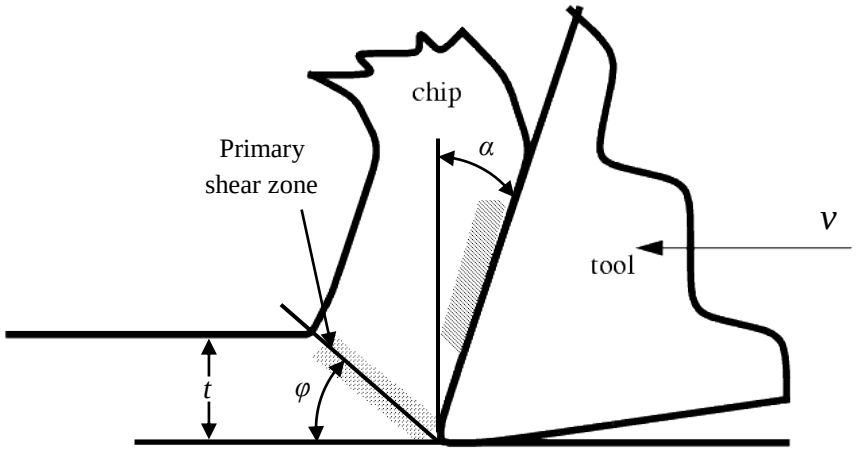

Figure 2-5: Tool-to-workpiece interaction that occurs during an orthogonal cutting process [27].

Ploughing tends to displace material more than completely remove or 'cut' it. The act of chisel edge ploughing, forces the material sideways in a similar fashion as seen during a hardness test [11]. The ploughed material is then in the path of the cutting lips and is removed via orthogonal cutting.

The removed material flows along the drill bit's flute before being evacuated outside the material surface. The flow direction of the material is dependent on the helix angle of the flute. The consistency of the material flow is quite predicable and continual in ductile materials, such as most metals, since the material is removed as a continuous chip. On the other hand, materials that are brittle in nature, such as bone, produce discontinuous chips and have a tendency to bunch together and inhibit consistent material flow. This phenomenon of drill bit clogging will be discussed later in this chapter.

The process of drilling is considerably complex to analyse due to variations of the rake angle, α, along the radius of the drill bit [11]. Standard drill bit cutting lips are designed in such a way as to have large positive rake angles towards the outer radius of the bit. This angle decreases as it

moves along the cutting lips. Eventually, the angle decreases to the point where it becomes a negative rake angle before the cutting lips are terminated at the chisel edge. Figure 2-6 displays the different cutting action experienced as the material moves across the cutting lips and is pushed aside by the chisel edge. In this figure, a positive rake angle along the cutting lips towards the outside radius of the drill bit (view AA) can be observed. As the cutting lips move toward the centre of the drill bit, the rake angle becomes negative (view BB). View CC displays the action of ploughing as the material is being pushed aside.

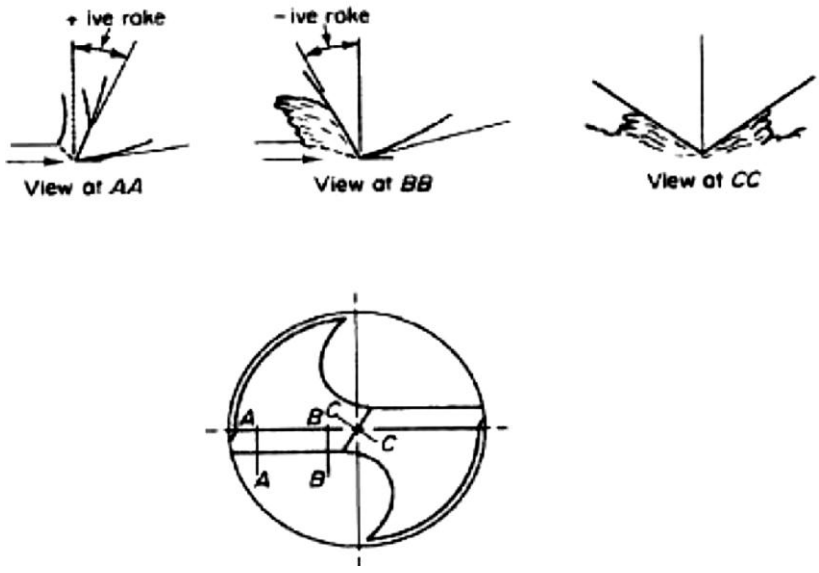

Figure 2-6: The various forms of cutting experienced at the different locations of the drill [26].

2.4 Drill Thrust Force and Torque Prediction Modeling

Over the years there have been many circumstances where it has been deemed advantageous to estimate the thrust force and/or torque experienced while drilling. Of these, most were developed to aide in the drilling of metals in a manufacturing environment. Thrust force and torque prediction models allowed manufacturing engineers to optimize energy consumption, analyse tool wear, optimize tool speeds, increase overall productivity, etc. More recently, with the advancement of surgical simulation systems, it has been necessary to use the similar models as force/torque estimations for haptic feedback.

Early pioneers in the field manufacturing engineering determined that, to describe the drilling process, it was helpful to define a material constant called *specific cutting energy*. Specific cutting energy is defined as the amount of energy required to remove a single unit volume of a

specific material and is reported in units of pressure (i.e. N/mm^2) [11]. It has been reported that specific cutting energy is analogous to Brinell hardness in that they are both influenced by similar properties. It has been further shown that specific cutting energy and Brinell hardness are proportional to one another over a small range of workpiece metals [9]. Specific cutting energy, *u*, is defined mathematically, in general, as:

$$u = \frac{8T}{aD^2}\ , \tag{2.1}$$

where *T* is the cutting torque (determined by measuring the electric power output), *a* is the drill's feed [mm/revolution], and *D* is the drill bit diameter.

Recall that the two principle methods of material removal during the drilling process are orthogonal cutting along the cutting lips and chisel edge ploughing. It is at these two locations on the drill bit that the entire cutting force and torque required to remove the material is generated. Figures 2-7a and 2-7b display two free body diagrams of the forces as they act on the tip of a drill bit. Represented in this figure are the tangential cutting forces, F_t, the perpendicular cutting forces, F_p, the force resulting from orthogonal cutting, F_1, and the force resulting from chisel edge ploughing, F_2. It was shown that these forces could be represented mathematically as follows [11]:

$$F_t = u\left(\frac{D}{2}\right)\left(\frac{a}{2}\right). \tag{2.2}$$

The couple created by F_t separated by half the diameter is solely responsible for the cutting torque, *T*, as:

$$T = \frac{uD^2a}{8}\ . \tag{2.3}$$

As it can be seen from Figure 2-7b, the thrust force is the summation of the two forces F_1 and F_2. It was reported that these forces could be found using the following formulation [11]:

$$F_1 = \frac{F_t}{F_p}\cos\alpha_p\, 2u\left(\frac{D}{2}\right)\left(\frac{a}{2}\right), \tag{2.4}$$

where α_p is defined in Figure 2-7b and F_t/F_p was shown to have a probable value of 0.5 to 1.0.

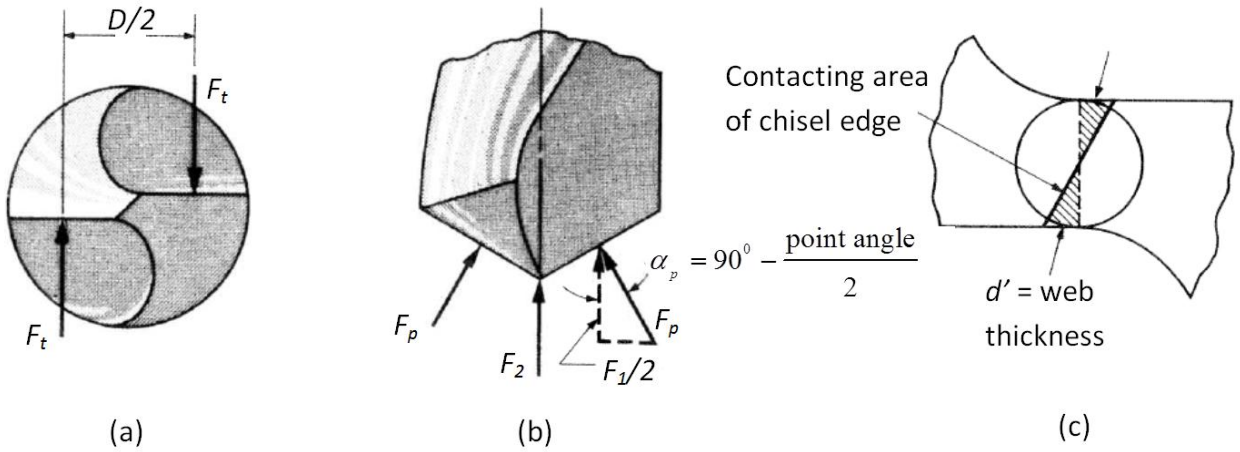

Figure 2-7: a) Free body diagram of a drill tip displaying the tangential forces, b) Free body diagram of a drill tip displaying the perpendicular and ploughing forces, and c) Area of material contact when cutting [11].

The ploughing force, F_2, is much more difficult to calculate since the portion of the chisel edge contacting the material is troublesome to estimate [26]. It has been reported that the web thickness, *d'*, can be approximated as 0.2D for drills less than 1/8" in diameter and as little as 0.1D for drills greater than 1" in diameter. Using this assumption and recalling that the ploughing force acts in a similar way as a Brinell hardness test, H_B, the following formulation was reported for F_2 [11]:

$$F_2 = m\frac{\pi\left(d'\right)^2}{4}H_B, \tag{2.5}$$

where H_B is the Brinell hardness number of the material being drilled and *m* ranges from 0.1 to 0.2. Summing Eqs. 2.4 and 2.5 results in a final formulation for the thrust force, *F*, as follows [11]:

$$F = F_1 + F_2 = \frac{F_t}{F_p}\cos\alpha_p 2u\left(\frac{D}{2}\right)\left(\frac{a}{2}\right) + m\frac{\pi\left(d'\right)^2}{4}H_B. \tag{2.6}$$

Later work developed force/torque prediction models using empirical relations. It was established that drill cutting force and torque were dependent on the feed rate, spindle speed, and diameter of the drill bit [26]. This led to the following empirical formulations for force and torque [26]:

$$F = C_1 a^{x_1} D^{y_1}, \tag{2.7}$$

$$T = C_2 a^{x_2} D^{y_2} . \quad (2.8)$$

Here, C_1, C_2, x_1, x_2, y_1, and y_2 are all experimentally established constants that depend on the material and drill bit geometry [26].

A similar approach for a variety of steels was taken by researchers in [10]. This research showed that the rake angle and how it changed along the chisel edge was an important consideration. Using a dimensional analysis approach, the following semi-analytical equations were reported for steel [10]:

$$\frac{F}{D^2 H_B} = \frac{0.15 a^{0.8}}{D^{1.2}} \left[\frac{1-q}{(1+q)^{0.2}} + 2.2 q^{0.8} \right] + 0.068 q^2 , \quad (2.9)$$

$$\frac{T}{D^3 H_B} = \frac{0.082 a^{0.8}}{D^{1.2}} \left[\frac{(1-q)^2}{(1+q)^{0.2}} + 3.2 q^{1.8} \right], \quad (2.10)$$

where

$$q = \frac{C}{D} = \frac{\text{length of chisel edge}}{\text{drill diameter}} . \quad (2.11)$$

The most recent works in this area of research takes advantage of finite element (FE) techniques in [28]. It was shown that the cutting forces along the cutting lips could be represented as a sequence of oblique sections while cutting occurring at the chisel edge region could be characterized as orthogonal cutting [28]. By doing so, three drilling forces required to remove material: the principle (cutting) force (F_H), the transverse force (F_T), and the vertical (thrust) force (F_V) were defined. Figure 2-8 displays these forces as the act on the drill tip. Additionally, it was suggested that the principle, transverse, and vertical forces were only the forces required to remove the material and would need to be broken down to properly predict the forces experience by the drill [28]. These forces are also displayed in Figure 2-8 as the tangential force (F_{tang}), the radial force (F_{rad}), and the thrust force (F_{thrust}). The tangential, radial, and thrust forces were defined as [28]:

$$F_{tang} = F_H , \quad (2.12)$$

$$F_{thrust} = F_T \cos\left(\frac{\beta}{2}\right) + F_V \frac{\sqrt{\left(r^2 - \left(\frac{b'}{2}\right)^2\right)}}{r} \sin\left(\frac{\beta}{2}\right), \quad \textbf{(2.13)}$$

$$F_{rad} = F_T \frac{\sqrt{\left(r^2 - \left(\frac{b'}{2}\right)^2\right)}}{r} \sin\left(\frac{\beta}{2}\right) - F_V \cos\left(\frac{\beta}{2}\right). \quad \textbf{(2.14)}$$

Here, r is the radial distance from the drill's axis, and β is the point angle. It was concluded that F_{thrust} was responsible for the drill thrust force, F_{tang} produced the drill torque, and F_{rad} cancelled each other as a result of the cutting lip symmetry [28]. For each section along the cutting lips, an Eulerian FE model was used to replicate the cutting forces. Once all the cutting forces had been determined, each section was combined to establish the overall thrust force and torque [28]. The above model showed good correlation with experimental results.

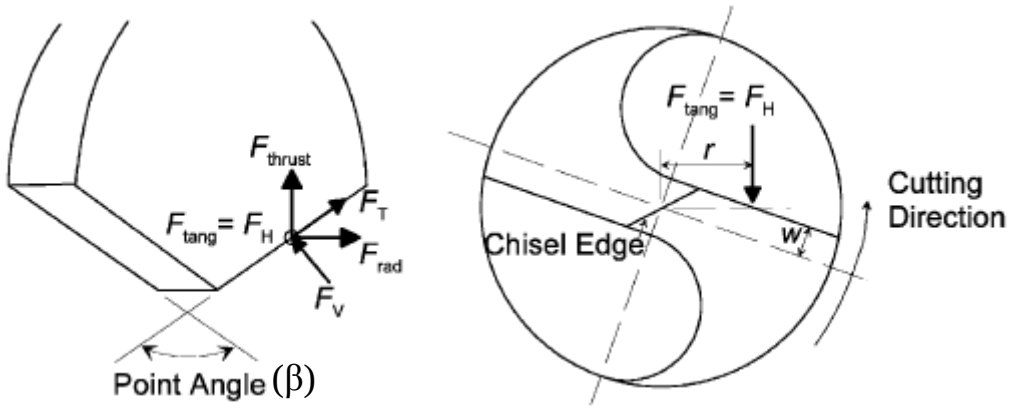

Figure 2-8: Free body diagram of the cutting forces as they act on the tip of a drill bit [10].

It should be noted that all the force and torque estimates presented thus far are independent of hole depth. This would suggest that the cutting forces and torques remain constant throughout the entire cutting of the hole. This assumption, as it will be shown later, only holds for ductile materials such as metals and plastics. The cutting of ductile materials produces a continuous chip flow along the drill flutes; this allows material to flow freely, without hindrance. On the other hand, the cutting of brittle materials generates discontinuous chips which tend to cluster together in the drill's flutes. This chip clustering or *clogging* results in increased thrust force and torque

resistance as the material continues to build up inside the drill's flutes [29]. The drilling of bone, being a brittle material, is very susceptible to this material flute clogging.

2.5 The Drilling of Bone

A majority of the literature that investigated drilling bone used the well-defined theorems that have been previously developed for drilling metal. The exploration in the area of drilling metals is extensive. This has provided a strong foundation for expanding these concepts to drilling of bone. That being said, it should be noted that there are significant differences between drilling metal and drilling bone. One of the most obvious of these differences is their respective material properties. Metals, in general, are dense and ductile whereas cortical bone tends to be slightly porous and brittle. Additionally, metals have much greater shear and yield strengths than cortical bone. Another significant difference is that metals are generally considered to be isotropic whereas cortical bone is considered to be highly anisotropic making it very difficult to predict how it will react when being drilled.

Initial research in the area of bone drilling focused on gathering experimental results which showed the interrelationships among thrust pressure, feed, torque, and specific cutting energy using three different types of drill bits: common surgical twist bits, general purpose twist bits used for metals, and a specially constructed spade bit [9]. It was shown that the thrust pressure, torque, and specific cutting energy for all three drill bits could be described by a power function relationship. Results indicated that feed, *a*, could be represented as the following power function [9]:

$$a = BP^{x'}, \tag{2.15}$$

where *P* represents the thrust pressure, *B* was described as the feed that can be anticipated at a thrust pressure of 1 N/mm^2, and *x'* was defined as a measure of the sensitivity of penetrating ability to the thrust pressure [9]. Experimental results were obtained for all three drill bit types tested; these results are presented in Figure 2-9a. Using a similar approach, a relationship was developed for torque, *T*, and feed, *a*, as follows [9]:

$$\frac{T}{A} = C'a^{y'}, \tag{2.16}$$

where A is the cross-sectional area of the hole, and C' and y' were determined via least squares regression analysis. The experimental results and empirically formulas are displayed in Figure 2-9b. Finally, interrelationship between specific cutting energy, u, and feed, a, was established as [9]:

$$u = D'a^{-m'}, \tag{2.17}$$

where D' and m' where obtained via least squares regression. The results emerging from these experiments are presented in Figure 2-9c.

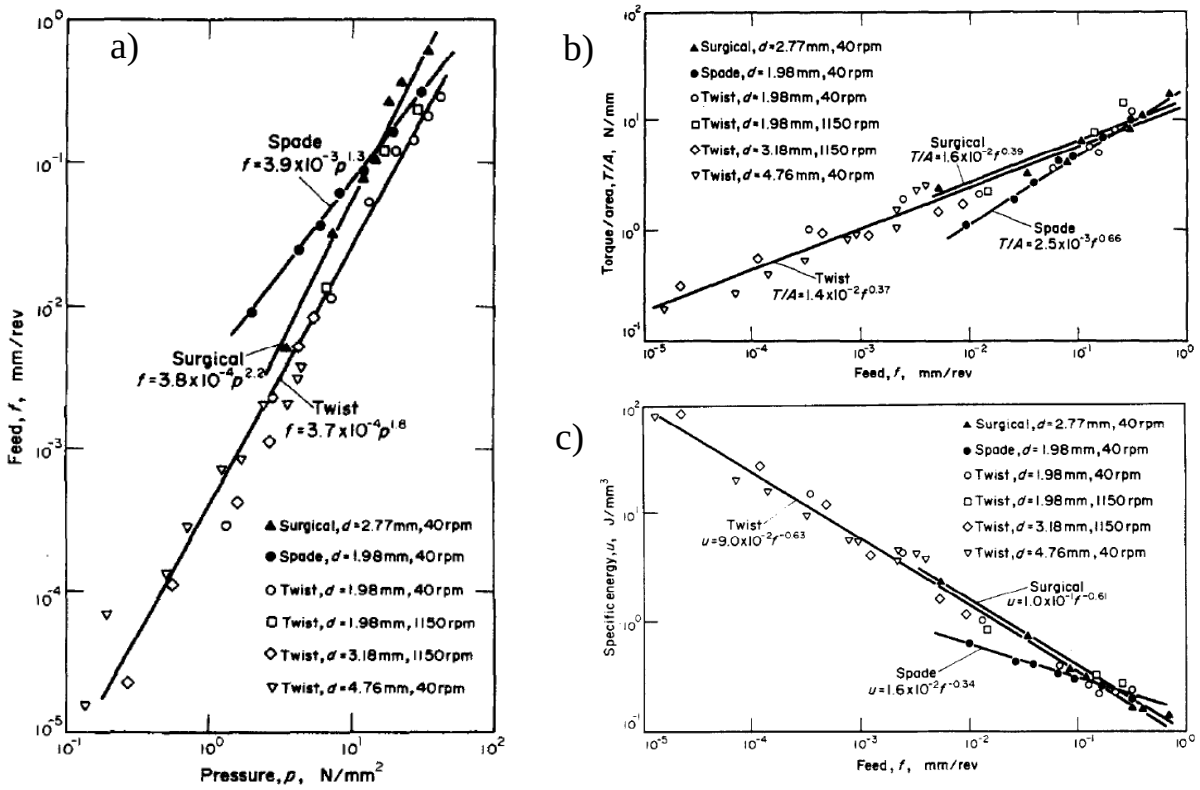

Figure 2-9: Experimental results relating feed with a) thrust pressure, b) torque, and c) specific cutting energy using three different types of drill bits [9].

It was the conclusion of the authors that drilling pressure, torque, and specific cutting energy were all dependent on the drill's feed and each of these relationships could be described by a power function unique to the type of drill bit used [9].

Another discovery of significance reported in this paper was the relationship between hole depth, drilling torque, and specific cutting energy. It was found that both drilling torque and specific cutting energy are greatly increased as the drill progresses through the bone. It was

conclude that this occurrence was a direct result of drill bit flute clogging and identified as a serious problem when drilling bone [9]. These results are depicted in Figure 2-10 for a 3.18 mm diameter general purpose twist drill bit rotating at 40 RPM and cutting at a constant pressure of 5.6 N/mm^2.

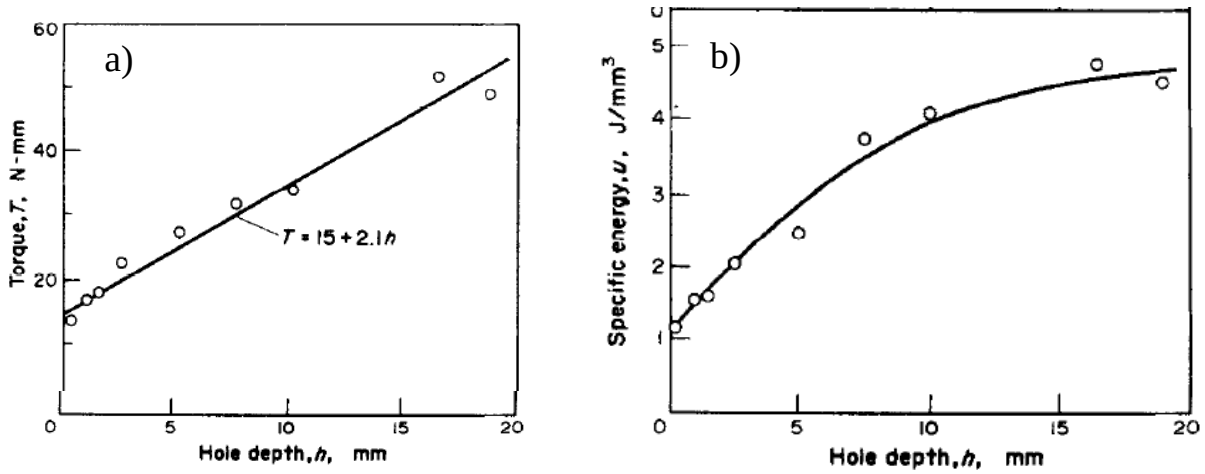

Figure 2-10: Experimental results relating hole depth with a) torque and b) specific cutting energy using a 3.18mm diameter drill bit [9].

Further research examined bone drilling from a slightly different perspective as exploration into drill bit tip geometry began to show importance when drilling bone. A study was conducted that examined 7 different drill tip geometries and analysed each on the basis of the thrust force and torque required for the cutting of bone [13]. Of the seven drill bits, five were commercially available surgical drill bits; one was a standard metal cutting bit, and the other an experimental point design. Additionally, a relationship was established which showed the dependence of drill thrust force and torque on spindle speed. Experiments were conducted using twelve different combinations of drill bit diameters and point angles. Experimental results were gathered from the drilling of bovine tibias using various feed rates and rotational speeds whilst measuring thrust force and torque [13]. A selection of the results obtained is displayed in Figure 2-11.

From these figures, both thrust force and torque significantly decrease as drill spindle speeds are increased. Later, these results were compared to the empirical formulation previously presented in [11]. The comparison showed adequate correlation. The following were concluded from these experiments [13]:

1) Bone drill bits must have significant point angle (no less than 25°).

2) Steep drill bit point angles are desired to prevent the drill from 'walking' on the surface of the bone.
3) The minimum spindle speed at which bone drilling should be performed is 750-1250 RPM. This prevents drill bit 'walking' and lowers thrust force and torque. Speeds much higher than this could produce excess heat.
4) Coolant should be used while drilling bone whenever possible. This will allow for greater spindle speeds to be achieved, thus lowering the thrust force and torque. A form of sterile saline solution was recommended.

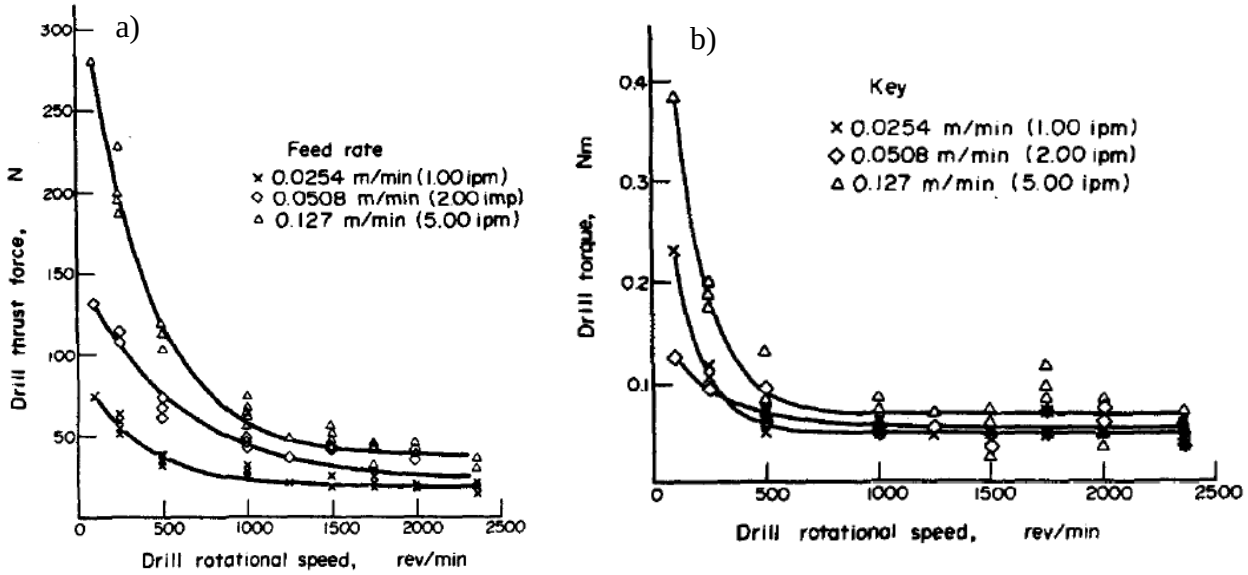

Figure 2-11: Experimental results relating the drill's rotational speed with a) thrust force and b) torque [13].

Another research group examined the drilling of bone using a very similar approach as Jacob et al. [13]. The main focus of this team's research was to examine the factors that facilitate increases in thrust pressure. Through experiments, the impact of six different drill types at varying spindle speeds was measured with each experiment being conducted by a different surgeon. The goal of these experiments was to determine, quantitatively, to what effect drill bit type, spindle speed, and interoperator variations would have on thrust pressure. It was shown that the type of drill bit does significantly affect the thrust pressure with the spear point drill bits and the Morse-type twist drill bits producing the lowest required thrust pressure [30]. Additionally, experimental results were presented that showed that spindle speed influenced thrust pressure as faster drill rotation resulted in lower thrust pressure. Finally, data was presented that showed that interoperator variations had the most significant effect on drilling thrust pressure. These results placed a clear emphasis on surgical standards and training methods [30].

The mechanical impedance experienced while drilling human bone was the next topic of interest for researchers. Experiments were conducted which, consequently, exhibited an interrelationship between feed rates, drilling strength, triaxial strength, and hardness of bone [31]. The term drilling strength was used to describe the ratio of energy input to the volume of material broken or removed and is commonly used when examining the process of cutting rock or stone. The reader should note the similarities between drilling strength and specific cutting energy which was previously introduced. Experimental results showed a linear relationship between spindle speed and feed rate at two different locations of the bone (mid-shaft and at the head of a femur bone) [31]. These results are displayed in Figure 2-12a. Another linear relationship was established experimental relating triaxial strength and drilling strength for the drilling of human cortical bone [31]. The results of these findings are depicted in Figure 2-12b.

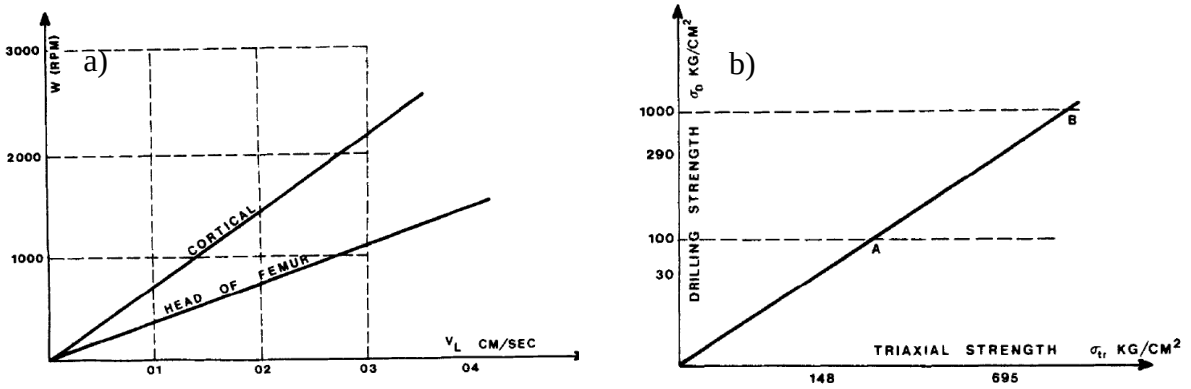

Figure 2-12: Experimental results relating a) spindle speed with feed rate at two different locations of the bone and b) drilling strength and triaxial strength [31].

In more recent years, research into the drilling of bone continued with investigations into the effects of spindle speed and energy consumption based on a constant applied thrust force [32]. Experiments were conducted by drilling bovine using a commercial surgical drill bit with a speedometer used to measure the rotational speed. It was found that the average operating spindle speed changed with varying forces. Specifically, it was shown that at slow starting speeds, the speed increased marginally with force, whereas, at high starting spindle speeds, speed significantly decreased with force [32]. Furthermore, it was determined that energy consumption is inversely proportional to spindle speed suggesting that, as the drill continues to penetrate the cortical bone at a constant applied thrust force, the spindle speed decreases while the energy consumption increases. An example of this relationship taken from this research is depicted in Figure 2-13.

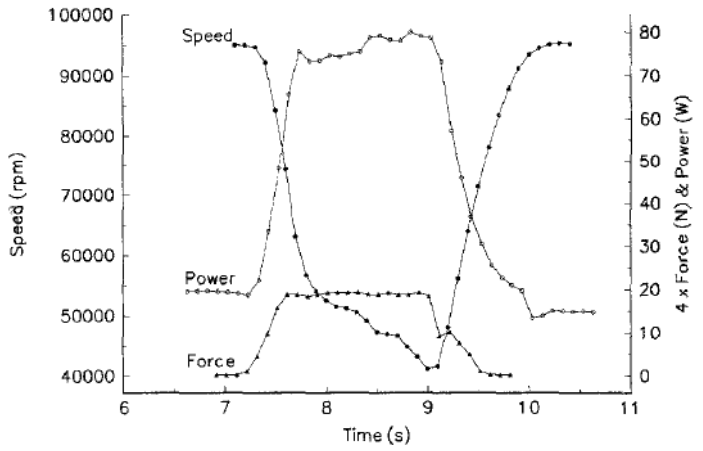

Figure 2-13: Experimental results indicating the three way relationship between spindle speed, thrust force, and power consumption [32].

Research into the drilling of bone next investigated the transition region between the cortical and cancellous bone. As was stated previously, the cortical and cancellous bones are very different in material properties and, thus, the cutting force and torque must be evaluated independently. This was accomplished by Allotta et al. when designing a mechatronic drilling tool for orthopaedic surgery [12]. This research group used a simplified version of Cook's formulation (Eq. 2.4) but incorporated superposition principals to account for the transition between materials. In addition to capturing the difference in material properties at the bone transition zone, a more accurate model of the cutting force and torque at the material entry and exit locations was created. This was accomplished by integrating with respect to depth to account for the change of drill tip contact at entry, exit, and material transition zones. Their theoretical model for cutting force was presented as follows [12]:

$$F(x_b) = a\sin\left(\frac{\beta}{2}\right)\tan\left(\frac{\beta}{2}\right)\left(u_1\int_0^{x_b} dx + u_2\int_{x_b}^{l} dx\right),$$

$$= a\sin\left(\frac{\beta}{2}\right)\tan\left(\frac{\beta}{2}\right)\left[u_1 x_b + u_2\left(l - x_b\right)\right], \qquad \textbf{(2.18)}$$

where u_1 and u_2 are the specific cutting energies of the cortical and cancellous bone, respectively, and x_b, l, and dx are the lengths shown in Figures 2-14a and 2-14b.

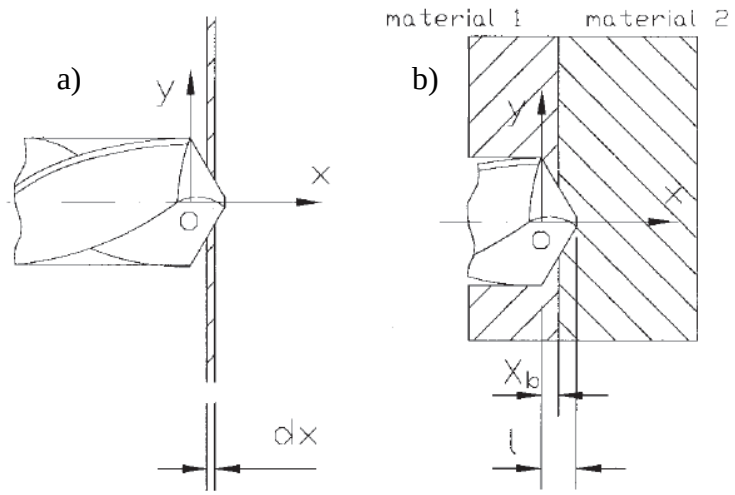

Figure 2-14: Pictorial representation of formulation parameters; a) infinitesimally small bone layer thickness, *dx*; b) material transition [12].

Similarly, the theoretical model for cutting torque was presented as follows [12]:

$$T\left(x_b\right) = a\tan^2\left(\frac{\beta}{2}\right)\left[u_1\int_0^{x_b}(l-x)dx + u_2\int_{x_b}^{l}(l-x)dx\right],$$

$$= a\tan^2\left(\frac{\beta}{2}\right)\left[u_1 x_b\left(l-\frac{x_b}{2}\right)+\frac{u_2}{2}\left(l-x_b\right)^2\right]. \quad \textbf{(2.19)}$$

These models were experimentally validated with the results displaying good correlation. An example of the validation experiments taken at the exit of the cortical bone was presented and appears here as Figure 2-15. Figure 2-15 displays a linear decrease shown as the * line (theoretical data) which closely predicts the continuous lines representing the experimental data.

2.6 Force and Torque Prediction Modelling for Haptic Rendering

Early research into orthopaedic surgery haptic simulation systems focused mainly on graphic rendering with little emphasis placed on haptic rendering. By doing so, many of the original platforms utilized force and torque prediction models previously developed. One such example is the system designed by Peng et al. [14]. This early haptic simulation took advantage of simplified versions of Allotta's formulations (Eqs. 2.18 and 2.19). These formulations were simplified by ignoring the drill tip entry and exit while also excluding the transition zones between the cortical and cancellous bone. This left force and torque prediction equations that

result in constant cutting force and torque from drill entry to exit. These simplified expressions for predicting force and torque were presented as follows [14]:

$$F = u\,a\frac{D}{2}\sin\frac{\beta}{2}, \tag{2.20}$$

$$T = 5R_a a\frac{D^2}{2}, \tag{2.21}$$

where R_a is the unitary ultimate tensile load.

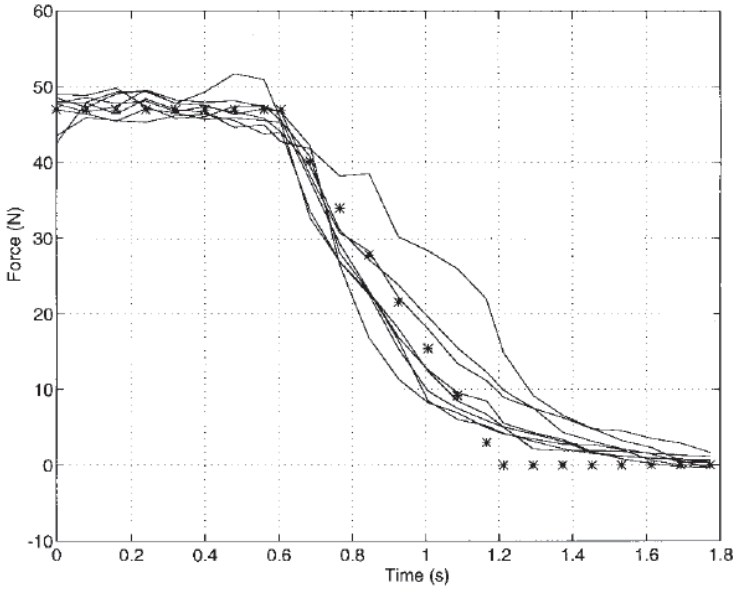

Figure 2-15: Experimental results used to validate the proposed model at the exit of the cortical bone [12].

Subsequent studies explored the possibility of developing unique empirical models for predicting cutting force and torque during the drilling of bone. It was shown that the drilling thrust force could be modeled using regression techniques and written as a function of drill speed, feed rate, and material density [15]. The empirical force model was presented in the following form [15]:

$$F = C_T N^{C_N} f^{C_f} \rho^{C_D}. \tag{2.22}$$

Here, f is the feed rate in mm/sec, ρ is the material density in g/cc, and C_T, C_N, C_f, and C_D are the constants of the model. Next, the logarithm of the equation was taken yielding the following [15]:

$$\log(F) = \log(C_T) + C_N \log(N) + C_f \log(f) + C_D \log(\rho). \quad \textbf{(2.23)}$$

To solve for the constants of the model, an undeclared amount of calibration experiments were conducted using three different feed rates and three different spindle speeds. Using the collected experimental data, a QR decomposition algorithm was implemented yielding the model constants. These constants were reported as [15]:

$$C_T = 134.6097 \quad C_N = -0.3327 \quad C_f = 0.5189 \quad C_D = 1.1841.$$

These values were inserted into the original formulation for thrust force (Eq. 2.22) to produce the following [15]:

$$F = 134.6 N^{-0.3327} f^{0.5189} \rho^{1.1841}. \quad \textbf{(2.24)}$$

It was reported that the above empirical formula predicted the thrust force within 10% difference of the measured value [15]. Additionally, an example of the experimental validation was provided and is displayed in Figure 2-16. It should be noted that the haptic interface used for the above formulation was a single degree-of-freedom system and thus was incapable of producing a torque feedback.

The most recent haptic simulation system utilized machining theorem to calculate the load on the cutting lips and chisel edge [16]. These loads were then summated to produce the overall drilling force and torque. Additionally, the models were created to account for all six degrees-of-freedom including forces and torques about the x- and y-axis. The model was developed using small surface elements along the drill bit and the virtual voxel location of the tool tip. Figure 2-17 displays how each of the forces and torques were defined. The loads acting at the various locations on the drill bit as shown in Figure 2-17 were defined as [16]:

$$F_{i,j}^{H} = \Delta K_H \cdot \mathrm{d}w \cdot \frac{f}{n}, \quad \textbf{(2.25)}$$

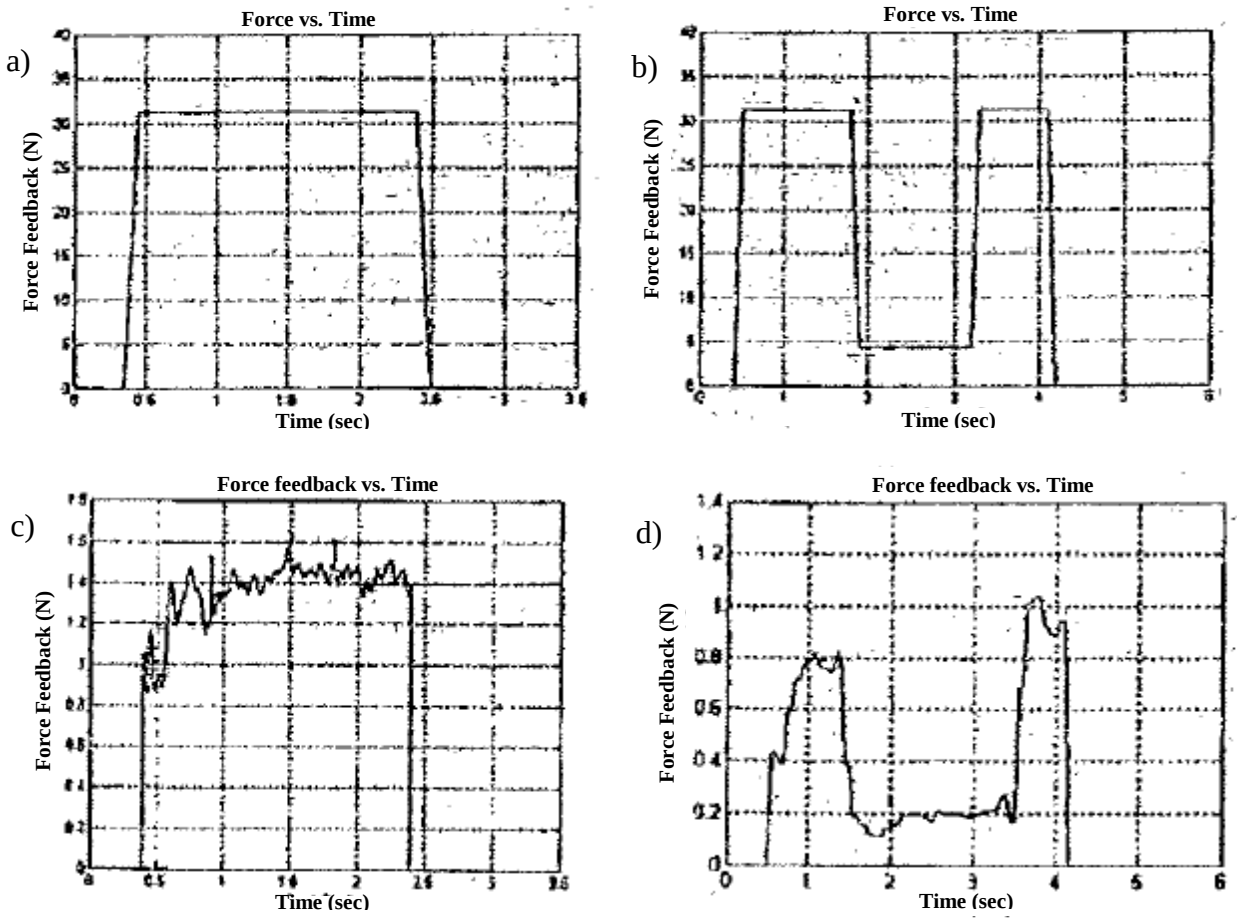

Figure 2-16: The simulated results based on the purposed model for drilling a) unicortical and b) bicortical. The experimental results obtained drilling c) unicortical, and d) bicortical [15].

$$F_{i,j}^{T} = \Delta K_T \cdot \mathrm{d}w \cdot \frac{f}{n}, \tag{2.26}$$

$$F_{i,j}^{V} = \Delta K_V \cdot \mathrm{d}w \cdot \frac{f}{n}, \tag{2.27}$$

where dw was defined as the surface thickness, n is the number of cutting lips, and Δ is 1 if the element is inside the voxel and 0 if otherwise.

Each of the load components was then summated to produce the tangential, thrust, and radial components. This summation was shown to take the following form [16]:

$$F_{tang} = \sum_{i,j} \left(F_{i,j}^{H} \right), \tag{2.28}$$

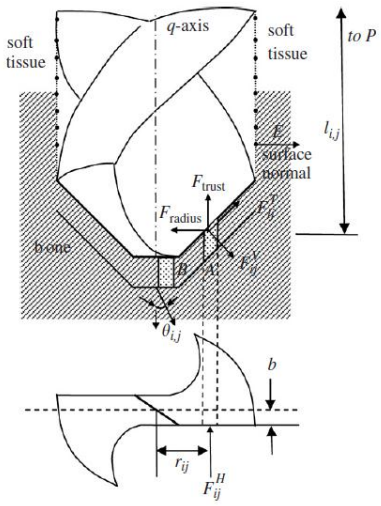

Figure 2-17: Free body diagram of the forces acting on the tip of a drill bit [16].

$$F_{trust} = \sum_{i,j} \left(\cos\left(\theta_{i,j}\right) \cdot F_{i,j}^{T} + \frac{\sqrt{\left(r_{i,j}^2 - \left(\frac{d'}{2}\right)^2 \right)}}{r_{i,j}} \sin\left(\theta_{i,j}\right) \cdot F_{i,j}^{V} \right), \tag{2.29}$$

$$F_{radius} = \sum_{i,j} \left(\frac{\sqrt{\left(r_{i,j}^2 - \left(\frac{d'}{2}\right)^2 \right)}}{r_{i,j}} \sin\left(\theta_{i,j}\right) \cdot F_{i,j}^{T} - \cos\left(\theta_{i,j}\right) \cdot F_{i,j}^{V} \right), \tag{2.30}$$

where $r_{i,j}$ is the distance of the element from the q-axis and $\theta_{i,j}$ is the half the point angle. Similarly, the elements were summated to produce the three torque values presented as [16]:

$$T_{\text{tang}} = \sum_{i,j} \left(r_{i,j} \cdot F_{i,j}^{H} \right), \tag{2.31}$$

$$T_{radius} = \sum_{i,j} \left(l_{i,j} \left(\frac{\sqrt{\left(r_{i,j}^2 - \left(\frac{d'}{2}\right)^2 \right)}}{r_{i,j}} \sin\left(\theta_{i,j}\right) \cdot F_{i,j}^{T} - \cos\left(\theta_{i,j}\right) \cdot F_{i,j}^{V} \right) \right), \tag{2.32}$$

$$T_{\text{thrust}} = \sum_{i,j} \left(r_{i,j} \left(\cos\left(\theta_{i,j}\right) \cdot F_{i,j}^{T} + \frac{\sqrt{\left(r_{i,j}^{2} - \left(\frac{d'}{2} \right)^{2} \right)}}{r_{i,j}} \sin\left(\theta_{i,j}\right) \cdot F_{i,j}^{V} \right) \right). \quad \textbf{(2.33)}$$

Here, $l_{i,j}$ denotes the distance from each element to the rotational centre for bending. It should be noted that the haptic hardware that was utilized for this system was unable to produce torque feedback resulting in only the force algorithm being used.

3 Drilling of Bone: Force and Torque Modelling

As was briefly discussed in Chapter 2, forces and torques not associated with the cutting of material are a result of friction and chip-buildup in the drill's flutes. In other words, the evacuated material is clogging the drill bit's flutes and results in an increase of force and torque experienced by the drill's operator [33]. For shallow drilling of ductile materials, these forces are either non-existent or negligible as the chips are formed continuously and evacuate the flute without hindrance. This is evident from Figure 3-1 for the drilling of 6061 T-6 aluminium alloy [34]. The force and torque increase approximately linearly as the tip of the drill bit is engaging the material. Once the drill tip is fully engaged into the material, both the force and torque flatten out and become constant for the remainder of the drilling operation. These results are typical when drilling most ductile materials.

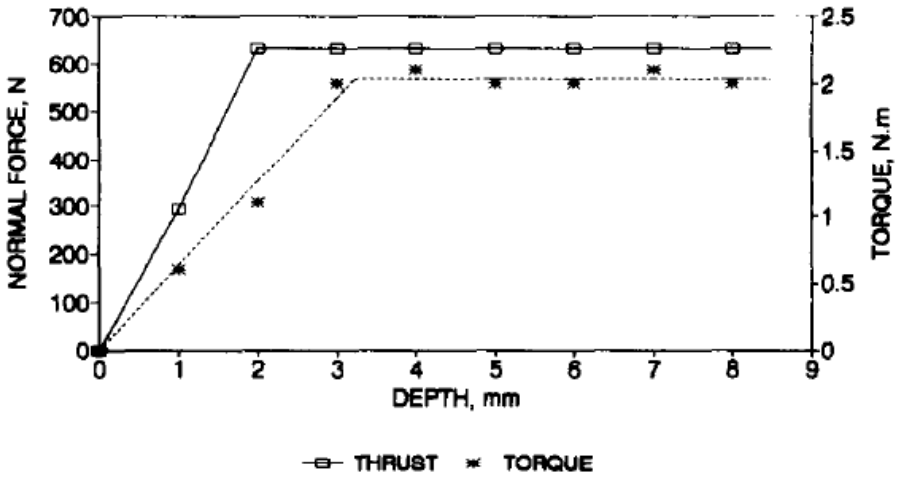

Figure 3-1: Drilling thrust force and torque verses depth for the drilling of 6061 T-6 Aluminium alloy at a feed of 0.16 mm/rev and 112 RPM [34].

The drilling of brittle materials, such as bone, produces discontinuous chips that do result in a significant increase in thrust force and torque as a consequence of flute clogging [9]. As an example, Figure 3-2 displays the thrust force and torque versus depth seen during drilling of a bovine bone. From this figure it can be seen that the cutting force, F_0, and the cutting torque, T_0, are achieved after a rapid increase as the drill tip fully engages the material. Much like the example provided for the drilling of metals, this increase is approximately linear. Once the drill tip is fully engaged, the cutting force and torque remain constant over the remainder of the

drilling of the hole. The additional forces observed in Figure 3-2 can be solely attributed to the forces required to move the growing amount of chips along the drill's flute. This additional force and torque will be referred to henceforth as chip-evacuation force and the chip-evacuation torque, respectively.

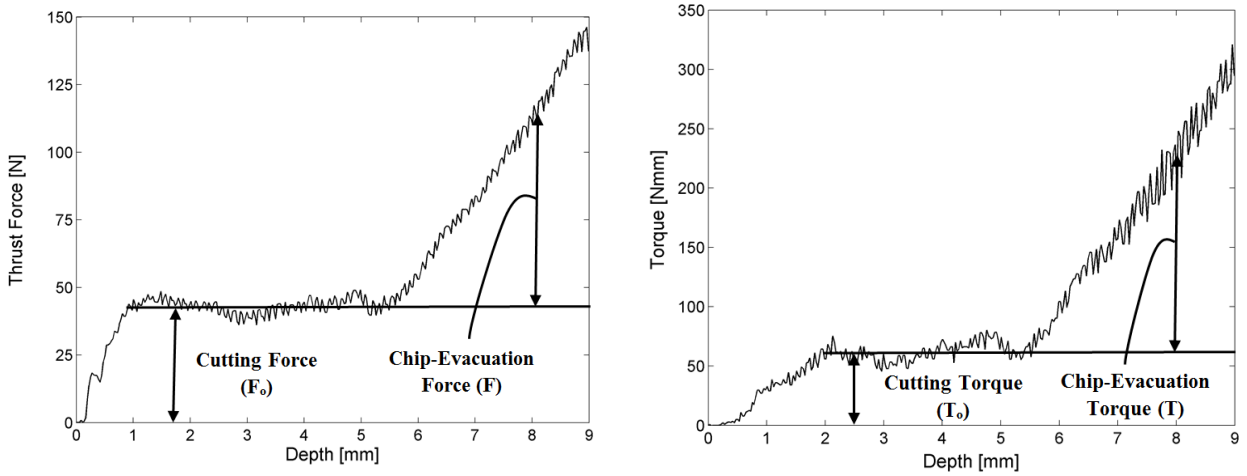

Figure 3-2: Example of experimental data collected from the drilling of bovine bone.

This chapter will examine the two independent cutting phases just introduced: cutting force/torque and chip-evacuation force/torque.

3.1 Cutting Force and Torque Modeling

The cutting force and torque experienced while drilling bone is not that unlike the drilling of most other materials. As was discussed in Chapter 2, the prediction of these forces are generally formulated based on some combination of operating variables such as drill bit geometry, feed rate, spindle speed, and/or specific cutting energy. This section will only briefly examine cutting force and torque as it is a necessary lead-in to the clogging phase.

Of the cutting force and torque prediction models presented in Chapter 2, the most comprehensive are those of Allotta [12]. These models not only account for the entry of the drill bit tip but also describe the transition region as the drill passes through cortical bone into cancellous bone and vice versa. Additionally, these formulations displayed good correlation with experimental results. It is for these reasons that Allotta's models were selected to describe the cutting force/torque phase of the drilling process. These force and torque prediction models are repeated here for convenience [12]:

$$F(x_b) = a\sin\left(\frac{\beta}{2}\right)\tan\left(\frac{\beta}{2}\right)\left[u_1 x_b + u_2\left(l - x_b\right)\right],$$

$$T(x_b) = a\tan^2\left(\frac{\beta}{2}\right)\left[u_1 x_b\left(l - \frac{x_b}{2}\right) + \frac{u_2}{2}\left(l - x_b\right)^2\right],$$

where each parameter is as described in Chapter 2. To provide an illustration of the effectiveness of these models, Figure 3-3 displays a comparison plot of the force formulation versus the experimental data collect while drilling bovine bone.

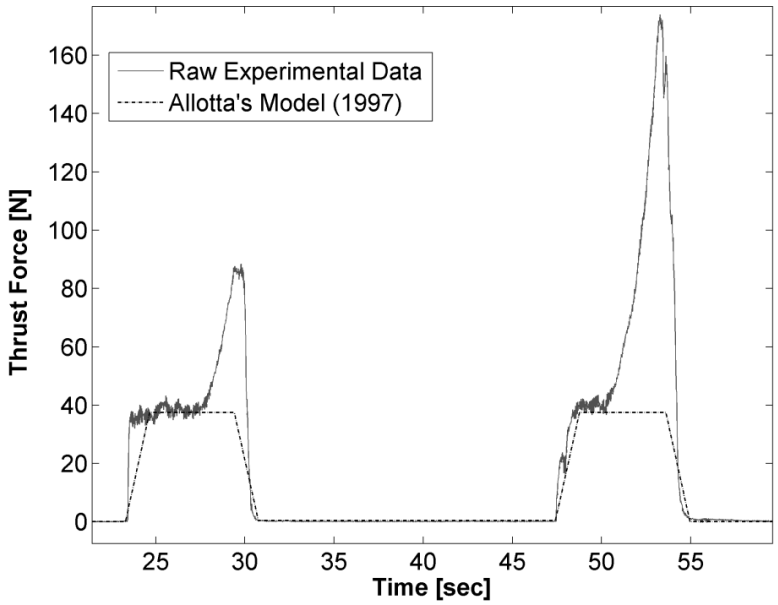

Figure 3-3: Plot comparing Allotta's force prediction model with raw experimental data collected drilling bovine bone.

The experiment was performed using a feed, *a*, of 0.09 mm/rev. Additionally, the drill bit used was a standard stainless steel orthopaedic drill bit with a point angle, β, of 90° and a diameter of 2.7mm. Based on the geometry, the length of the drill tip cone, *l*, was calculated to be 1.35mm. See Appendix A for calculation. The values for specific cutting energy for cortical bone, u_1, and cancellous bone, u_2, were obtained from the literature [24].

From Figure 3-3, it is clear that Allotta's force model correctly predicts the magnitude of the cutting force when drilling bi-cortical (through both cortex) through a bovine femur. The model's apparent deficiency is the ignorance of the chip-evacuation force due to drill flute

clogging. To further emphasise this point, Figure 3-4 displays a clearer perspective of the same comparison this time displaying a comparisons of both force and torque experienced drilling unicortical (though a single cortex). The reader should note the parabolic increase and decrease evident in Figure 3-4b as reflected in Allotta's torque prediction model.

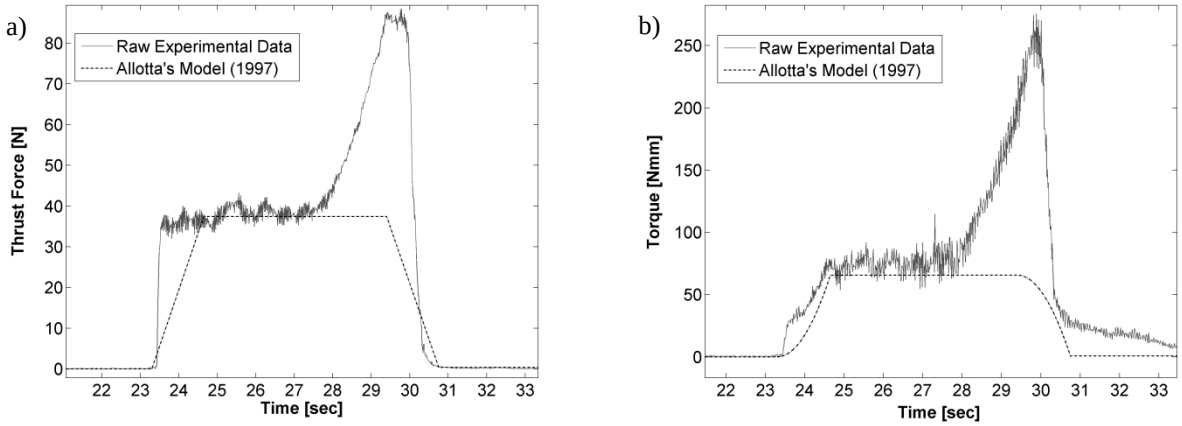

Figure 3-4: Plots comparing Allotta's a) force and b) torque prediction models with raw experimental data collected drilling bovine bone.

3.2 Chip-evacuation Force and Torque Modeling

The force observed as exponentially increasing beyond the cutting force, as seen in Figure 3-4, can solely be attributed to the clogging of material attempting to vacate the drill's flute at the hole's surface [9]. When the drilling process is being conducted at high spindles speeds and slow feed rates, the bone material has the opportunity to clear the drill's flutes without much hindrance. The discontinuous chips produced from the process just described are shown in Figure 3-5a and appear as a white flaky/powdery substance. This is contrasted by the continuous chips presented in Figure 3-5b for the typical drilling of metal.

The problem of flute clogging arises when spindles speeds are at lower RPMs and feed rates are increased. This is typical for the drilling of bone since it has been shown that high spindle speeds and/or slow feed rates can cause a high increase in temperature at the bone/tool interface resulting in damage to the bone [35]. For this reason, surgical drills generally use low spindle speeds and surgeons tend to conduct the drilling at relatively fast rates. Typical spindle speeds and feed rates used by orthopaedic surgeons for the drilling of bone will be further discussed in Chapter 4.

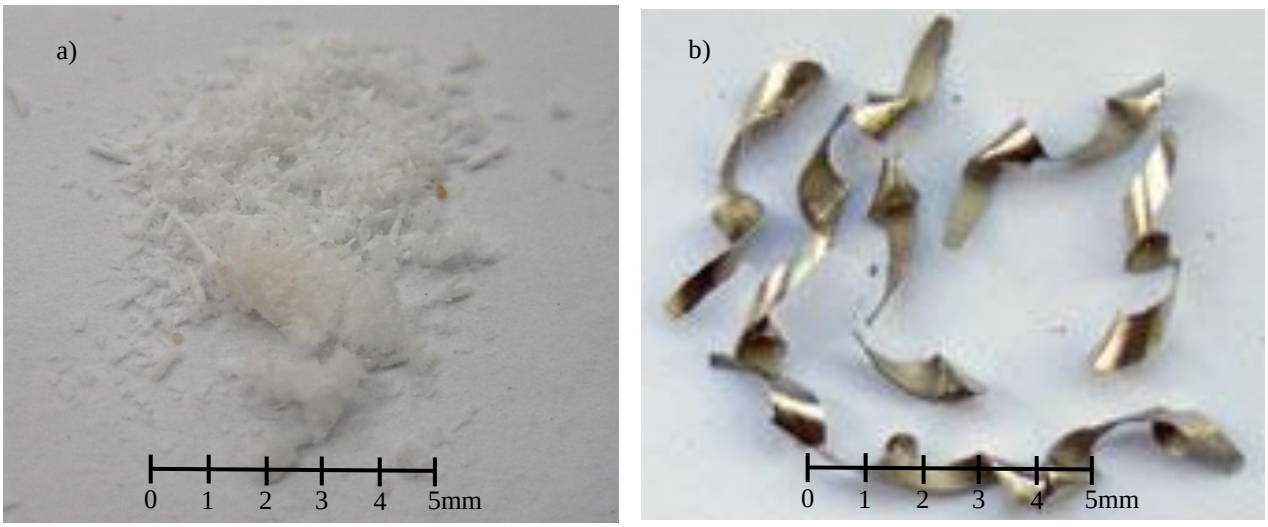

Figure 3-5: Chip formation resulting in the drilling of a) bovine bone and b) AISI 316 stainless steel.

The consequence of drilling bone at slower spindle speeds and more rapid feed rates is that the removed material begins to clog in the drill's flute prior to being entirely evacuated. The more and more the chips begin to build-up, the greater the increase in frictional resistance. Additionally, this also initiates a sizable increase in the pressure and temperature exerted on the removed material which causes the chips to compact and become more of a solid as opposed to the flaky/powdery material observed in Figure 3-5a. To illustrate this, Figure 3-6 presents a comparison of bovine bone material after drilling. Figure 3-6a shows clogged bone removed from a drill bit's flute using a relatively low spindle speed and fast feed rate (750 RPM and 3.0mm/sec, respectively) as compared to Figure 3-6b, which displays the same material which evacuated the drill without clogging due to a relatively high spindle speed and slow feed rate (2500 RPM and 0.5mm/sec, respectively).

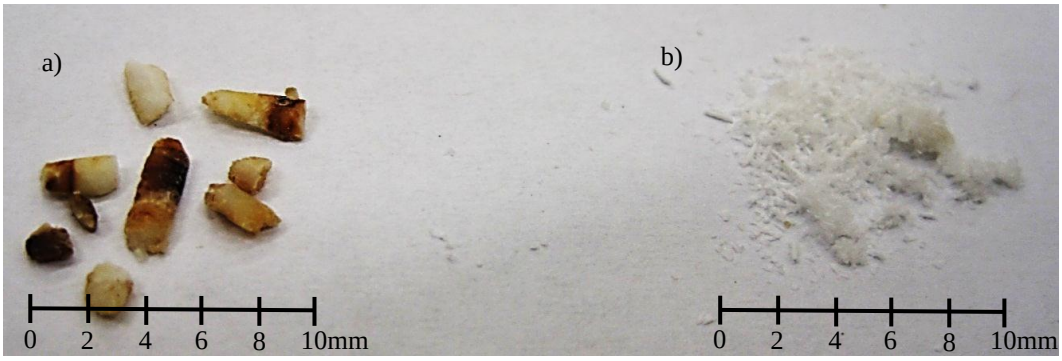

Figure 3-6: The two forms of material removed by drilling bovine bone: a) clogged material and b) evacuated material.

An obvious change of state, from powder to solid, and color, from white to brown, can be observed in Figure 3-6 as a result of the increased pressure and temperature caused by material clogging. The operating parameters that were used to obtain this figure are slightly outside that of the typical range. This exaggeration was only intended to provide an explicit illustration of the significance of material clogging.

3.2.1 Empirical Model

The discontinuous chips resulting for the drilling of bone are classified as granular solids. This means that they share characteristics of both liquids and solids [28]. Specifically, as liquids, granular solids occupy the shape of the container in which they fill, exert pressure on the extreme boundaries of that container, and readily flow through available openings. As solids, granular solids have compressive strength, possess non-isotropic stress distribution, and when loaded, the shear stress is proportional to the normal stress [36].

Since machined bone is considered to be a granular solid, a model was developed to predict the force and torque required to 'move' the material along the drill bit's flute. This allows for the use of previously developed techniques utilized for investigations involving the flow of granular solids through the solid conveying zone of a screw extruder used in the processing of polymers [36]. The force required to move the chip formation along the drill's flute can be explained by investigating the pressure distribution and accompanying force balance on a differential chip section of material in the drill's flute. Figure 3-7 displays this differential chip section, *dz'*, as the hatched area along one of the drill's flutes. In Figure 3-7, *z'* represents the distance for the material surface to the current location of the drill tip.

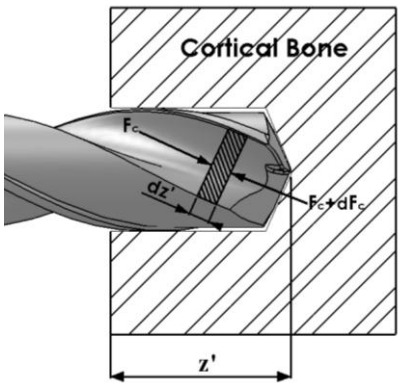

Figure 3-7: A drill penetrating cortical bone with the hatched area indicating a differential chip section, *dz'*.

To get a better understanding of the force balance, a cross-section of a standard twist drill bit is provided in Figure 3-8. Again, the hatched area represents the material inside one of the drill's flutes. The direction of rotation is indicated by ω. There are four areas of contact in this figure: contact between the bone chip and the drill bit at the flute face, heel, and root, and the contact between bone chip and the wall of the hole. These four bone chip interaction locations are of interest for the purpose of force balance.

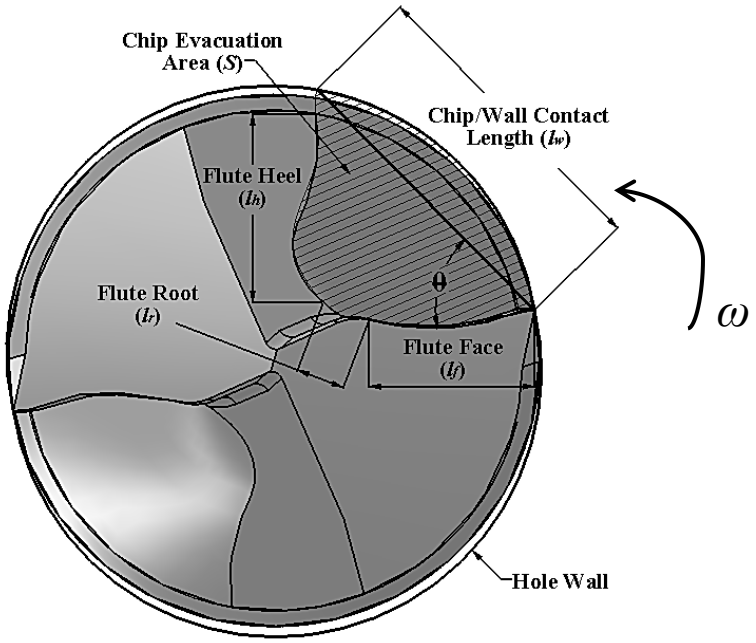

Figure 3-8: A cross-section of a typical twist drill bit.

A close up view of the differential bone chip section and the relative force balance is provided is Figure 3-9. The chip-evacuation force per flute, F_c, can be determined by applying a force balance in axial direction on the forces displayed in Figure 3-9 [29]:

$$F_c - (F_c + dF_c) + F_{ff} + F_{hf} + F_{rf} + F_{fwi} = 0, \quad (\mathbf{3.1})$$

where F_{ff}, F_{hf}, and F_{rf} are the axial frictional forces caused by the flute face, heel, and root, respectively. The frictional force F_{fwi} is a result of the friction between the bone chips and the wall of the hole. Although the frictional force from the wall, F_{wf}, does appear in Figure 3-9, it is not used in Eq. 3.1 because it does not act in the axial direction. This frictional force is considered to be acting in the tangential direction since the tangential velocity (resulting from the

rotational speed of the drill's spindle) is significantly greater than the axial velocity (resulting from the feed rate of the drill).

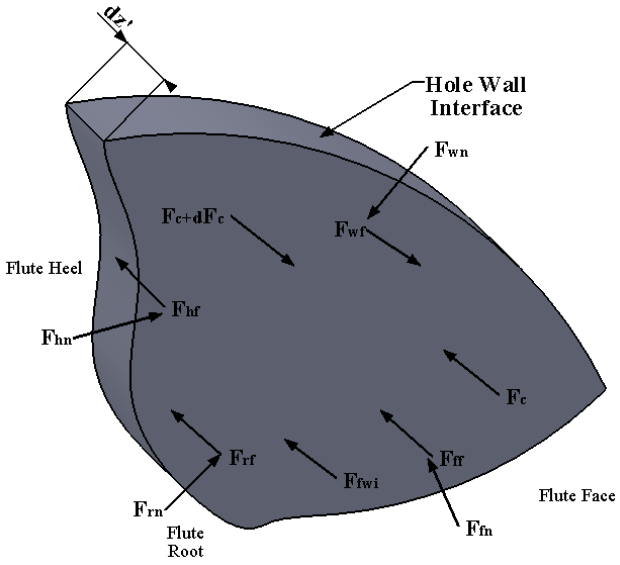

Figure 3-9: Force balance on differential bone chip section.

The chip-evacuation force, F_c, causes an axial pressure, P, on the differential chip section. This means that the chip-evacuation force is a product of this axial pressure and the flute cross-sectional area, S, i.e.:

$$F_c = SP\,. \tag{3.2}$$

The axial pressure induced in the differential chip section causes the chip to expand in the plane of the flute cross-section. A lateral pressure is developed along the plane of the drill's cross-section as a result of the chips being contained on all sides. This lateral pressure can be considered to be proportional to the axial pressure through a constant η allowing for the lateral pressure to be defined as ηP [37]. Although this pressure may vary marginally, it can be assumed to remain constant [37]. The normal forces appearing in Figure 3-9 can be determined as the product of the lateral pressure and the affected area:

$$F_{fn} = \eta P l_f D dz\,, \tag{3.3}$$

$$F_{hn} = \eta P l_h D dz\,, \tag{3.4}$$

$$F_{rn} = \eta P l_r D dz\,, \tag{3.5}$$

$$F_{wn} = \eta P l_w D dz\,, \tag{3.6}$$

where F_{fn}, F_{hn}, and F_{rn} are the normal forces at the flute face, heel, and root, respectively, and F_{wn} is the normal force at the wall of the hole. The dimensions l_f, l_h, l_r, and l_w are the geometric lengths as defined in Figure 3-8. Finally, z represents the dimensionless depth to diameter ratio, $z=z'/D$.

The frictional forces at the contact surfaces of the drill's flute and the wall of the hole will be acting in the opposite direction of the relative velocity. Additionally, based on the definition of Coulomb kinetic friction, these forces are related to their respective normal forces by a coefficient of friction. Thus, the frictional forces can be written as:

$$F_{ff} = \mu_f F_{fn} = \mu_f \eta P l_f D dz\,, \tag{3.7}$$

$$F_{hf} = \mu_f F_{hn} = \mu_f \eta P l_h D dz\,, \tag{3.8}$$

$$F_{rf} = \mu_f F_{rn} = \mu_f \eta P l_r D dz\,, \tag{3.9}$$

$$F_{wf} = \mu_w F_{wn} = \mu_w \eta P l_w D dz\,, \tag{3.10}$$

where μ_f is the coefficient of friction between the bone chip material and the drill's flute and μ_w is the coefficient of friction between the bone chip material and the wall of the hole. The frictional force from the wall of the hole causes the chips to build-up and thrust against the flute face. This results in an increase in the normal force seen at the flute face. It should be noted that this also increases the normal forces seen at the flute's root and heel but the increase is minimal and can, thus, be assumed negligible [29]. This increase in normal force seen at the flute face creates the frictional force F_{fwi} which is written as:

$$F_{fwi} = \mu_f F_{wf} \sin\theta\,, \tag{3.11}$$

where θ is the angle formed between the flute face and the plane formed across the flute (see Figure 3-8).

Substituting Eqs. 3.7-3.11 into Eq. 3.1 yields the force balance equilibrium in the following form:

$$SP - S\left(P + dP\right) + \mu_f \eta P l_f D dz + \mu_f \eta P l_h D dz + \mu_f \eta P l_r D dz + \mu_f \mu_w \eta P l_w D \sin\theta dz = 0, \quad \textbf{(3.12)}$$

which can be rearranged and simplified to yield:

$$\frac{dP}{P} = \frac{\eta D \mathrm{M}}{S} dz, \quad \textbf{(3.13)}$$

where M is defined as:

$$\mathrm{M} = \left(l_f \mu_f + l_h \mu_f + l_r \mu_f + l_w \mu_f \mu_w \sin\theta\right). \quad \textbf{(3.14)}$$

Integrating Eq. 3.13 produces the chip-evacuation pressure:

$$P\left(z\right) = P_o e^{\left(\frac{\eta \mathrm{M} D}{S}\right) z}, \quad \textbf{(3.15)}$$

where P_o is the initial axial cutting pressure at z=0. Assuming the cross-sectional area of the drill's flute remains constant over the entire length of the drill bit, the chip-evacuation force can be obtained by dividing Eq. 3.15 by the area, S. This yields the following as the chip-evacuation force model:

$$F_c\left(z\right) = F_o e^{\left(\frac{\eta \mathrm{M} D}{S}\right) z}, \quad \textbf{(3.16)}$$

where F_o is the initial cutting force at z=0.

The chip-evacuation torque can be modeled in a similar fashion. The chip-evacuation torque is simply the product of the frictional force on the wall of the hole and the radius of the drill bit. This can be written as:

$$dT_c = RF_{wf}, \quad \textbf{(3.17)}$$

where R is the radius of the drill bit. Substituting Eq. 3.10 for the frictional force, F_{wf}, and Eq. 3.15 for pressure, P, yields the following integral:

$$T_c = \int_0^z R\mu_w \eta l_w D \frac{F_o}{S} e^{\left(\frac{\eta \mathrm{M} D}{S}\right)\zeta} d\zeta \,, \tag{3.18}$$

which after integrating becomes:

$$T_c(z) = \frac{R\mu_w l_w F_o}{\mathrm{M}} \left(e^{\left(\frac{\eta \mathrm{M} D}{S}\right) z} - 1 \right). \tag{3.19}$$

Equations 3.16 and 3.19 provide closed-form expressions that can be used to predict the chip-evacuation force and torque as a function of the independent variable, *z*. These expressions also contain the two coefficients of friction: μ_f, the coefficient of friction between the bone chip and the drill flute, and μ_w, the coefficient of friction between the bone chip and the hole of the wall. To establish a value for these constants, a set of calibration experiments is required. The experimentation methodology and calibration procedure will be presented in Chapter 4.

The above formulations were established based on several assumptions. To properly substantiate the presented models, this section will conclude with a list of these assumptions: (1) the bone chips remain in constant contact with one another; (2) the evacuated material flows through and fills the drill's flute; (3) the bone chips are continuously exerting pressure on the contacting surfaces (i.e. the drill flute and the wall of the hole); (4) the helix angle of the drill bit is negligible; (5) the frictional forces between the bone chips and their contacting surfaces are proportional to their normal forces; and (6) nonisotropic stress distribution is exhibited by the bone chips.

3.2.2 Artificial Neural Network

An alternative to empirical modeling is the development of an artificial neural network (ANN). As its title would suggest, an ANN mimics the way a biological nervous system functions by processing information using interconnected processing elements (neurons) to solve a problem. Applications of ANN include pattern recognition, regression analysis, sales forecasting, process control, data processing, and risk management.

A simple neural network is composed of two layers: a hidden layer of neurons and an output layer of neurons. Each of these two layers function similarly: each layer receives an input, multiplies that input by a unique weight, adds a bias to the product, and passes the result through

a transfer function. An example of the hidden layer of a simple single input, single output, and single neuron neural network is displayed in Figure 3-10 where *h* is the scalar input, *w* is the scalar weight, *b* is the scalar bias, *s* is the net input, and *g* is the scalar output. The box with the *f* represents the transfer function which is chosen based on by the application of the ANN. The weights and bias of the neural network are determined through a training procedure.

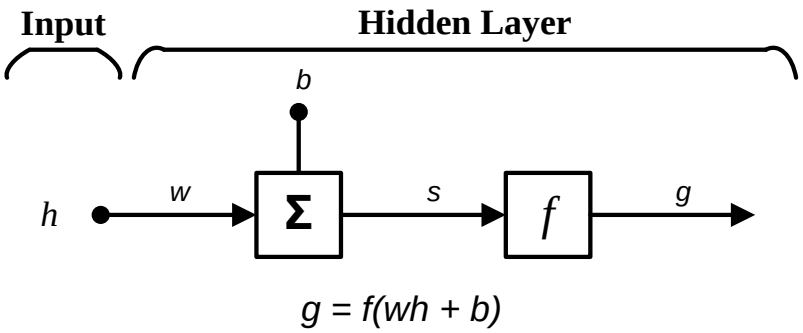

Figure 3-10: A single neuron artificial neural network.

The ANN develops the solution to problems via the presentation of large sets of data which it utilizes for training, validation, and testing without the need for a priori knowledge. In fact, the only substantial requirement for obtaining accurate results from a neural network is a large enough collection of meaningful data such that the network can be properly trained. Just to clarify, the following is how Matlab distinguishes between the terms training, validation, and testing:

Training: … presented to the network during training, and the network is adjusted according to its error.

Validation: … used to measure network generalization, and to halt training when generalization stops improving.

Testing: … have no effect on training and so provide an independent measure of network performance during and after training.

To train an ANN, the data sets must be divided into two distinct collections: input data and target data. The input data is self-explanatory whereas the target data is simply the desired network output that will be used for training. Each sample of data (input and target) is allocated

to be used as either training, validation, or testing data. Usually the quantity of samples to be used for each training, validation and testing is determined based on a percentage of the total number of samples. Once training is complete, the user can input known values and obtain the desired output values generated by the ANN.

3.2.2.1 Network Development

The neural network for the application of force/torque prediction modeling was created using the neural network toolbox in Matlab. Specifically, the 'Neural Network Fitting Tool' graphic user interface (GUI) was utilized. The default network settings use a sigmoid transfer function for the hidden layer neurons and a linear transfer function for the output layer neurons. The use of a sigmoid transfer function is desirable in this situation since it utilizes an exponential operator in a similar manner as the one found in the proposed empirical models. Also as the default, the network is trained using the Levenberg-Marquardt backpropagation algorithm. Additionally, this interface allows the user to define the number of hidden layer neurons, the data to use for training, and the amount of data to allocate for training, validation and testing. Finally, the GUI evaluates the network's performance using mean square error and regression analysis each for training, validation, and testing, independently.

Since a large array of data is required for training, validation, and testing, the ANN will require experimental data to complete its development. The procedure for acquiring this data will be presented in Chapter 4 and the ANN will be completed with accompanying results in Chapter 5.

3.3 Finite Element Modeling

In this section, the finite element simulation used for this work will be introduced. A solid model of a human bone was loaded dynamically with the forces and torques approximated from the empirical modeling and the resulting deflection and stress was obtained. These results can be compared to the results acquired using traditional force and torque prediction models presented in the literature. Additionally, the load positioning can be altered to allow a comparison of the results from one location to another.

3.3.1 Human Femur Bone Model Acquisition

A comprehensive, detailed solid model of a human femur bone was obtained from Pacific Research Labs (Vashon, WA, USA). This particular model was of a medium sized adult left femur. The choice of a femur bone was made due to the fact that the femur is the longest, strongest, and heaviest bone in the human body and will, thus, provide for the worst case scenario when measuring deflection, stresses, and strains due to mid-diaphysis drilling. Also, the femur bone is a popular site of injury in orthopaedic trauma that requires drilling techniques to permit the insertion of bone screws to aid in the alignment of bone fragments [39-46].

The software that was selected for this analysis was ANSYS Workbench 11.0 (ANSYS Inc., Canonsburg, PA, USA). The model was imported into ANSYS as three solid bodies: the cortical bone, the cancellous bone proximal, and the cancellous bone distal. The intramedullary canal was modeled as an empty space in accordance with the geometric specifications outlined by Pacific Research Labs. The geometry of these imported solids is displayed in Figure 3-11. The material properties of each of the three solid bodies were adjusted to reflect the respective material properties of cortical and cancellous bone obtained from the literature as was presented in Chapter 2. The specific values used in the simulation can be found in Table 3-1.

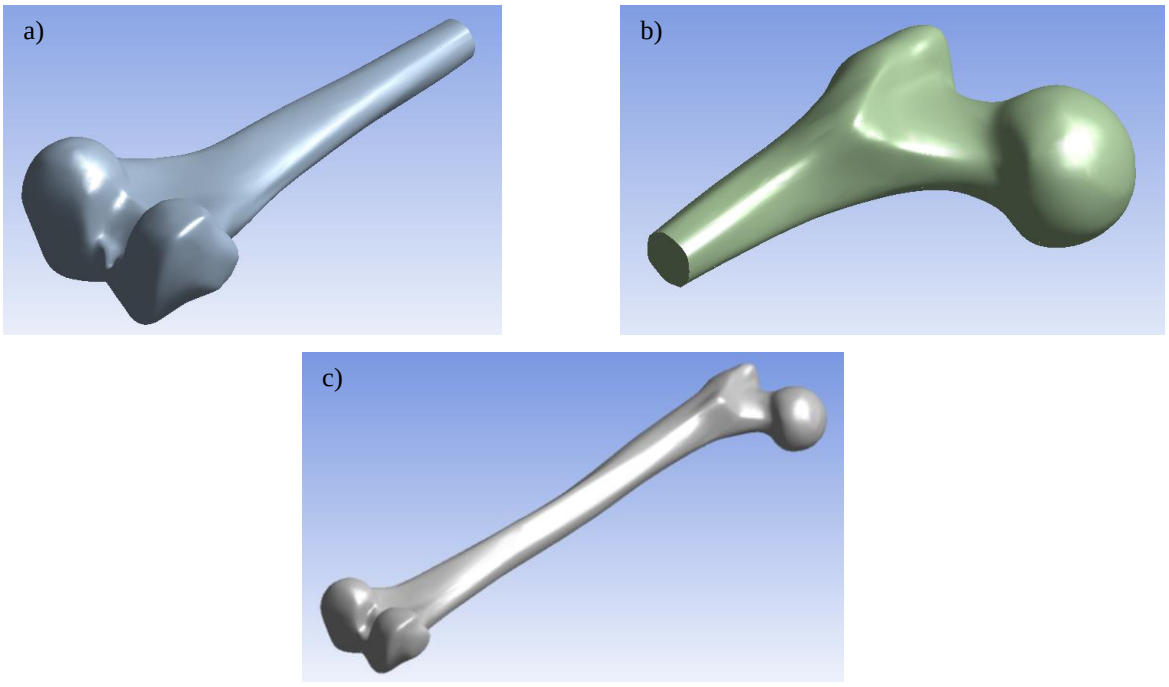

Figure 3-11: The three solid bodies used to form the model of a human femur bone; a) cancellous bone distal, b) cancellous bone proximal, and c) cortical bone.

	Young's Modulus of Elasticity [GPa]	Density [kg/m^3]	Poisson's Ratio
Cortical Bone	16.0	1700	0.4
Cancellous Bone	0.50	320	0.15

Table 3-1: Material properties of cortical and cancellous bone used in finite element simulation [24, 25].

3.3.2 Boundary Conditions

The femur bone must be constrained in a similar fashion as if it were attached to a human patient at the hip and knee. One way to approximate this constraint would be to cantilever both the proximal (hip) and distal (knee) ends of the femur bone. The exact locations where these supports were imposed on to the actual femur bone model in ANSYS are depicted in Figure 3-12.

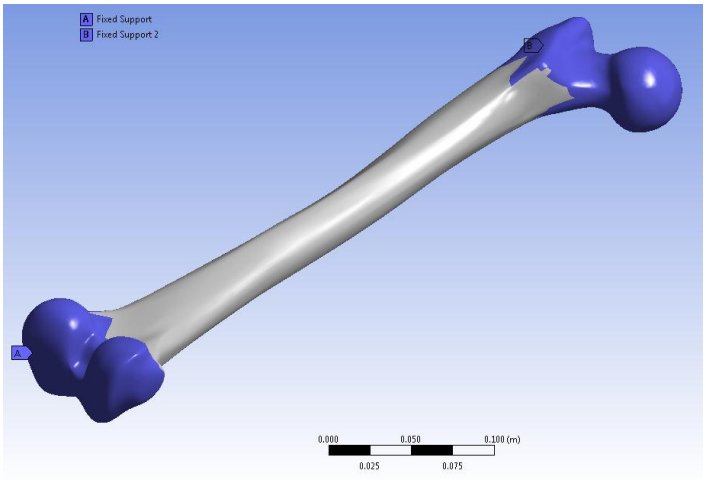

Figure 3-12: Boundary conditions applied to the femur bone model in ANSYS.

3.3.3 Load Application

To simulate the force and torque experienced by the bone during a drilling operation, the addition of a force load and torque load was required. To expand this investigation to include several different orthopaedic drilling situations, the force and torque loads would be applied to three different locations along the femur bone. The first location was mid-diaphysis or halfway along the bone. This is a site where much drilling is done for the insertion of screws to hold plates and attach bone fragments when repairing femoral shaft fractures [46]. This is also the location of drilling that will result in the greatest displacement and the highest stress. The second site of interest was at the proximal end of the bone (where the femur joins the hip). This is a

location that also requires a great amount of drilling during routine orthopaedic surgeries involving proximal femoral neck fractures or during hip replacement surgery [39-46]. The final drilling site that was investigated is at the distal end of the femur bone (where the bone joins the knee). This location is used in orthopaedic drilling for the placement of screws to repair distal femoral neck fracture or during total and partial knee replacement surgery. A visual representation of these locations on the femur bone model is shown in Figure 3-13.

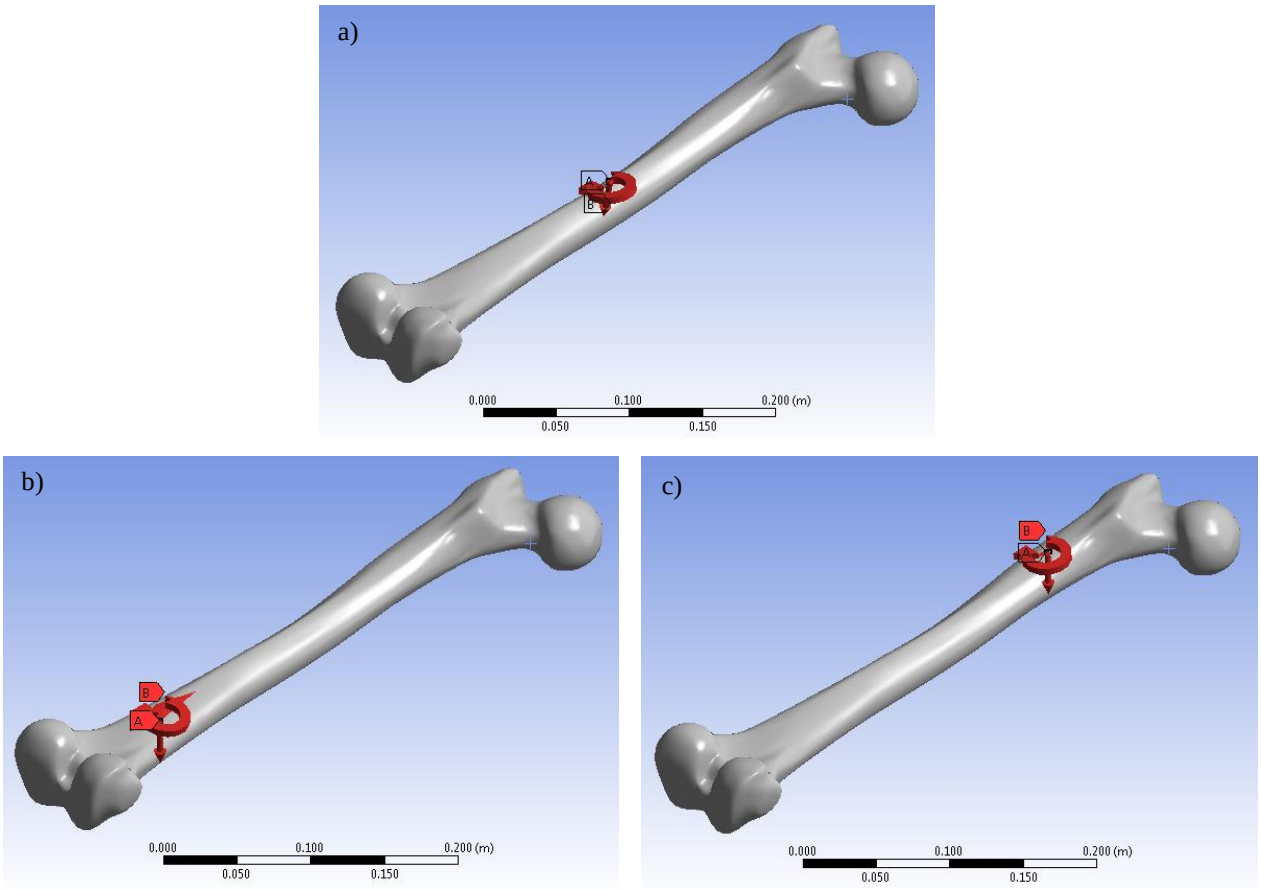

Figure 3-13: Applied force and torque locations on the femur bone model: a) mid-diaphysis, b) distal end, and c) proximal end.

At each of the three locations depicted in Figure 3-13, a perpendicular force and clockwise torque were positioned. The magnitude of this force and torque is based on the calibrated empirical models presented previously. For simplification, it was assumed that the drill would be entering perpendicular to the bone face. This is again justified since it is in agreement with many orthopaedic drilling practices.

3.3.4 Meshing

In ANSYS, the parameters of the discretised elements that form the mesh can be specified by the user. Of these parameters, only two are of interest for this simulation; namely, the element shape and element size.

The element shape defines the specific geometric shape of the element. For most three dimensional applications the shape of the elements are one of three different formations: tetrahedral, hexahedral, and pentahedral. Figure 3-14 provides a visual of these element shapes. In general, the FEA software that is being used selects a default element based on the type of analysis (mechanical, thermal, etc.) and the geometry of the model. The user then has the option to change the element type if another element shape is desired. In the case of this simulation, the default tetrahedral element shape was maintained. An image of the solid model with the default tetrahedral element mesh is presented in Figure 3-15.

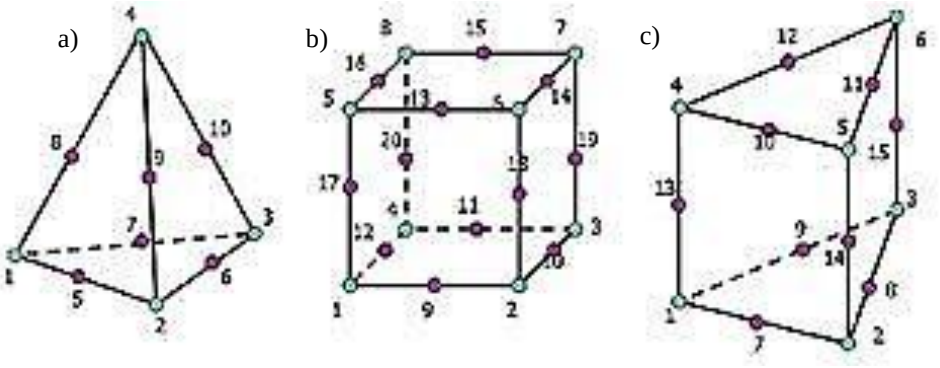

Figure 3-14: The three common element shapes used for 3D FEA analysis; a) tetrahedral, b) hexahedral, and c) pentahedral.

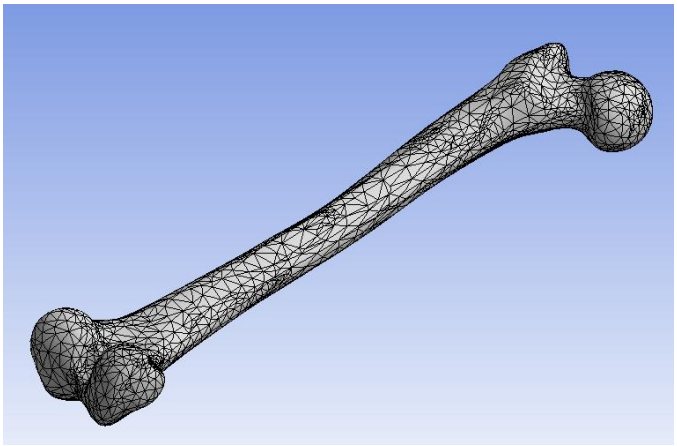

Figure 3-15: A screen shot of the default element shape and size as established by ANSYS.

The element size is one of the more important parameters in a finite element analysis. It is the size of the element that dictates the precision of the results as well as the computational expense of the analysis. Again, this parameter is often chosen as a default by the FEA software based on the type of analysis and the geometry of the solid model. As it applied to this simulation, a default element size of 10mm was instated. This is the element size presented in Figure 3-15. To determine if the default element size is ideal, it is often advantageous to conduct a mesh sensitivity analysis.

3.3.5 Mesh Sensitivity Analysis

To conduct a mesh sensitivity analysis, the femur bone was loaded with a realistic force and torque at the mid-diaphysis point of the bone. The maximum deflection as a result of these applied loads was measured and utilized as the dependent variable of the sensitivity analysis. The default mesh size provided by the software was 10mm. This was adjusted from 4mm to 32mm to determine the sensitivity of the mesh. The results of this analysis are presented in Figure 3-16. This figure displays a table providing the mesh size, maximum deflection, number of nodes, and number of elements as well as a plot of mesh size versus maximum deflection.

Mesh Size [mm]	Maximum Deflection [mm]	# of Nodes	# of Elements
32	0.031289	39711	20268
30	0.030918	39937	20370
28	0.031269	40668	20753
26	0.029547	41012	20903
24	0.034202	41415	21127
22	0.034051	42407	21620
20	0.03592	43651	22329
18	0.032445	45218	23152
16	0.033165	46969	24153
14	0.033417	48948	25285
12	0.034339	52508	27348
10	0.036735	59646	31679
9	0.037137	63365	33833
8	0.035285	70242	37924
7	0.035741	77955	42560
6	0.033062	93484	51982
5	0.03323	114629	64515
4	0.034102	153936	88022

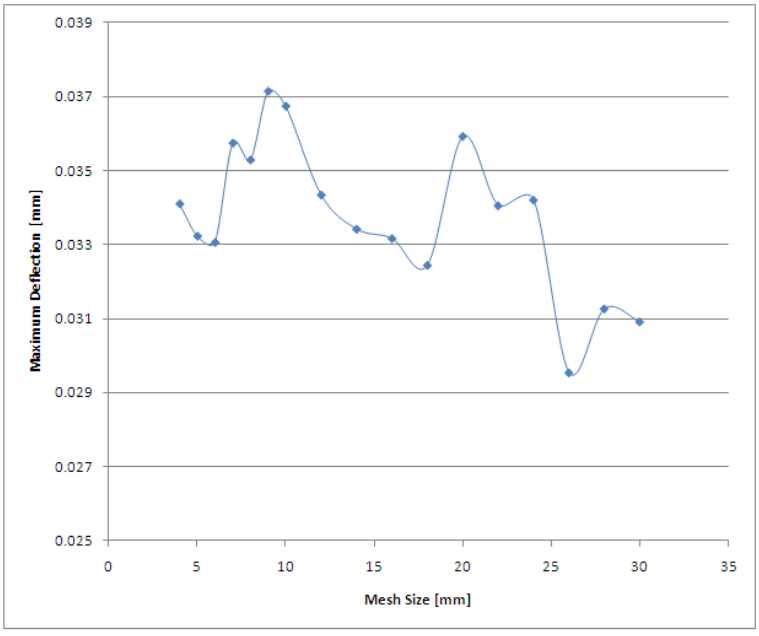

Figure 3-16: A plot of the values obtained via a mesh sensitivity analysis.

As can be observed, a majority of the data appears to be oscillating about a deflection value of approximately 0.035mm. The mesh sizes that create this oscillation can be observed to range from 4mm to 24mm. Figure 3-17 provides a depiction of this occurrence. It can thus be concluded that a mesh size less than 24mm will provide near equivalent results to a mesh size of 4mm. This would allow for simulations to be performed using a much coarser mesh size, say 22mm for example, and obtain an accuracy of the results approximately equal to that of the accuracy of results obtained using a much finer mesh size. The benefit to conducting the simulation using the coarser mesh would be a significant reduction in computational time which leads to a higher efficiency of data collection and analysis. It was decided that a mesh size of 22mm would be used to conduct this simulation.

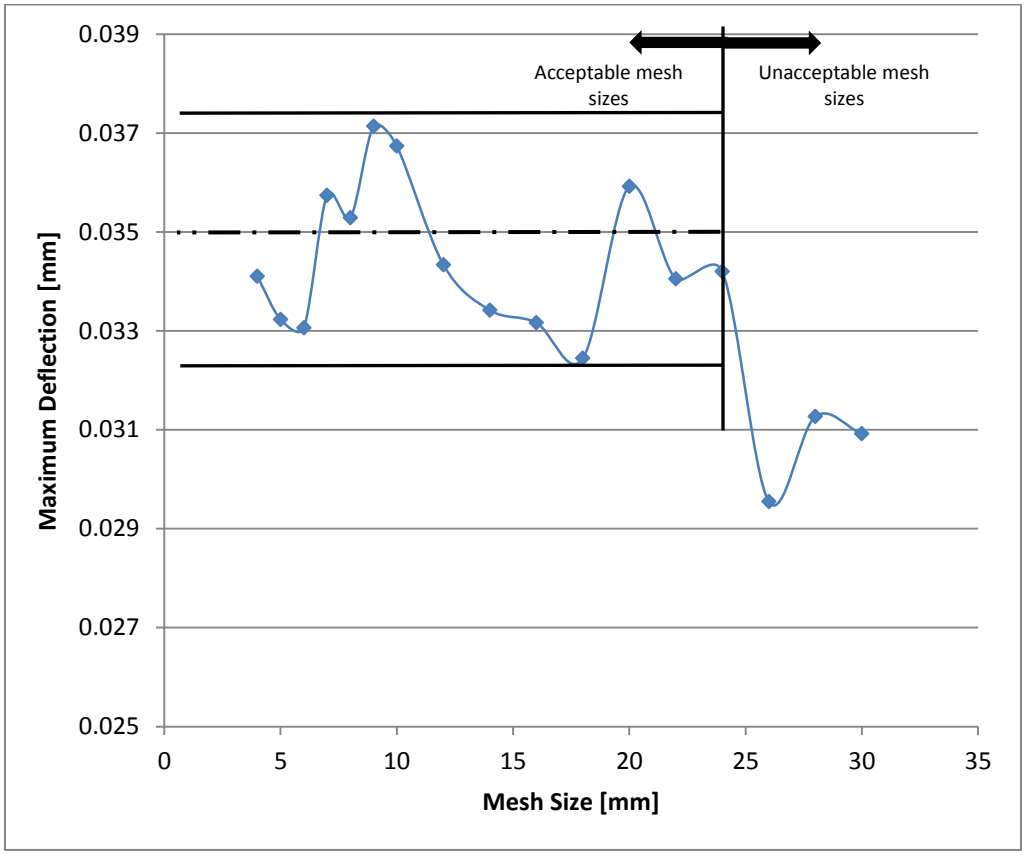

Figure 3-17: Plot of mesh size vs. maximum deflection indicating the mesh size cut-off value.

4 Experimentation

An experiment was designed to collect data that was used to calibrate and validate the mechanical force and torque prediction models as well as train and validate the neural network prediction models. This experiment was designed to collect the vertical or thrust force and the torque about the z-axis during the drilling of bone. Section 4.1 of this chapter will expand on the design of experiments outlining the experiment classification, experimental procedure, model parameter definition, and the model calibration procedure. Section 4.2 will introduce the experimental set-up expanding on the experimental equipment used: measurement device and data acquisition, CNC drill, drill bit, and bone specimen. In Section 4.3, an issue with the experimental set-up, drill misalignment, will be discussed at length. This is followed by Section 4.4 which outlines the methodology utilized to determine if the experimental data could be considered as normally-distributed. Section 4.5 presents the techniques used for experimental data processing including data isolation, normalization, and filtering.

4.1 Design of Experiments

The design of experiments procedure is an essential characteristic to any experimental process. It is through the design of experiments methodology that the type of experiment is defined, the components of the experiment are described, the experimental procedure is outlined, and the experimental factors are selected. In other words, the design of experiments fully defines and structures the experiment as to reduce the introduction of bias and to achieve the most accurate and statistically significant results.

4.1.1 Experiment Classification

To calibrate the drilling thrust force and torque prediction models, a two factorial experiment was designed with two levels per factor. The motivation for designing a two factorial experiment was that the model to be calibrated is a function of two independent variables: feed rate and spindle speed. Additionally, it was decided that two levels per factor would be sufficient to properly calibrate the prediction model while maintaining a relatively low number of experimental combinations. This created a total of four factorial runs. It was later decided to add a fifth factorial run that would help in strengthening the generalization of the models. Finally, it

was decided that ten replicas or repeats for each factorial run would provide enough data to correctly calibrate the model. Therefore, in total, five factorial runs with ten replicas per run resulted in a total of 50 experiments that were required for calibration. To obtain the validation data, two additional factorial runs also with ten replicas were used.

In order to prevent the possibility of introducing any bias into the experiment, the 50 experiments were run randomly. This was achieved by using a number randomizer to assign a random sequential number to each of the experiments and performing the experiments in the order that was assigned. The 20 validation experiments were randomly selected using the same methodology.

4.1.2 Experimental Procedure

The model calibration and validation experiments were designed to capture two primary measurements while drilling bone: thrust force and torque about the z-axis. It was initially decided that this data would be obtained by transverse drilling through the first layer of cortical bone, passing through the cancellous bone, and then through the second layer of cortical bone as the drill exited. This procedure is known in orthopaedic surgery as drilling *bi-cortically* (Figure 4-1a). After this method was attempted several times and the data collected, it was realized that only penetration through the first layer of cortical bone was desired. This was due to the fact that transition from the cancellous bone into the second layer of cortical bone could not be properly centred with a centre drill and was, therefore, delivering unwanted results. Additionally, only the data from the drilling of the first cortical bone would be needed as it is relatively uncommon in standard orthopaedic surgical practices to drill bi-cortically [1]. For these reasons it was decided that transvers drilling through only the first layer of cortical bone into the cancellous bone would be the method followed for experimental data collection. This method of drilling is known as *unicortical* drilling in orthopaedic surgery (Figure 4-1b).

The experimental procedure for obtaining the thrust force and torque data is outlined through the following steps:

1) Remove the bovine bones from the freezer in which they are stored and place them out in the open to allow them to rise in temperature to room temperature.

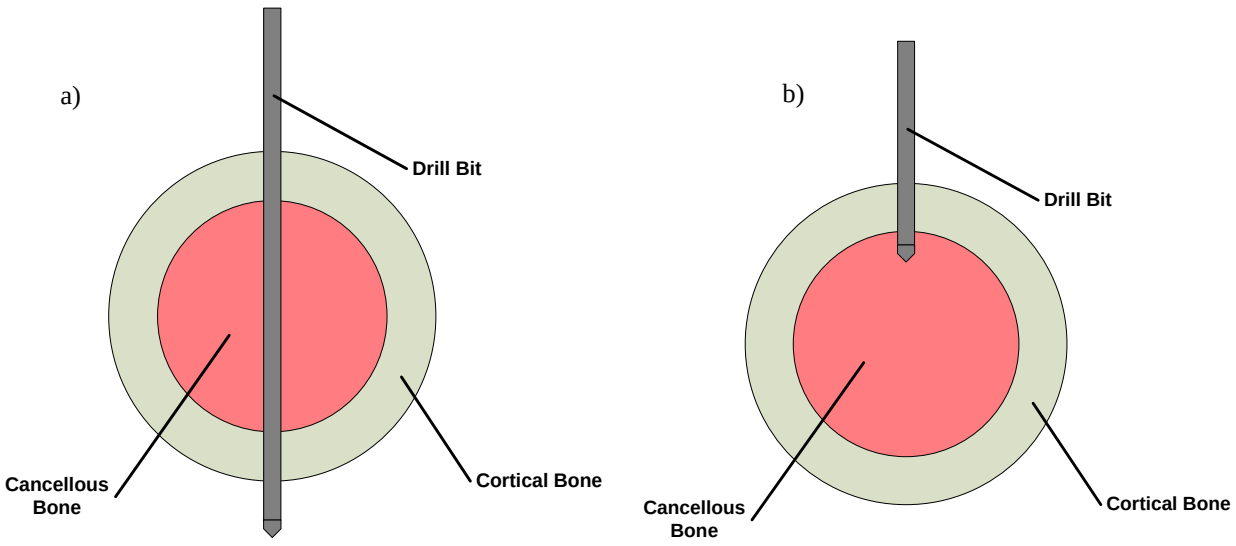

Figure 4-1: The orthopaedic drill penetrating a cross-section of a bone a) bi-cortically, and b) unicortically.

2) Select and load a bone specimen into the vice of the CNC machine. Ensure that the specimen is clamped firmly in place and that the clamp is firmly secured to the table.

3) Load the center drill bit into the CNC drill chuck and lock tightly.

4) Position the drill bit centered approximately 20mm above the outer layer (cortex) of the bone specimen.

5) Set the CNC drill spindle speed to its maximum rotational speed.

6) Center drill a small hole in the outer layer of the bone. This hole is used to properly align the surgical drill bit as it enters the bone.

7) Retract the drill to its home position.

8) Replace the center drill bit with the surgical drill bit. Confirm that the bit is securely locked in the drill chuck.

9) Once again, position the drill bit centered approximately 20mm above the bone specimen.

10) Set the CNC drill's spindle speed to the desire speed for that particular experiment. Recall, this value may change from experiment to experiment depending on the factorial run of interest.

11) Set the CNC drill's feed rate to the desire speed for that particular experiment. Recall, this value may change from experiment to experiment depending on the factorial run of interest.

12) Start the CNC drill and the force/torque sensor simultaneously. Observe as the drill travels towards the bone specimen. Continue to watch the drill bit as it progresses through the cortical bone. Once the drill penetrates through the cortical bone and enters the cancellous bone, stop the feed of the CNC machine.

13) Return the CNC drill to its home position and stop the data collection once the drill exits outside the bone. Turn off the drill spindle.

14) Remove the surgical drill bit from the CNC drill and clean it thoroughly making sure the flutes are clear of clogged material.

15) Remove the bone specimen from the vice.

16) Save and store the experimental data file for later analysis.

17) Repeat steps 2 through 16 for all factorial runs.

4.1.3 Model Parameter Definition

Before model calibration and validation experiments could begin, the model parameters needed to first be defined. This involved defining the range of the independent variables and establishing the model's constants. The chip-evacuation force and torque prediction models have been repeated here for convenience.

$$F_{Model} = F_c(z) = F_o e^{\left(\frac{\eta \mathrm{MD}}{S}\right)z}, \tag{4.1}$$

$$T_{Model} = T_c(z) = \frac{R\mu_w l_w F_o}{\mathrm{M}}\left(e^{\left(\frac{\eta \mathrm{MD}}{S}\right)z} - 1\right), \tag{4.2}$$

where:
$$\mathrm{M} = \left(l_f \mu_f + l_h \mu_f + l_r \mu_f + l_w \mu_w \mu_f \sin\theta\right). \tag{4.3}$$

As it can be seen above, the force and torque prediction models are both a function of the drill's operating parameters; namely they are a function of the drill's spindle speed and feed rate. Consequently, these values represented the independent variables used for experimental model

calibration and validation. The drill's feed rate and spindle speed have large variations as they apply to orthopedic surgery applications. These operating parameters rely heavily on the surgeon performing the surgery, the equipment that is being used, and the application that it is being used for. For these reasons, the literature was used to select the independent variables for experimentation. Referencing the literature, Table 4-1 displays a list of the 5 spindle speeds and feed rates that were used for the calibration experiments [9, 13, 18].

Feed Rate (*f*) [mm/sec]	**Spindle Speed (*N*) [RPM]**
1.0	1000
1.5	1100
1.5	1250
1.75	1500
2.0	1500

Table 4-1: List of selected feed rates and spindle speeds

In addition to the identification of the experimental operating parameters, the chip-evacuation force/torque model's constants needed to be defined. This involved an inspection of the drill bit's geometry to determine the contact lengths and area of the drill bit's flutes. OmniMet software (Buehler, Lake Bluff, IL) was used to measure these lengths and area using an image at 60x magnification. Each of the contact lengths were measured and are shown in Figures 4-2a and 4-2b. From Figure 4-2a it can be seen that the contact length of the flute face, l_f, was found to be 1.16mm (C2), the length of the flute heel, l_h, was measured to be 1.16mm (C3), and the length of the flute root, l_r, was observed to be 0.29mm (C4). From Figure 4-2b it can be seen that the contact length of the wall, l_w, was found to be 1.91mm (D6). The cross-sectional area of the flute, S, using Figure 4-2c was calculated and the resulting value was found to be 1.46mm^2. See Appendix A for calculation. The final geometric measurement that was required for the model was the angle between the flute face and the cutting plane, θ. This angle was measured using the lengths, D4 and D5, obtained from Figure 4-2d and was found to be 26.7°. See Appendix A for calculation.

The final model parameter that needed defining was the η-value constant. This value is a ratio between lateral and axial pressures and is a material property of the material of which the pressure is applied. As it relates to drilling, this constant defines the amount of axial pressure that is converted to radial pressure along the drill flute walls and the walls of the hole being drilled.

This value is unknown for most materials but, as shown by Long, can be approximated for powder like materials as the material's Poisson's ratio [37]. As with all non-homogenous materials, cortical bone has a small variation in its Poisson's ratio value. This variation is dependent on the age, weight, sex, etc. of the patient. For reasons of simplicity, the value of η was selected as 0.4; the approximated value of Poisson's ratio of cortical bone as reported in the literature [24].

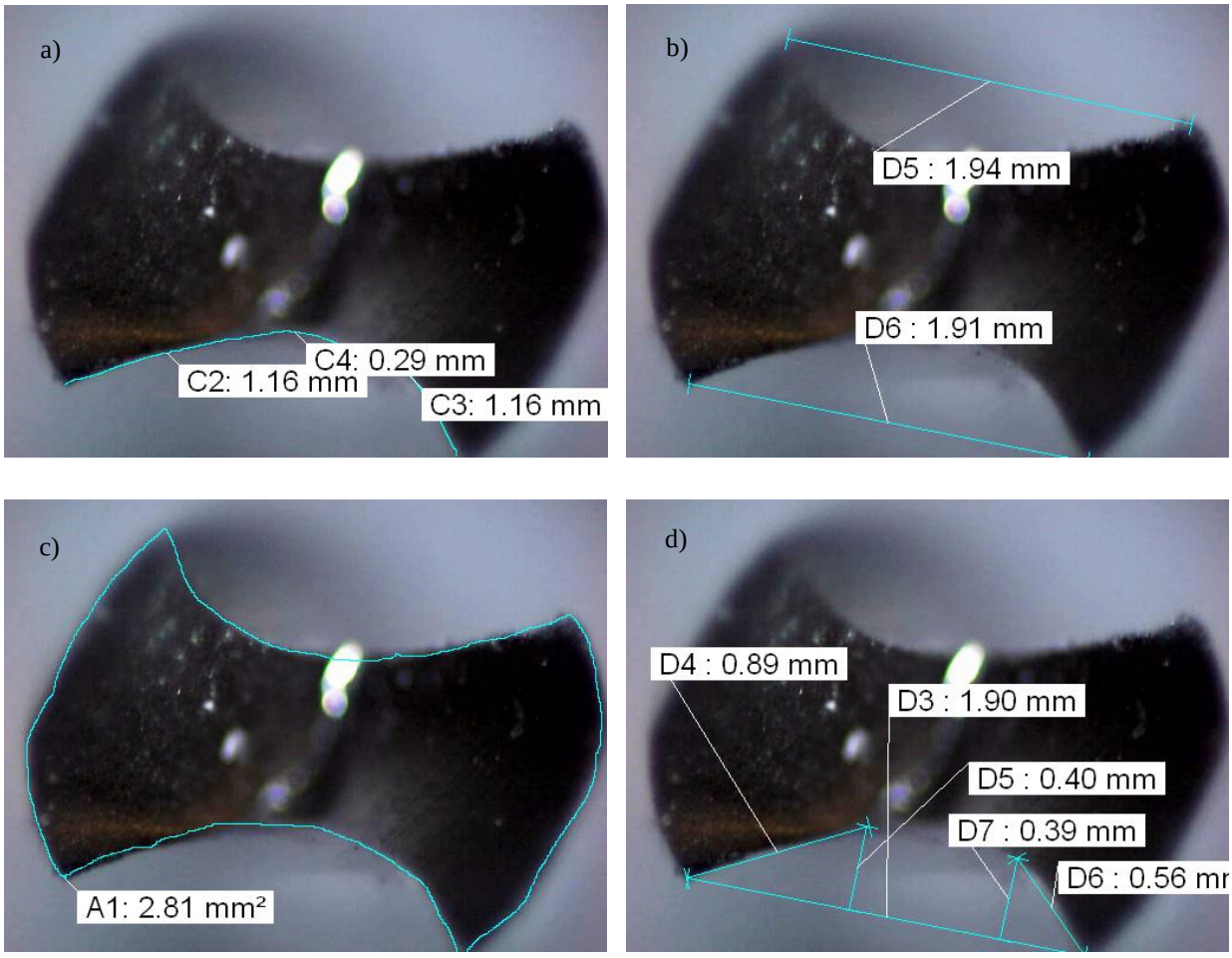

Figure 4-2: The 60x magnification image of the orthopaedic twist drill used for experimentation: a) the face, heel, and root contact lengths, b) the contact length of the wall, c) the cross-section area, and d) the angle between the flute face and cutting plane.

4.1.4 Model Calibration Procedure

To properly calibrate the force and torque prediction models, a systematic statistical and regression analysis was performed. The following steps outline this calibration procedure:

1) Perform a nonlinear least-squares optimization to obtain μ_f and μ_w for each set of operating parameters. This is achieved using the following form:

$$\min_{\mu} \sum_{z} \left[\left(F_{Model} - F_{Exp} \right)^2 + \left(\frac{T_{Model} - T_{Exp}}{R} \right)^2 \right], \tag{4.4}$$

$$\mu = \begin{bmatrix} \mu_f & \mu_w \end{bmatrix},$$

where F_{Exp} and M_{Exp} are the experimental force and torque signals, respectively.

2) Using the following power law model:

$$\ln \mu_{fi} = a_0 + a_1 \ln f_i + a_2 \ln N_i + a_3 \ln f_i \ln N_i, \tag{4.5}$$

$$\ln \mu_{wi} = b_0 + b_1 \ln f_i + b_2 \ln N_i + b_3 \ln f_i \ln N_i,$$

where a_0 through a_3 and b_0 through b_3 represent the coefficients of the power law. The coefficients of friction for each factorial run obtained from step 1 form a system of equations with 5 equations and 4 unknowns for both μ_f and μ_w. These systems take on the following form for $i = 1, 2, \ldots 5$:

$$\ln \mu_{f1} = a_0 + a_1 \ln f_1 + a_2 \ln N_1 + a_3 \ln f_1 \ln N_1, \tag{4.6}$$

$$\ln \mu_{f2} = a_0 + a_1 \ln f_2 + a_2 \ln N_2 + a_3 \ln f_2 \ln N_2,$$

$$\vdots \qquad \vdots \qquad \vdots \qquad \vdots$$

$$\ln \mu_{f5} = a_0 + a_1 \ln f_5 + a_2 \ln N_5 + a_3 \ln f_5 \ln N_5,$$

and,

$$\ln \mu_{w1} = b_0 + b_1 \ln f_1 + b_2 \ln N_1 + b_3 \ln f_1 \ln N_1, \tag{4.7}$$

$$\ln \mu_{w2} = b_0 + b_1 \ln f_2 + b_2 \ln N_2 + b_3 \ln f_2 \ln N_2,$$

$$\vdots \qquad \vdots \qquad \vdots \qquad \vdots$$

$$\ln \mu_{w5} = b_0 + b_1 \ln f_5 + b_2 \ln N_5 + b_3 \ln f_5 \ln N_5.$$

Solving the above systems of equations for a_0 through a_3 and b_0 through b_3 completes the power law and allows one to obtain μ_f and μ_w for any feed rate (f) and spindle speed (N).

4.2 Experimental Set-up

To best capture the drilling force and torque data required to drill bone, the experiment was setup as shown schematically in Figure 4-3a and pictorially in Figure 4-3b. A toolmaker's vice was mounted atop a 6 degree-of-freedom force/torque transducer. The force/torque sensor was connected an industrial standard architecture (ISA) data acquisition board mounted inside a personal computer. A bone specimen were cut to approximately 2 inches in length was inserted into the vice and locked into place. The sensor and vice assembly was secured directly under the drill of a computer numeric controlled (CNC) drilling machine. The alignment of the drill directly above the centre of the sensor was crucial since any misalignment could have resulted in the thrust force and torque being broken up into multi-directional components of the actually force. Another area of the setup that was important was making sure that the vice, sensor, and bone specimen were all rigidly connected and were unable to move.

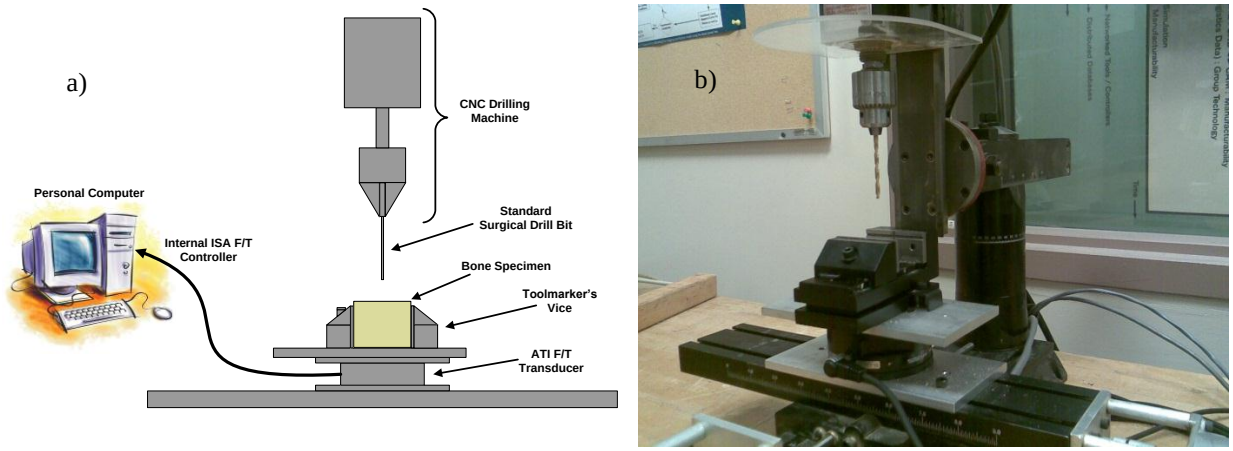

Figure 4-3: Experimental set-up depicted: a) schematically and b) pictorially.

4.2.1 CNC Drill

The CNC drill utilized for the cutting operation of this experiment was a CNC converted Sherline Model 2000 Deluxe 8-Direction Mill (Sherline Inc., Vista, CA). The Sherline spindle boasts a high-torque 90V DC motor with electronic speed control which is continuously variable from 70 to 2800 RPM [47]. The manual Sherline table-top drill was converted into a computer numeric controlled system with the addition of a custom made controller and three matching servo motors to control each of the feed screws which governed the three degrees of freedom. The software utilized by the CNC machine's position and velocity controller is DeskNC (Carken

Inc., Syracuse, NY). DeskNC is a G-Code interpreter that, when combined with the CNC controller, provides real time feedback of both position and velocity.

4.2.2 Transducer and Data Acquisition

The transducer used to obtain the experimental data was the Gamma ISA F/T-16 Intelligent Multi-axis Force/Torque Sensor System (ATI Industrial Automation Inc., Apex, NC). The Gamma transducer has a 16-bit analog-to-digital signal resolution and is capable of capturing 6 degrees-of-freedom for both force and torque. This transducer has a rated 1/80 N and 1/3200 Nm resolution for thrust force and torque about the z-axis, respectively. Additionally, the sensor can withstand a maximum force of ±4100N along the z-axis and a maximum torque of ±82N/m about the z-axis [48].

The data from the transducer was transmitted, via the transducer cable, to the internal ISA F/T controller/data acquisition card inside the PC where the force and torque data was available to be processed. The ISA card processed the data at a sampling rate of 1.2 KHz−7.8 KHz [48]. The software interface provided with the hardware utilizes Microsoft Excel to capture the data transmitted from the sensor. This Excel interface also provided the capability to stop and start data collection, define the length of time desired for data collection, reset the stored data, and tare the sensor. The spread sheet delivered x, y, and z-axes force and torque data as well as a corresponding sequence value that could be converted into time. Additional outputs included the total time elapsed, total samples read, and samples read per second. It also provided a vector depiction of the force and torque as it is applied to the sensor that visually updates as the forces change. A screen shot of the data collection interface is displayed in Figure 4-4.

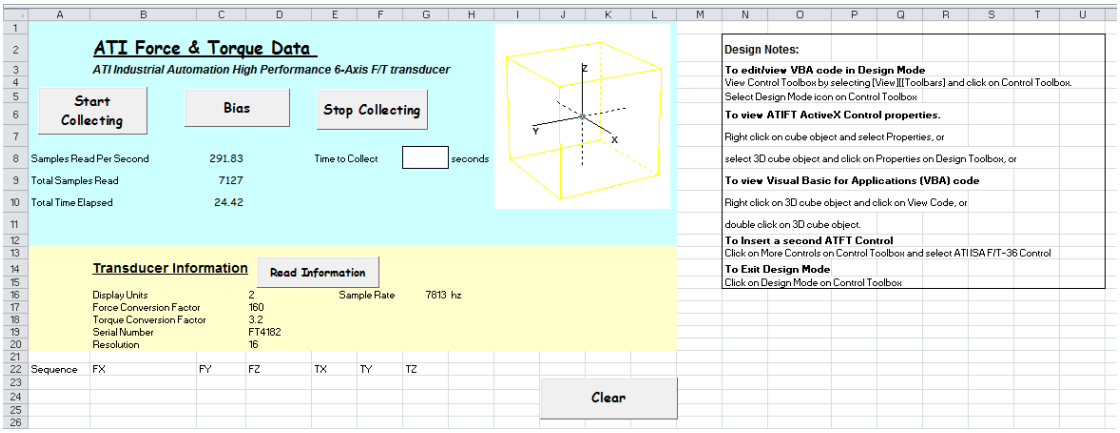

Figure 4-4: Screen shot of the Microsoft Excel data acquisition user interface.

4.2.3 Drill Bit

The drill bits used for this experiment were selected as the same standard drill bits used by orthopedic surgeons for the drilling of bone [15]. Typical surgical drill bits range in diameter from 1-5mm and have a length of between 60−200mm. The drill bit selected for this experiment was a two flute, 2.7mm diameter, stainless steel, plain shank/Jacob chuck twist drill bit, 130mm in length (Synthes Inc., West Chester, PA). Additionally, as is the case with most surgical drill bits, the drill bits used had 90° point angles. Each of the drill bits utilized for experimentation were unused and came straight from the manufacturer. A photograph of one of the drill bits used for these experiments is provided as Figure 4-5.

Figure 4-5: A stainless steel, 2.7mm diameter orthopaedic surgical drill bit used for experiments.

4.2.4 Bone Specimen

The bones selected for this experiment were bovine femurs. These bones were selected due to their likeness to human bone in both geometry and material properties [12]. Additionally, bovine femurs are affordable and readily available from most local butcher shops. Both epiphysis of the bovine femur were removed leaving only the mid-diaphysis. The mid-diaphysis was cut into approximately 2” diameter disc specimens to be used for experimentation. The thickness of the cortical bone varied from specimen to specimen which provided for a large range of cutting depths. A picture of one of the femur bone specimens loaded in the vice ready for experimentation is shown in Figure 4-6. The femurs were stored in an industrial freezer and maintained at -37°C prior to experimentation. Initially, each specimen was heated to human body temperature of 38°C using a 0.6% NaCl warming bath [49]. This temperature proved to be quite difficult to maintain as cooling began immediately once the bone was removed from the bath. Also, the heating of the bone in the warming bath created a significant mess that could have

resulted in a bio-hazard. It was discovered that, based on the literature, little accuracy would be lost in the results if the experiments were performed at room temperature [49]. Thus, at the time of experimentation, each specimen was removed from the freezer and place on a table to be warmed to room temperature.

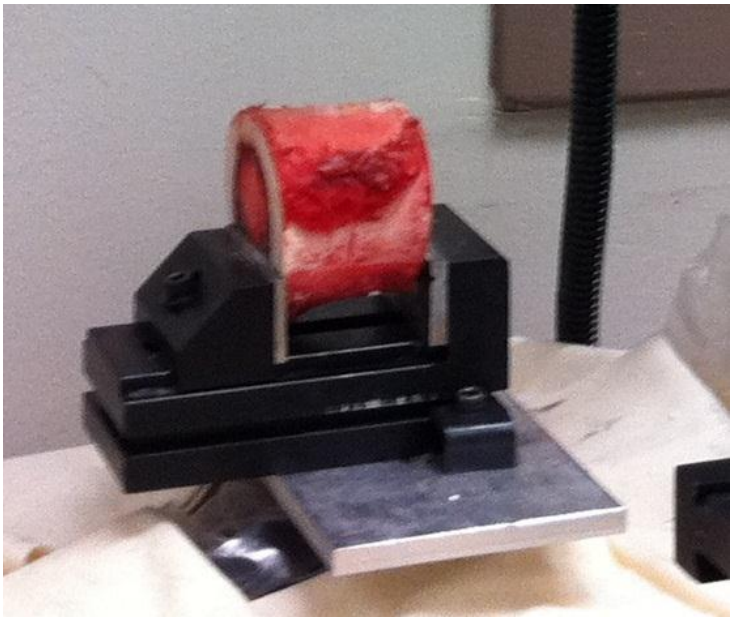

Figure 4-6: Bovine femur bone specimen loaded in the vice ready for experimentation.

4.3 Drill Misalignment

Throughout the calibration and validation experiments, six degrees-of-freedom were observed. Namely, these are the forces along the x-, y-, and z-axis and the torques about the x-, y-, and z-axis. Figure 4-7 depicts these axes with respect to the drill bit.

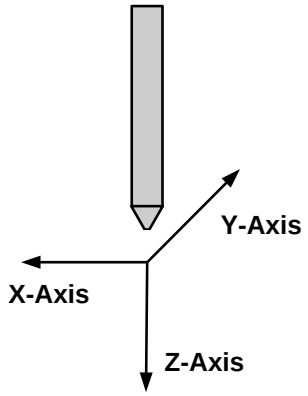

Figure 4-7: Drilling coordinate system.

Of these six independent measurements, one force and one torque component dominated – thrust force (the force along the z-axis) and cutting torque (the torque about the z-axis). The fact that these are the only two components of interested is well documented in the literature and can be experienced first-hand by anyone drilling a hole in any material [12]. This fact has become so accepted that most research papers written on the drilling process tend to omit the data for the x- and y-axis forces and torques with the understanding that this data is negligible. Similarly, these forces/torques will not be reported in this thesis.

Even though only the thrust force and torque about the z-axis were of interest, our experiments were performed using a six degree-of-freedom transducer. Thus, forces and torques along all three axes were recorded during the experiments with some interesting results. Initial experimental results demonstrated forces and torques about all three axes with a majority of the force and torque appearing along the z-axis and smaller but increasing forces and torques appearing along the x- and y-axes. An example of the data collected for all six degrees of freedom is shown in Figures 4-8 and 4-9.

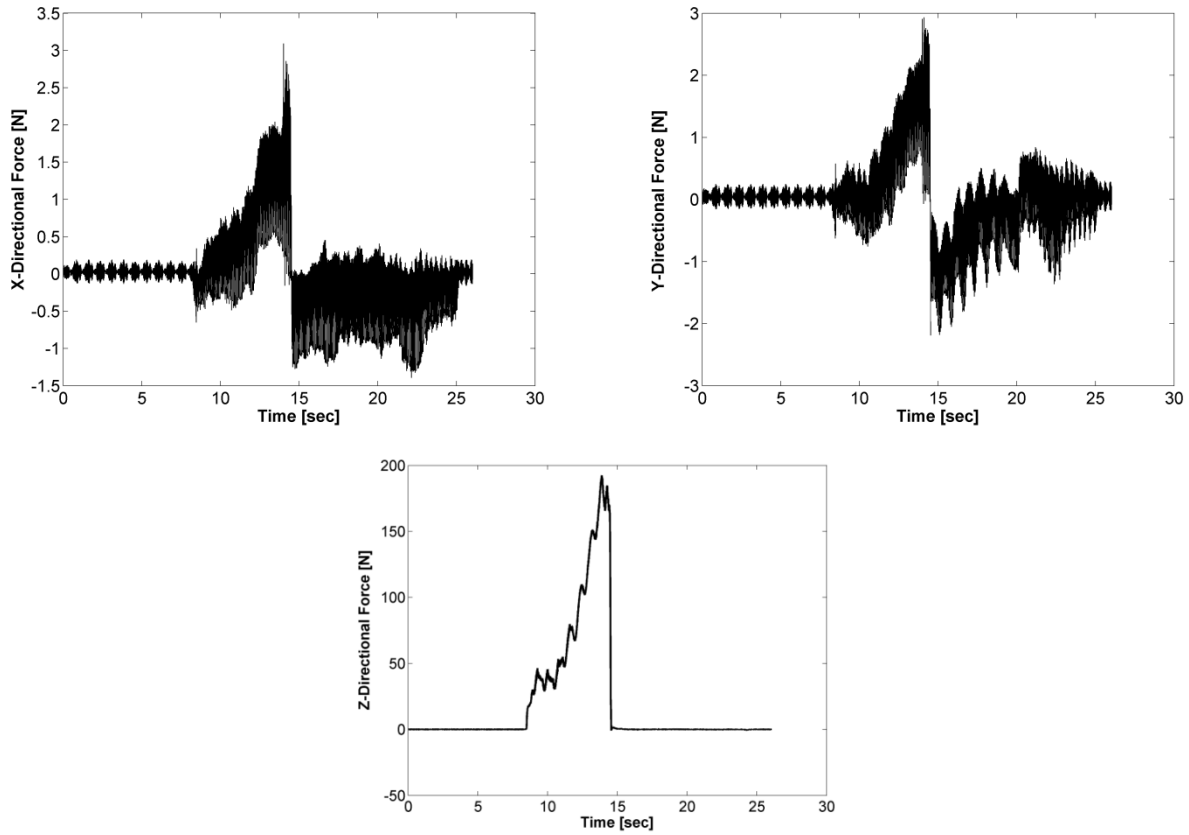

Figure 4-8: An example of data collected for x-, y-, and z-axis forces.

From these figures, the existence of x- and y-axes forces and torques are clear. For all four of these data sets, the signal is increasing from the time the cutting begins, peaks at the moment the drill bit breaks through the bone, then decreases as the drill returns to its home position. The present of these x and y forces and torques were attributed to two different forms of drill misalignment: drill path misalignment and drill shaft misalignment.

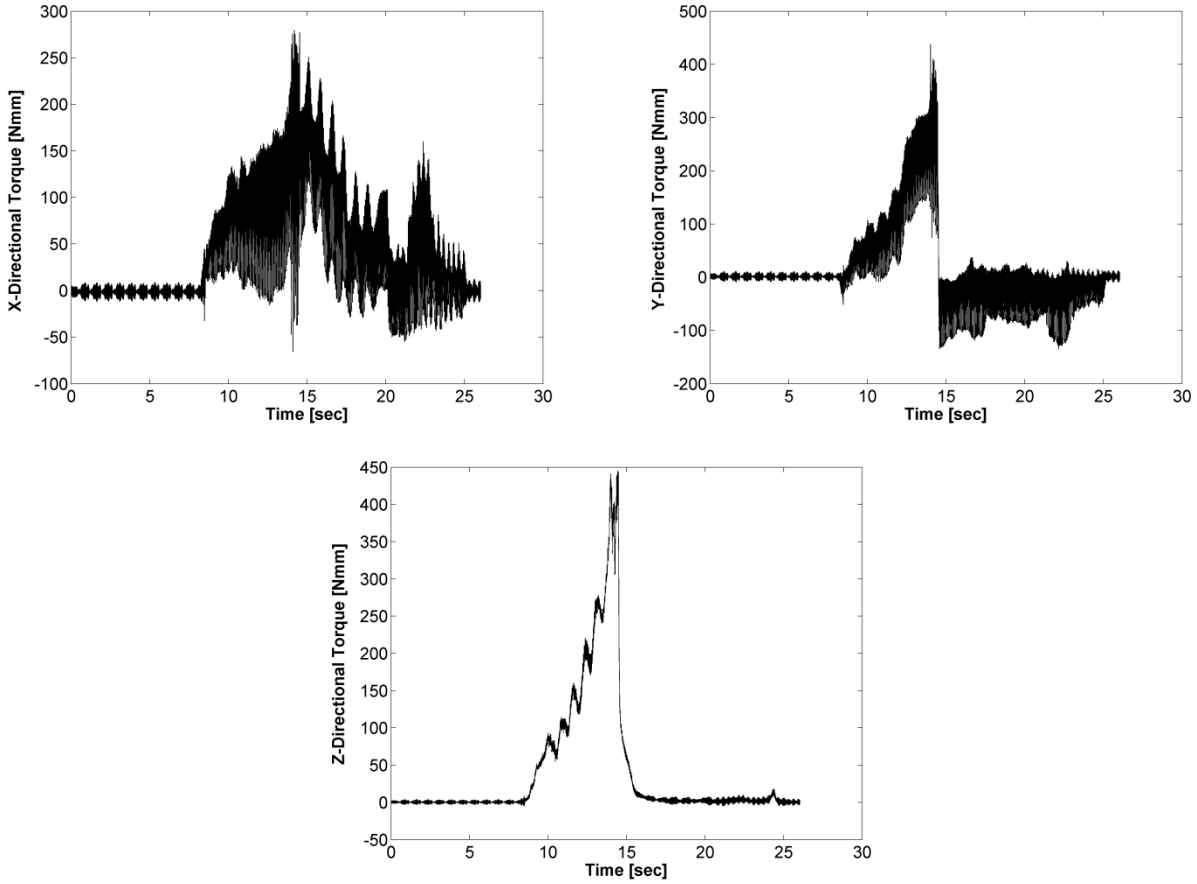

Figure 4-9: An example of data collected for x-, y-, and z-axis torques.

In ideal cutting conditions, the forces and torques about the x- and y-axis should oscillate, due to noise, around the zero value as the physical nature of the drilling process does not produce forces along these axes. One of the main requirements to achieve an ideal cutting condition is that the drill bit penetrates and travels the complete length of its cut exactly perpendicular to the material's surface. This means that the axis of the drill's path must be parallel to the z-axis of the sensor. Any deviation from this parallelism could result in forces and torques about the x- and y-axis. Furthermore, these forces and torque would be due to the contributions of the cutting force and would, in effect, lessen the force seen along the z-axis. An exaggeration of this misalignment

is depicted in Figure 4-10. Since a portion of the cutting force was being distributed to axes other than the z-axis, this issue needed to be addressed.

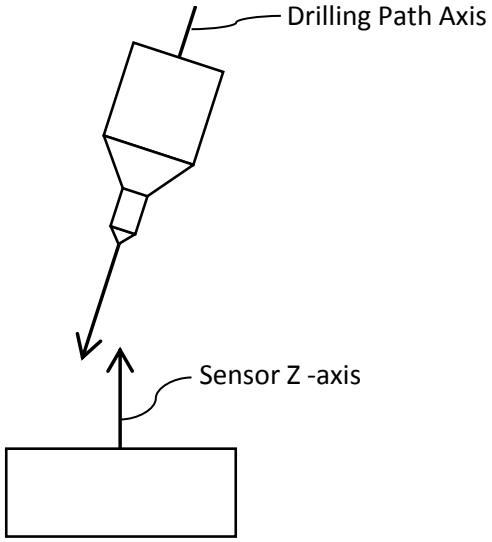

Figure 4-10: Exaggeration of drill axis and sensor axis misalignment.

The misalignment of the drill's path was measured using a marker based optical tracker (Optotrak Certus, NDI, Waterloo, Ontario) to determine the amount of misalignment present. This was done in an attempt to correct the error caused by this misalignment. The location of the force/torque sensor was marked as the frame of reference and a marker was placed on the axis of the drill shaft to measure its deviation from this reference frame. The deviation in position was measured capturing the x, y, and z coordinates relative to their starting positions. An experimental simulation was conducted to observe the drill descend approximately 140 mm from the home position, stop for a moment, and then ascend back to its starting location. The resulting measurements of this simulation are presented in Figure 4-11.

Figure 4-11 shows that as the drill descended from its home position to approximately 140 mm, the x and y positions were also being altered slightly. Specifically, it was recorded that the drills path deviated by approximately 1.8 mm in the x-direction and approximately 0.7 mm in the y-direction during the 140 mm decent in the z-direction. As the average bovine cortical bone thickness was approximately 10 mm, during the actually cutting of bone, an estimated 0.13 mm displacement and 0.05 mm displacement would result in the x- and y-direction, respectively.

Although these displacements are quite small in magnitude, we attributed this misalignment with the unexpected force and torque results observed along the x- and y-axes. Fortunately, this issue was easily resolved by simply manually adjusting the drill's path using the measurements acquired and square blocks to confirm its parallelism to the sensor's z-axis.

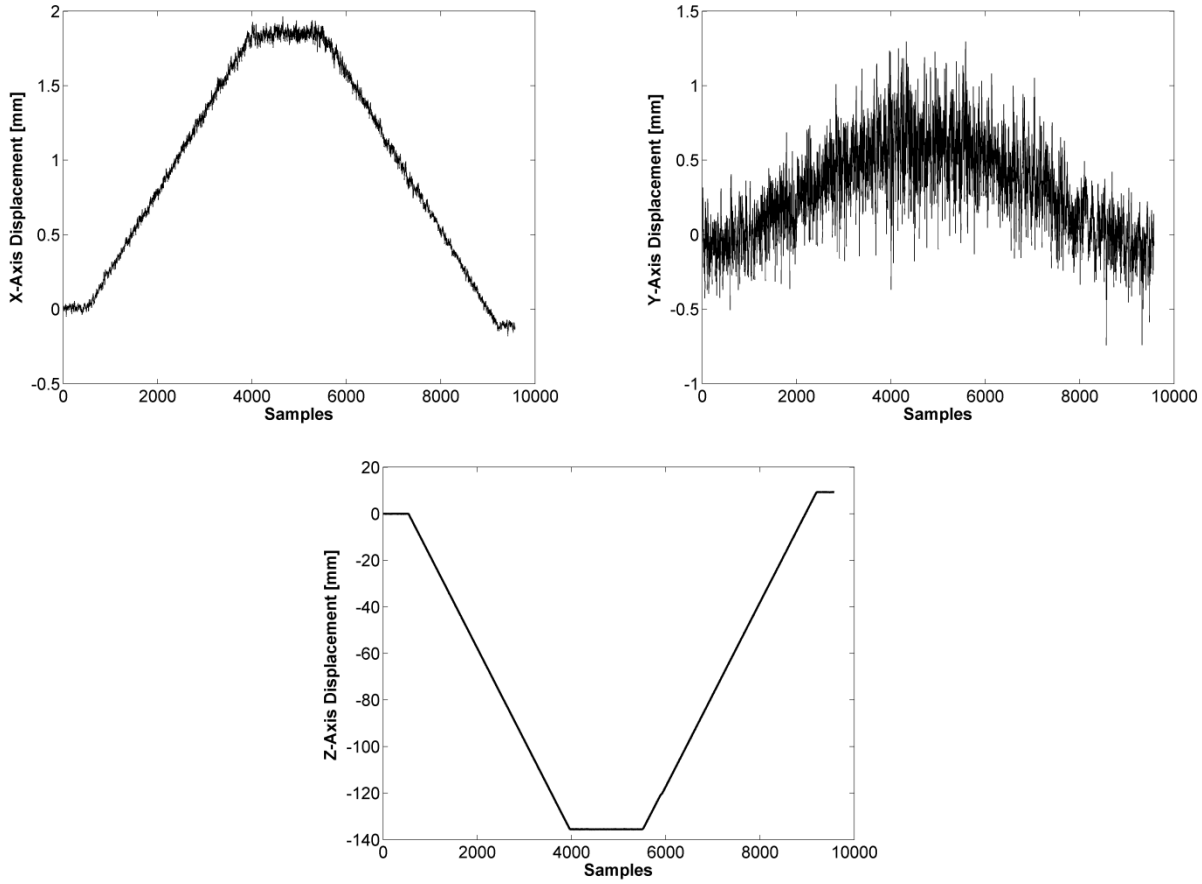

Figure 4-11: Displacement measurements in the x-, y-, and z-directions collected while simulating a drilling experiment.

Another issue of misalignment that occurred was the misalignment of the axis of the drill's path with the axis of the drill's shaft. An exaggeration of this misalignment is depicted in Figure 4-12. In this configuration, the drill's path is aligned (or parallel) with the z-axis of the sensor but the drill's shaft is misaligned (or antiparallel) with the z-axis of the sensor. This resulted in the drill travelling through the bone along a diagonal path at some small offset angle. This, once again, introduced forces and torques about the x- and y-axes. This misalignment was much easier to correct as all that was required was to place a level along the drill's shaft and manually adjust the positioning screws until parallelism was obtained.

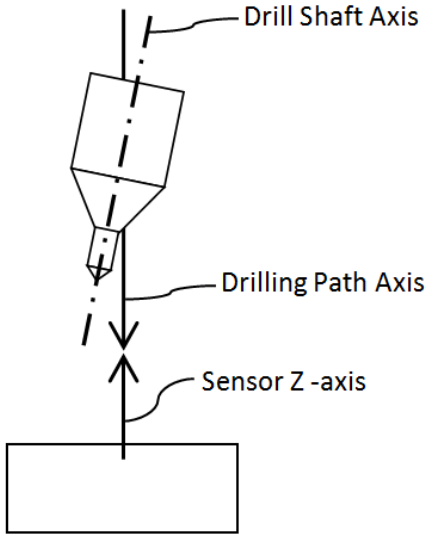

Figure 4-12: Exaggeration of drill shaft axis, sensor axis, and drill path axis misalignment.

After these two misalignments were properly addressed and corrected for, the existence of the x- and y-axes force and torque dissipated substantially. The remaining force and torque seen along the x- and y-axes were attributed to experimental noise and the small amount of misalignment that was still present in the system.

4.4 Data Test for Normality

Before any experimental data could be collected, it was important to establish that the experiment would produce unbiased or normalized results. If the acquisition of normalized data could not be established, this would have indicated an error in the experimental design. The following section will discuss the motivation, procedure, and results as the data was tested for normality.

4.4.1 Motivation and Procedure

As with the collection and analysis of any experimental data, it is important for the investigator to test and confirm that the random variable is statistically significant. A random variable is determined to be statistically significant if it can be shown, within some level of confidence, that it is unlikely to have occurred by chance [50]. The test conducted on the data to determine if it is statistically significant is called a *test of significance*. The test of significance is

then, typically, evaluated using a null hypothesis test which results in an acceptance or rejection of the declaration of significance.

One of most widely used test of significance is the *test of normality*. The test of normality is applied to a population to statistically determine if the population data is normally distributed. A population (or selected sample of the population) of a continuous random variable is said to be of a normal distribution (or Gaussian distribution) if the data, once plotted, congregates around the mean in the traditional bell-shape form. If the data is normalized, as it often is, the mean value will be zero, the standard deviation will be one, and approximately 95% of the population will be within two standard deviations from the population mean. It has been reported that, to accurately conclude that a population is normally distributed, a sample size of 30 or more random variables must be obtained and compared to test for normality [50].

4.4.2 Data Collection

To confirm that a random variable population of experimental data is normally distributed a sample size of 30 or more is required. These samples should be taken under the same operating conditions to substantiate that any variation in the data is random and cannot be attributed to the independent variables of the experiment. Specific to this experiment, the independent variables have been declared as the drill feed rate and drill spindle speed; these are the operating parameters that remained constant for all 30 samples. In order to extend the results of the normality test over the range of operating parameters that will be used to model the bone cutting forces and torques, it was important to define the values of the independent variables that were used to test for normality as the middle or average values of all the operating parameters. Additionally, all experiments would have to be performed with the same surgical drill bit. The fixed values for drill feed rate and spindle speed were decided to be 1.5 mm/sec and 1500 RPM, respectively. The drill bit selected was a 2.7mm diameter standard surgical twist bit.

In order to extend the results of the normality test to the experiments required to model the bone cutting forces and torques, the data that was to be tested for normality was extracted from the force clogging model. In other words, the signal data collected experimentally would be fed into the force prediction model and the results for each experiment would be compared for normality. This would allow for the collected data of bones of various geometries to be directly

compared. The clogging force prediction model that was used was a simplified version of the model introduced in Chapter 3. This simplified version of the clogging force model is as follows:

$$F_{\exp} = F_o e^{pz}, \tag{4.8}$$

where F_{exp} is the force signal acquired experimentally, F_o is the initial cutting force, p is the exponential constant based on geometric and material properties, and z is the dimensionless depth/diameter ratio. The F_o and p values from the above model were extracted from the experimental force signal data via a nonlinear least squares regression algorithm. This process was conducted for all 30 experiments resulting in 30 different initial cutting forces and 30 different exponential constants for the drilling of each bone specimen. Table B-1 of Appendix B displays these extracted values. It was these values that were investigated and statistically compared to determine normality.

4.4.3 Median Rank Test

There are several different approaches to testing a random variable for normality. The two that will be employed in this report are the *median rank test* and the *Chi Square* (or *goodness of fit*) test. Median rank tests use a probability plotting approach which plots the data on specifically constructed probability graph. Since this is a test for normality, the graph structure of choice was a normal probability graph. The data is ranked with respect to the median value with half of the data being greater than the median and half the data being less than the median. Once this data is plotted on the normal probability graph, an approximate straight line would indicate that the sample data is normally distributed.

Two median rank tests were performed on the experimental force data collected. The first test compared the initial cutting forces, F_o. The result of the median rank test for the initial cutting force is depicted in Figure 4-13. From this figure, it can be seen that the data does tend to distribute in such a way as to form a reasonably good straight line. Hence, it can be concluded that the initial cutting force values for these 30 samples are normally distributed.

The second of the median rank tests was performed on the exponential constant, p. The result of the median rank test for normality of this variable appears in Figure 4-14. As with the test conducted on the initial cutting force, this median rank test shows that the data also tends to

distribute in such a way as to form a reasonably good straight line. From this plot it can also be concluded that the exponential constant values are normally distributed. It should be noted that, in both the case of the initial cutting force values and the exponential constant values, there exists several outliers. These outliers suggest the presents of small variations in the experimental data obtained and, although it does not change our conclusion that the data is normally distributed, may need to be addressed when gathering the data for model calibration and validation.

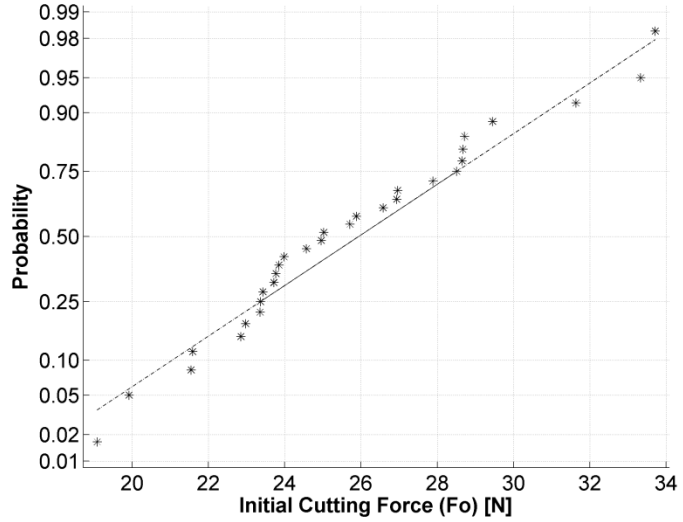

Figure 4-13: The results of a median rank normality test using initial cutting force data.

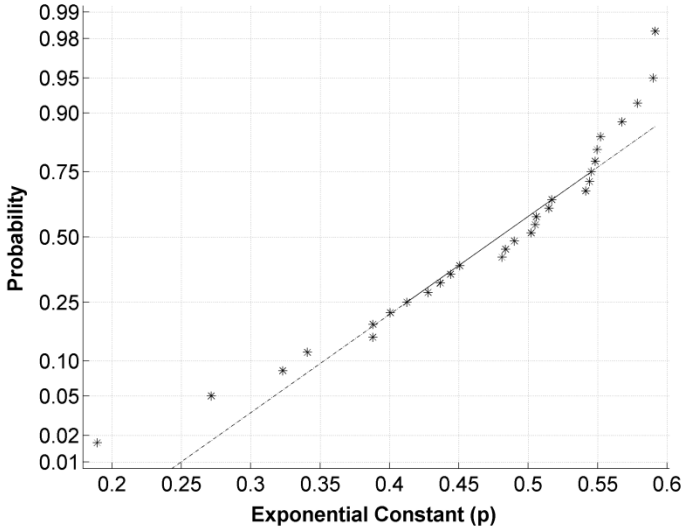

Figure 4-14: The results of a median rank normality test using the exponential constant data.

4.4.4 Chi Square Test

The Chi Square test is based on the plotting of the data in a histogram form. This places the data in discrete 'bins' each having its own frequency of occurrence. The function that best models these bins is called the Chi Square function. Once the binned data is normalized, the summation total for each bin is obtained and the total can be compared, over some predefined confidence limit, to the values found on a Chi Square table. Using a null hypothesis test, the goodness of fit of the data can then be determined.

As with the median rank test, the Chi Square test was performed on both the initial cutting force and the exponential constant to confirm normal distribution. The first step of a Chi Square test is to standardize the data using the data's mean and standard deviation. This process was performed on the same 30 trial data that was used for the median rank test. The results of this standardization are tabulated in Table B-2 of Appendix B. The standardized values for initial cutting force were then placed in discrete bins to determine the frequency of occurrence and to plot the histogram. The histogram for the initial cutting force is displayed in Figure 4-15. As it can be seen from Figure 4-15, this histogram suggests that the data is almost normally distributed as most of the data is clustered around the zero (± 0.5) value.

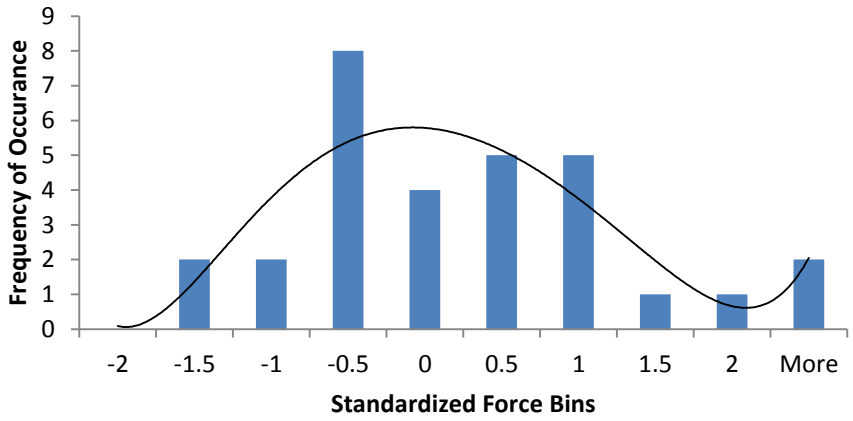

Figure 4-15: Resulting histogram based on initial cutting force data.

In addition to the histogram, a null hypothesis Chi Square test was performed using the same standardized data, seven degrees-of-freedom, *v*, and a 95% confidence limit. See Appendix A for calculation of degrees−of−freedom. The results of this test are displayed in Table 4-2. As if can be seen from Table 4-2, the sum of the Chi Squared values for each bin is approximately 8.33

which is less than the acceptable Chi Square value of 14.1 reported for seven degrees-of-freedom, *v*, and a 95% confidence limit. Thus, the null hypothesis that the data is normally distributed must be accepted and it can be concluded that, based on a 95% confidence limit, the data is normally distributed and is, thus, statistically significant [50].

Bins	Observed Counts	Normal Probability	Expected Counts	Observed - Expected	Chi Square Values
< -2.0	0	0.023	0.69	-0.69	0.6900
-2.0 to -1.5	2	0.044	1.32	0.68	0.3503
-1.5 to -1.0	2	0.092	2.76	-0.76	0.2093
-1.0 to -0.5	8	0.15	4.5	3.5	2.7222
-0.5 to 0	4	0.191	5.73	-1.73	0.5223
0 to 0.5	5	0.191	5.73	-0.73	0.0930
0.5 to 1.0	5	0.15	4.5	0.5	0.0556
1.0 to 1.5	1	0.092	2.76	-1.76	1.1223
1.5 to 2.0	1	0.044	1.32	-0.32	0.0776
> 2.0	2	0.023	0.69	1.31	2.4871
	Total = 30				Sum = 8.3297

< 4.1 with: *v*=(10-1-2)=7 @ 95% CL

Table 4-2: Chi Square test for normality using the initial cutting force data.

A similar procedure to confirm normality was followed for the exponential constant, *p*. As done for the initial cutting force, each of the experimentally acquired exponential constants were standardized and placed into discrete bins. These standardized values are tabulated in Table B-3 of Appendix B. A histogram was plotted and is displayed in Figure 4-16 below. Once again, from this figure, it can be seen that the data tends to cluster around the zero value suggesting that it is normally distributed.

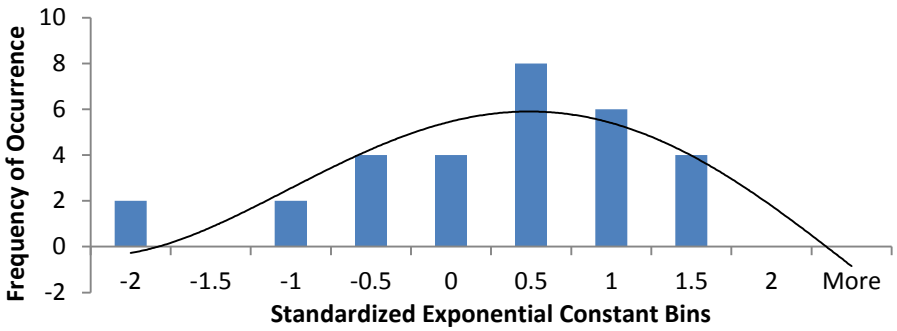

Figure 4-16: Resulting histogram based on exponential constant data.

A Chi Square test was also performed on the exponential constant using a null hypothesis test with seven degrees-of-freedom and a 95% confidence limit. The test was conducted in an identical fashion as was the test done with the initial cutting force. Namely, the sum of the Chi Square values for each bin was found and compared to the reported Chi Square value for a seven degree of freedom and 95% confidence limit test. The results of this comparison are displayed in Table 4-3.

Bins	Observed Counts	Normal Probability	Expected Counts	Observed - Expected	Chi Square Values
< -2.0	2	0.023	0.69	1.31	2.4871
-2.0 to -1.5	0	0.044	1.32	-1.32	1.3200
-1.5 to -1.0	2	0.092	2.76	-0.76	0.2093
-1.0 to -0.5	4	0.15	4.5	-0.5	0.0556
-0.5 to 0	4	0.191	5.73	-1.73	0.5223
0 to 0.5	8	0.191	5.73	2.27	0.8993
0.5 to 1.0	6	0.15	4.5	1.5	0.5000
1.0 to 1.5	4	0.092	2.76	1.24	0.5571
1.5 to 2.0	0	0.044	1.32	-1.32	1.3200
> 2.0	0	0.023	0.69	-0.69	0.6900
	Total = 30				Sum = 8.5606

< 14.1 with: v=(10-1-2)=7 @ 95% CL

Table 4-3: Chi Square test for normality using the exponential constant data.

As is depicted in Table 4-3, the sum of the Chi Squared values for each bin was found to be approximately 8.56 which is less than the reported Chi Square value of 14.1. From this, it can be concluded that the null hypothesis that the data is normally distributed must be accepted and, based on a 95% confidence limit, the data is normally distributed [50].

4.5 Data Processing

Inherent to any experimental data collection practice is the need to process the collected data in an attempt to remove any unwanted disturbances or unnecessary data. The experimental data collected for this thesis was no exception. The data was processed in three different ways. First the drilling force and torque signals were isolated to include only the cutting forces. Second the signals were normalized to eliminate the variation in initial cutting force. Finally, the remaining data signals were filtered to remove experimental noise. This section will investigate these three data processing techniques.

4.5.1 Data Isolation

The experimental signal data collected contained several portions of data that were unwanted. Figures 4-17a and 4-17b displays an example of the raw force and torque data collected experimentally. As it can be seen from Figure 4-17a, the time between 0 seconds and approximately 8.5 seconds is the time during which the drill is approaching the first layer of cortical bone. At approximately 8.5 seconds, the drill has reached and engages the bone as the force instantaneously spikes to the initial cutting force of approximately 35 N. Over the next few seconds the force appears to be slowly increasing as the drill flutes begin to clog with material and the frictional resistance to the cutting begins to increase. As the drill proceeds, this resistance begins to increase at a much more rapid rate until it finally peaks right before breaking through the first layer of cortical bone and extending into the cancellous bone. This results in the force returning to approximately zero. It was at this time that the drill was retracted and returned to its home position as is depicted from approximately 14.5 seconds until the data collection equipment is turned off at approximately 26 seconds.

There are three portions of this raw data that are undesired. The first is the portion from the time when the data collection begins to the moment just before the drill engages the bone. Using

the example shown in Figure 4-17, this would represent the time from 0 seconds to approximately 8.5 seconds.

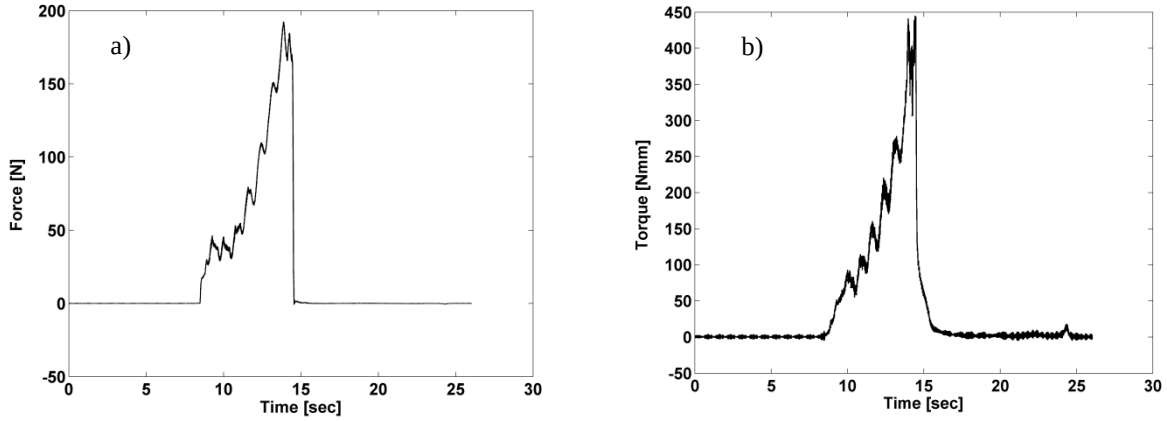

Figure 4-17: An example of the raw a) force and b) torque data obtained experimentally.

The second portion of data that is undesired is the rapid increase of the cutting force and torque observed as the drill first engages the bone and continues until the initial cutting force is achieved. This is shown as the approximate 0.5 second duration from 8.5 seconds to 9 seconds in Figure 4-17. This portion of the data is undesired since prediction models for the initial cutting force are prevalent in the literature and our model only attempted to predict the force and torque after the initial cutting force had been achieved. This portion can readily be predicted and programmed into a haptic device.

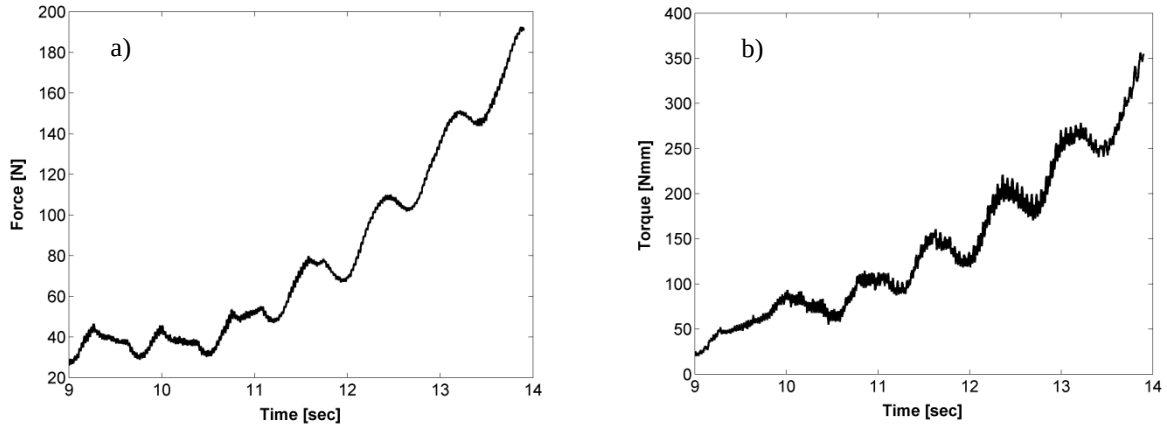

Figure 4-18: An example of a) force and b) torque data after signal isolation.

The final portion of the signal that is undesired is the section of data from when the drill breaks through the cortical bone until the data collect equipment is turned off. Figure 4-17

displays this portion of data from approximately 14.5 seconds to 26 seconds (to the end of the data signal). These three sections of data were removed manually leaving only the drill clogging signal of interest. The isolated data for the same example presented in Figure 4-17 is shown in Figure 4-18.

4.5.2 Data Normalization

Once the desired data for both force and torque was isolated, the independent and dependent variables needed to be altered to match the model. Specifically, the dependant variables (thrust force and torque) needed to be normalized to eliminate the variation in initial cutting force and the independent variable (time) needed to be converted to the dimensionless ratio of depth/diameter (z) to conform to the model presented in Chapter 3. To normalize the force data, each value of the signal was divided by the initial cutting force. To convert the time variable to the depth/diameter ratio, the time signal was multiplied by the feed rate to convert the time into depth and this result was divided by the diameter to yield the required depth/diameter ratio. The result of these alterations for the same example data used is depicted in Figure 4-19. It should be observed from this figure that the trends of the data remained unchanged as the independent and dependent variables were altered.

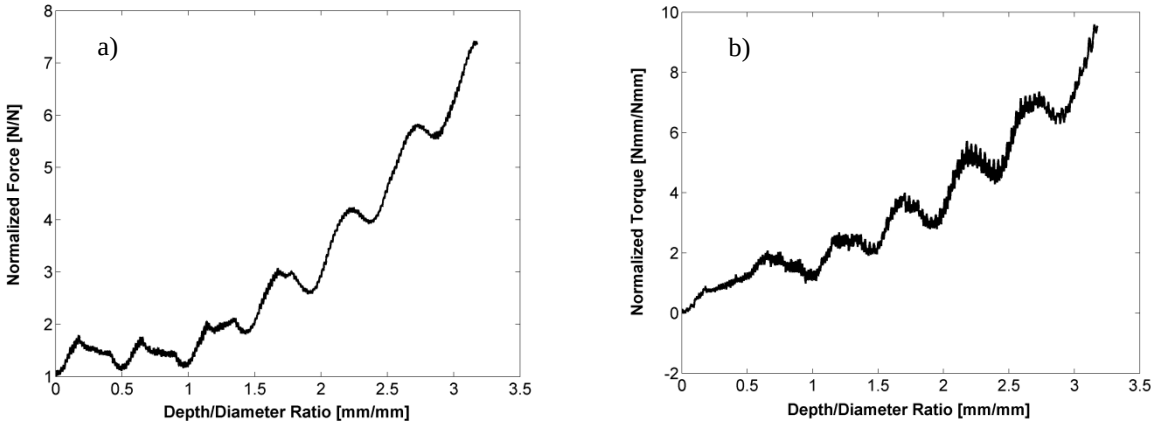

Figure 4-19: An example of a) force and b) torque data after normalizing the signals.

4.5.3 Data Filtering

After the collection of the data, it was observed that many of the data signals contained undesired frequency that could be considered as noise. Filtering was used to remove the undesired or disruptive portion of the signal data without affecting or altering, in any way, the

overall trend of the results. The fact that filtering does not disturb the trend of the data is very important since any alteration of data's trend could introduce bias into the experiment and could, ultimately, vary the results. It should also be noted that filtering signal data could affect the trend if a wrong filter is used or the correct filter is improperly tuned. Filter selection and tuning will be discussed at length later in this section.

Once the process of analysing the result of these particular experiments began, it was clear that the experimental results would require some form of filtering. This was evident simply by observing a large oscillation of the signal progress in time. Figure 4-19 showed an example of a raw force and torque data signals acquired experimentally. The aforementioned large oscillation is clear in this example and appeared to represent a low frequency noise. It was concluded that this oscillation was a result of the CNC machine not feeding continuously and actually feeding in a pulse type fashion. We attributed this to a slightly worn slider in the CNC machine causing the rail to bind on occasion and resulting in the feed pulsating. This also represents many practical bone drilling situations. The noise in the data rendered the trend of the data a little more difficult to determine, and increased the difficulty in identifying outliers from large groups of data. For these reasons, all of the experimental data were smoothed by a filter before analysis.

There are several different types of filters that are used to filter signal data. The most common types are: high-pass and low-pass filters. Since the desired portion of the signal was the very low frequency exponential trend of the data and the undesired portion of the signal was the higher frequency oscillation caused by the CNC machine, a low-pass filter was selected as the filter of choice for this application. Additionally, a low-pass filter would also remove any of the high frequency noise inherent to the data acquisition system.

The filter was created using Matlab's Simulink toolbox as depicted schematically in Figure 4-20. The independent and dependent variables were fed into the filter from the Matlab workspace as variables a (time), b (force), and c (torque). Tuning the low-pass filter required an examination of the data to determine the filtering parameters; namely: the sampling frequency (f_s), the pass frequency (f_{pass}), and the stop frequency (f_{stop}).

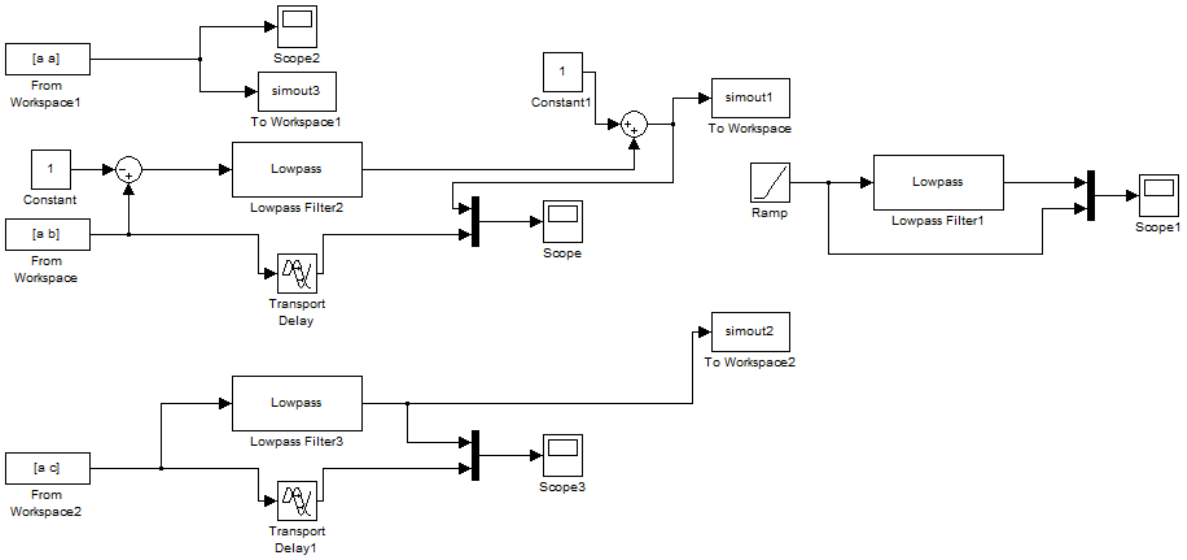

Figure 4-20: Simulink schematic of the low-pass band filter used to filter experiential signal data.

The filter parameters required to properly tune the low-pass filter were strictly dependant on the experimental conditions; specifically on the conditions of the experiment that are time dependant. This means that if any of the time dependant experimental parameters are changed, a new filter would need to be designed. Since one of the independent variables of this experiment was the feed rate of the drill, a time dependant parameter, a separate filter was designed for each feed rate. Furthermore, since the sampling frequency and pass frequency were approximately the same for all operating parameters, the values for f_s and f_{pass} remained constant. A summary of the low-pass filter parameter values are provided in Table 4-4.

Feed Rate [mm/sec]	Sampling Frequency [Hz]	Pass Frequency [Hz]	Stop Frequency [Hz]
1.0	500	0.05	2.2
1.5	500	0.05	2.0
1.75	500	0.05	1.9
2.0	500	0.05	1.8

Table 4-4: Summary of low-pass filter tuning parameters based on increasing feed rate.

Once the filter was properly tuned for each of the specified feed rates based on the values presented in Table 4-4, each individual data signal was passed through the filter and the newly filtered data was obtained. An example of this can be seen in Figure 4-21 as the filtered data for force and torque are overlaid the original signal (Figure 4-19). As it can be seen, the signal's trend is much clearer and smoother. This is further exemplified in Figure 4-22 where an entire

data set is depicted prior to and after filtering. From this figure, the reader can appreciate that the filtered data is significantly easier to read allowing for ease of data trend recognition and outlier identification.

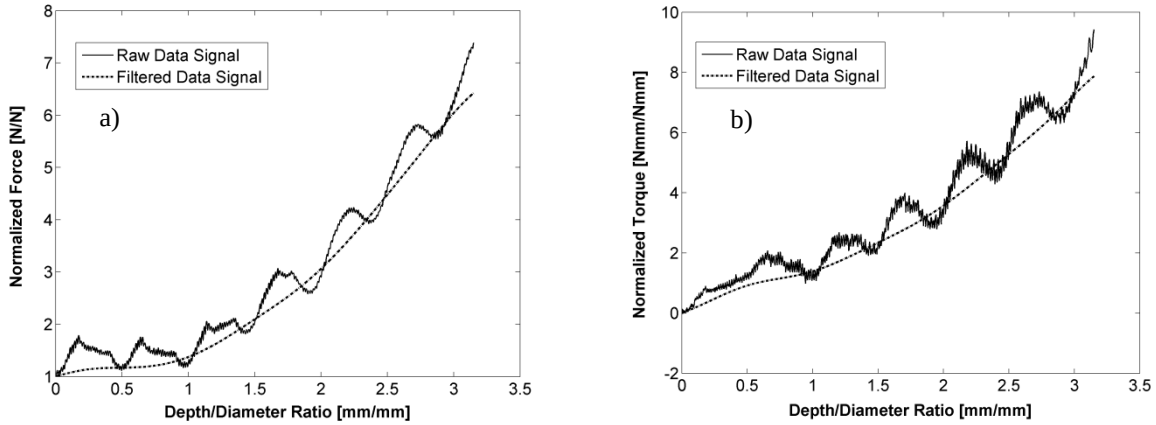

Figure 4-21: Example of raw experimental a) force and b) torque data signals overlaid by their corresponding filtered signals.

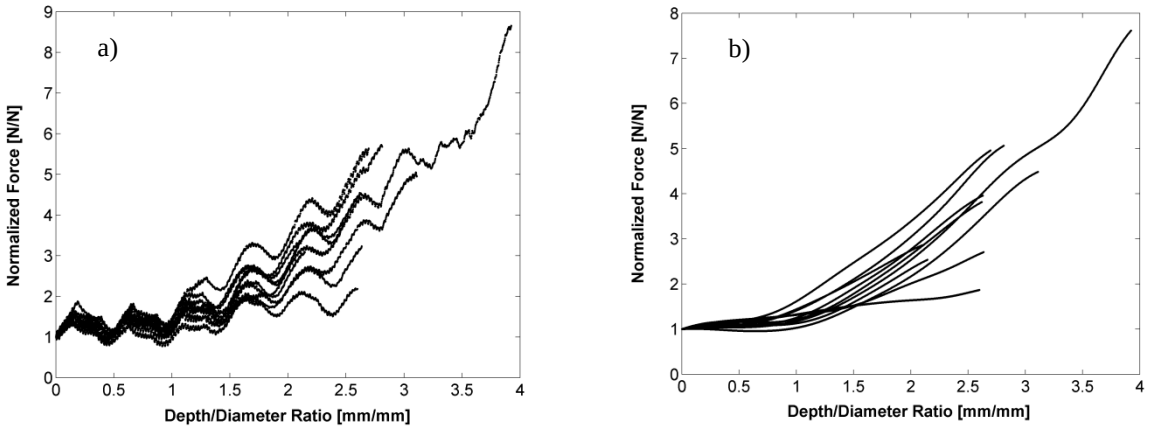

Figure 4-22: An example of a complete data set a) before filtering and b) after filtering.

5 Results and Discussion

The experimental data collected while drilling bovine bone was used to calibrate the empirical chip-evacuation thrust force and torque prediction models presented previously. The sensitivity of the empirical models to their respective calibration parameters, μ_f and μ_w was also investigated. In Section 5.4, the experimental data was used to train the artificial neural network that was introduced in Chapter 3. Once the ANN was properly trained, additional experimental results were used to validate the accuracy of the network. Sections 5.6 and 5.7 of this chapter will repeat the empirical model calibration and validation, respectively, with experimental data collected while drilling human bone. The section to follow will compare the results of all of the presented models and discuss the significance of the findings. Section 5.9 will incorporate the established force and torque models into the finite element analysis simulation that was introduced in Chapter 3.

5.1 Empirical Chip-Evacuation Model Calibration

The thrust force and torque prediction models were calibrated using a 2 factorial design of experiments with an additional combination of operating parameters used to increase the generalization of the models. Each of these combinations was run with 10 replicates resulting in 50 sets of experimental data in total. For all experiments, only the first layer of cortical bone was drilled (unicortical) and only force and torque data about the z-axis was collected as this was the only data required for calibration. The 10 replicas for each of the 5 sets of operating parameters were collected and processed (isolated, normalized, and filtered as outlined in Chapter 4). An example of a complete data set overlaying itself is presented in Figure 5-1 using a feed rate of 2.0mm/sec and a spindle speed of 1500RPM.

It is clear from Figure 5-1 that there exists some variation in the results. This is a consequence of several factors. The first and most significant of these factors is the nature of the bone itself. Bone is an anisotropic material which is due to the organization of bone cells which tend to follow lines of applied stress [51]. This could result in particular parts of the bone being more or less vulnerable to the effects of clogging. The second of these factors is cortex thickness. The cross-sectional geometry of a bovine femur bone is not consistent along the entire length of the

bone. Therefore, the thickness of the cortex varies at different locations on the bone. This is evident from Figure 5-1 as some of the force and torque data ended after a depth of approximately 5.5mm while others went to depths of approximately 11mm. Since clogging is a function of hole depth, the experiments conducted on thinner areas of the bone lacked the increased force and torque due to the effect of clogging.

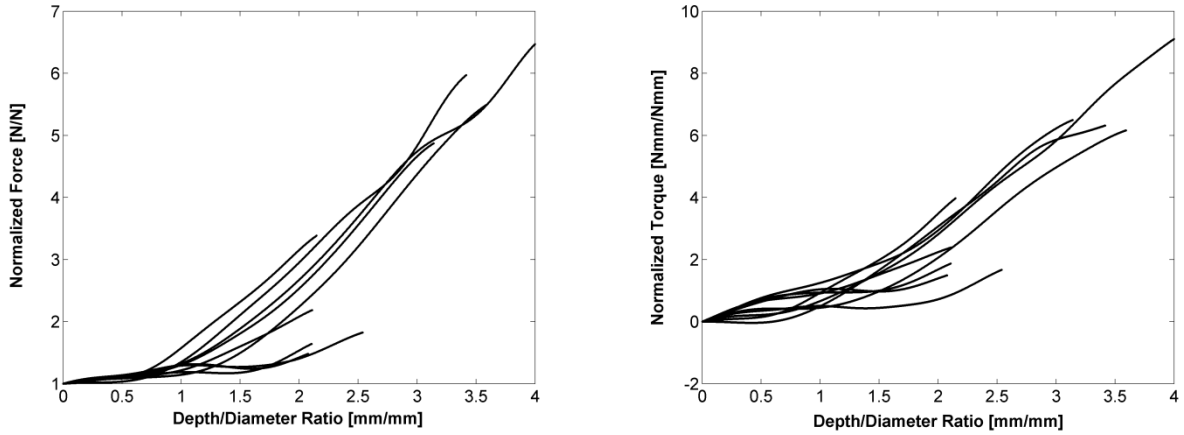

Figure 5-1: A complete set of experimental data collected using a feed rate of 2.0mm/sec and a spindle speed of 1500RPM.

Experimental data that deviates significantly from the other members of the sample in which it occurs are called *outliers*. The inclusion of outliers can have very negative effects on regression analysis and other trending techniques as they tend to influence the trend toward an incorrect solution [50]. Thus, all outliers must be removed before further analysis can commence.

Outlier identification is not an exact science [50]. As it pertains to data collected for the drilling of bone, this process involved simply selecting the data sets that appeared to trend differently than the others from the same sample. Once the outliers were identified, they were removed from that particular sample data set. An example of this is depicted in Figure 5-2 for the same sample data set as was presented in Figure 5-1. From this figure it is observed that the sample data set has much less variation and is now suitable for further analysis. The sets of data obtained using the other 4 pairs of operating parameters can be found in Appendix C, Figures C-1 to C-5.

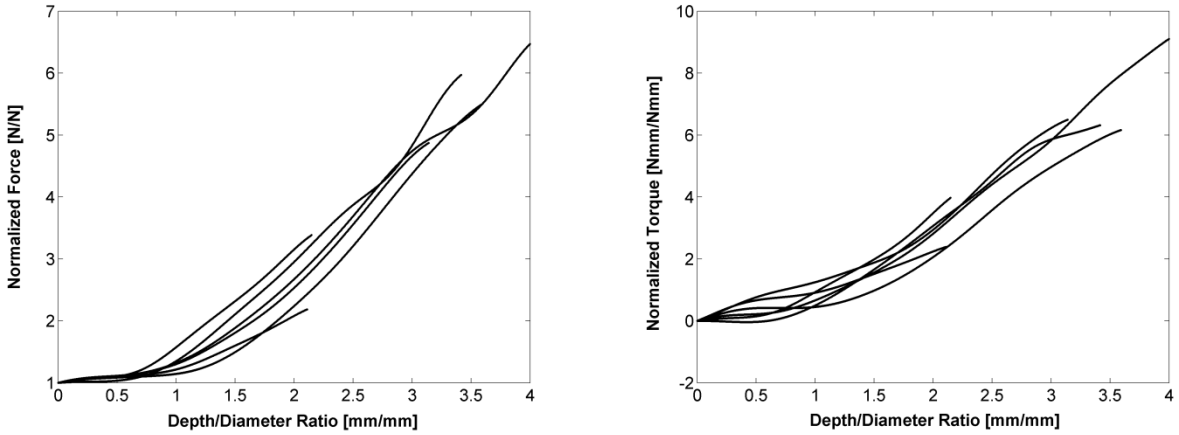

Figure 5-2: A sample data set with outliers removed collected using a feed rate of 2.0mm/sec and a spindle speed of 1500RPM.

Referring to the empirical model calibration procedure outlined in Chapter 4, the next step was to perform a nonlinear least-squares optimization on each data set. This involved the comparison of values obtained experimentally with the empirical form of the force and torque prediction models using Eq. 4.4. This allows for the extraction of the optimized coefficients of friction, μ_f and μ_w. These optimized coefficients of friction for all 5 data sets are presented in Table 5-1.

Feed Rate (*f*) [mm/sec]	**Spindle Speed (*N*) [RPM]**	μ_f	μ_w
1.0	1000	0.1989	0.5406
1.5	1100	0.2236	0.6217
1.5	1250	0.2135	0.5910
1.75	1500	0.2071	0.5895
2.0	1500	0.2131	0.5701

Table 5-1: The results of nonlinear least-squares optimization used to determine the coefficients of friction for all calibration operating parameters.

As the spindle speed increased while the feed rate remained constant, both coefficients of friction decreased which will result in a lower value for thrust force and torque. This is an expected result as it was established in Chapter 2 that thrust force and torque are inversely proportional to spindle speed. Additionally, as feed rate increases while the spindle speed remains constant, the coefficient of friction between the drill flute and the bone chip, μ_f, increases while the coefficient of friction between the bone chip and the wall, μ_w, decreases. This result also agrees with the theory as the friction between the bone chip and the drill flute depends on the transverse velocity (feed rate) while the coefficient between the bone chip and the wall of

the hole is dependent more on the tangential velocity (spindle speed). It is difficult to determine the effect of these parameters when both the feed rate and spindle speed are changing simultaneously as each would independently impact the results. Although, by inspection, it would appear that these values also follow a similar trend.

With the determination of the optimized coefficients of friction for all data sets, the next step was to determine the coefficients of the power law. This was done by employing Eqs. 4.6 and 4.7 and solving the system of equations yielding the power law constants. These constants are presented in Table 5-2.

i	0	1	2	3
a_i (μ_f)	-0.2146	2.9851	-0.2027	-0.3783
b_i (μ_w)	-2.3518	7.3518	0.2514	-1.0177

Table 5-2: Coefficients of the power law model.

The coefficients of the power law can be substituted into Eq. 4.5 resulting in the following:

$$\ln \mu_f = -0.2146 + 2.9851 \ln(f) - 0.2027 \ln(N) - 0.3783 \ln(f) \ln(N), \quad (5.1)$$

$$\ln \mu_w = -2.3518 + 7.3518 \ln(f) + 0.2514 \ln(N) - 1.0177 \ln(f) \ln(N). \quad (5.2)$$

The above two equation can be used to determine the coefficients friction, μ_f and μ_w, for any feed rate, f, and spindle speed, N. Once the coefficients of friction have been calculated, they may be substituted back into Eqs. 3.16 and 3.19 to evaluate the chip-evacuation force and torque at any depth during the drilling of bovine bone, respectively.

5.2 Empirical Chip-Evacuation Model Validation

To properly validate any empirical prediction model, the model must demonstration that it can generate accurate results based on parameters outside those of which it was established. This can be demonstrated by acquiring additional experimental results using operating parameters different, but within the same approximate range as those which the model was established.

Two additional sets of operating parameters were used for validation of the model predictions. Each of the new set of operating parameter was run twice; the operating parameters that were used are found in Table 5-7. The spindle speeds and feed rates in Table 5-7 are in the same range

as those on which the models were calibrated and are also operating parameters common with typical orthopaedic practices [9, 13 ,18].

Feed Rate (*f*) [mm/sec]	**Spindle Speed (*N*) [RPM]**
1.75	1250
2.0	1000

Table 5-3: The operating parameters used for validation experiments.

Four validation experiments were run (two for each of the new operating parameters) and the obtained data was isolated, normalized, and filtered as was done previously. The results of these experiments are presented in the following four figures. Figures 5-3 and 5-4 display the thrust force and torque using a feed rate of 1.75mm/sec and a spindle speed of 1250RPM for each of the two trials. Figures 5-5 and 5-6 display the thrust force and torque using a feed rate of 2.0mm/sec and a spindle speed of 1000RPM for each of the two trials. Also plotted in each figure are the respective empirical model's prediction of the chip-evacuation force and torque based on the operating parameters.

As it can be seen from Figures 5-3 to 5-6, the empirical chip-evacuation force and torque prediction models do well in estimating the force and torque experienced while drilling bovine bone. The precision of these models can be quantified by calculating the coefficient of determination, R^2, for each of the compared results. The coefficient of determination is a statistical measurement used to quantify how well an empirical model is likely to predict future outcomes [50]. The resulting measure ranges from 0 to 1 with 1 representing a perfect fit or prediction and 0 signifying inadequate fit or prediction. As it related to this discussion, the coefficient of determination will provide a basis of comparison on which the accuracy of empirical models can be related to the obtained validation data. The coefficients of determination were calculated using the standard form that can be found in most statistical textbooks [50]:

$$R^2 = 1 - \frac{SS_{err}}{SS_{tot}}, \tag{5.3}$$

where SS_{err} is the residual sum of squares, and SS_{tot} is the total sum of squares. This is represented mathematically as:

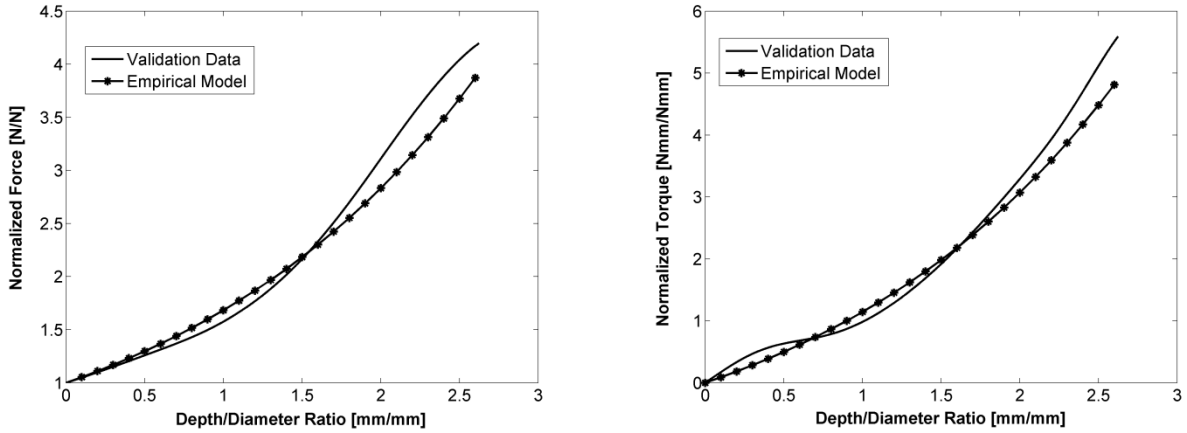

Figure 5-3: Trial one of the comparison of experimental validation data versus predicted empirical model for force and torque using a feed rate of 1.75mm/sec and spindle speed of 1250RPM.

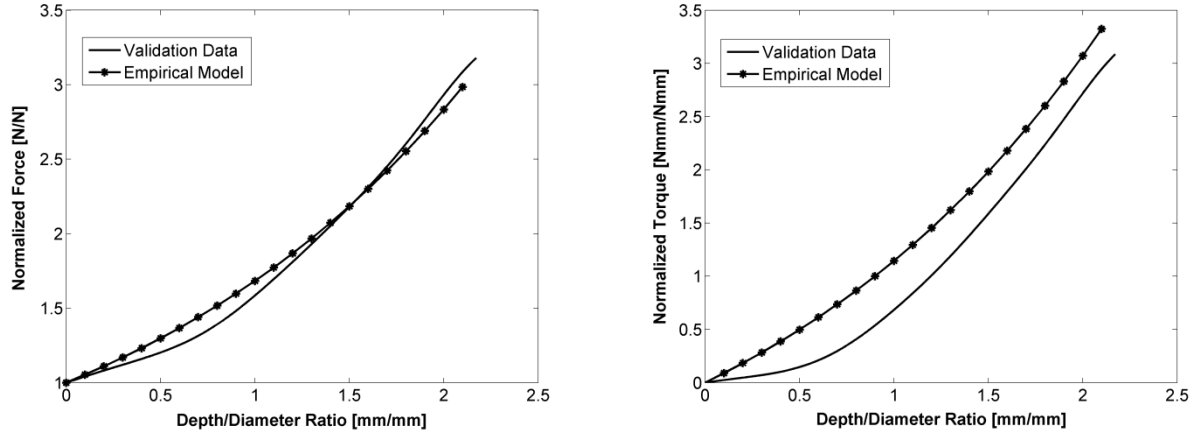

Figure 5-4: Trial two of the comparison of experimental validation data versus predicted empirical model for force and torque using a feed rate of 1.75mm/sec and spindle speed of 1250RPM.

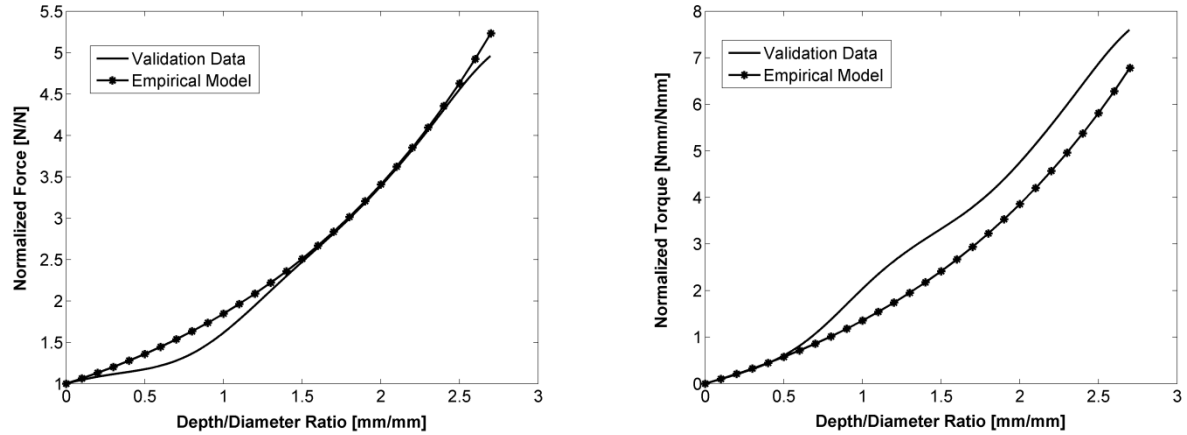

Figure 5-5: Trial one of the comparison of experimental validation data versus predicted empirical model for force and torque using a feed rate of 2.0mm/sec and spindle speed of 1000RPM.

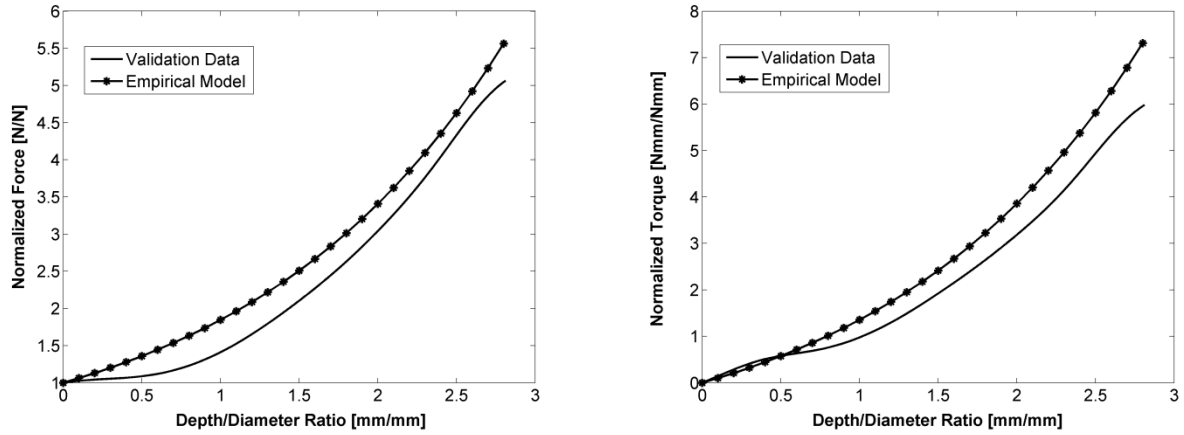

Figure 5-6: Trial two of the comparison of experimental validation data versus predicted empirical model for force and torque using a feed rate of 2.0mm/sec and spindle speed of 1000RPM.

$$SS_{err} = \sum_i \left(y_i - \hat{y}_i \right)^2, \tag{5.4}$$

$$SS_{tot} = \sum_i \left(\hat{y}_i - \bar{y} \right)^2, \tag{5.5}$$

where,

$$\bar{y} = \frac{1}{n} \sum_i^n y_i \, . \tag{5.6}$$

Here y_i is the ith observed data set value, $\hat{y}_i$ is the associated ith predicted value, $\bar{y}$ is the arithmetic mean of the observed data set, and n is the total number of samples in that particular data set. The R^2 values for the force and torque comparison of all four validation trials is presented in Table 5-4.

Feed Rate (*f*) [mm/sec]	Spindle Speed (*N*) [RPM]	Trial #	R^2 for Force Model	R^2 for Torque Model
1.75	1250	1	0.9455	0.9658
		2	0.9836	0.8627
2.0	1000	1	0.9627	0.9347
		2	0.9265	0.9205

Table 5-4: The coefficients of determination, R^2, for the force and torque models for each of the four validation experiments.

It can be concluded that, based on the high R-squared values presented in Table 5-4, the empirical chip-evacuation prediction models presented are acceptable for estimating the increased thrust force and torque experience while drilling bovine bone. The thrust force model

appears to be slightly more accurate with an average R-squared value of 0.9546 while the torque model reported an average R-squared value of 0.9209. In either case, both showed highly acceptable results throughout the validation process.

5.3 Empirical Chip-Evacuation Model Sensitivity Analysis

A sensitivity analysis provides a clear picture of the relationship between a function's input variable and the output result [52]. An analysis of this nature is specifically interesting to this study since the output values of force and torque are dependent on both of the input values of μ_f and μ_w. The degree to which each model is sensitive to change in these coefficients of friction will be investigated in this section.

A sensitivity analysis was conducted to determine the influence of μ_f and μ_w on the presented force and torque predictions. The sensitivity of the models to the frictional coefficients was determined using the following definition [52]:

$$S_{\mu} = \frac{\mu}{\psi}\frac{\delta\psi}{\delta\mu}, \tag{5.7}$$

where $\mu = \mu_f, \mu_w$ and ψ represents the force and torque functions. The partial derivative represents the partial derivative of the force and torque models with respect to the coefficients of friction, μ_f and μ_w, respectively. The numeric values for μ and ψ were acquired experimentally. The results of this analysis are presented in Table 5-9.

	Force Model	**Torque Model**
Sensitivity ($S_{\mu f}$)	1.0700	0.6286
Sensitivity ($S_{\mu w}$)	0.1874	1.1101

Table 5-5: Force and torque prediction model sensitivity to the coefficients of friction μ_f and μ_w.

The sensitivity values presented in Table 5-5 represent what can be viewed as a ratio of dependence. That is, if a sensitivity of 0.5 were reported, the output value would have a ratio of 1:2 based on the input value tested. The results indicate that μ_f has a strong dominance on the thrust force model as the resulting sensitivity is relatively high. The sensitivity value of 1.07 reported in Table 5-5 suggests that an approximate 1:1 ratio exists between the input variable μ_f and the output result, F. In other words, if the coefficient of friction, μ_f, were to be doubled, the resulting output force would also be doubled. This is caused by bone chip-buildup in the drill's

flute which hinders material evacuation in the opposing direction of the thrust force and ultimately results in the force increasing. The input variable μ_w appears to have relatively little influence on the force prediction model. This is a result of the force caused by μ_w acting perpendicular to the thrust force and adding only marginal effect to the overall force.

A similar relationship can be observed between the input variables μ_f, μ_w and the torque prediction model. From Table 5-5, the torque prediction model appears to have a relatively high dependence on the coefficient of friction μ_w and a relatively lower dependence on the coefficient of friction μ_f. This can be explained by observing that the effect of μ_w occurs at the radius of the drill bit where an increasing resistance at the contact between material buildup in the flute and the wall of the hole is in the opposing direction of the rotation of the drill bit. This results in an increase in drilling torque. Furthermore, as was discussed, the effect of μ_f is acting perpendicular to the drilling surface and thus has reduced effect on the drilling torque.

5.4 Artificial Neural Network Training

As was first introduced in Chapter 3, an artificial neural network model was created as an alternative to the empirical model. This provided a complimentary approach and basis for comparison when analysing the results of the force and torque prediction models developed previously. Additionally, implementation of an accurate ANN model into clinical practice could provide an algorithm with faster computation time than that of the empirical formulation.

Initially, the network was constructed using all the experimental data. This was approximately 70 sets of experimental results containing roughly 52000 samples. This resulted in the ANN being unable to predict the output of any input outside of the values on which it was developed, a problem referred to as overtraining. Several trial and error attempts were made to find the optimal training data set. A total of 500 samples were used for the network input and target data.

The ANN was trained using the results of five experiments, each being run under different operating parameters. Additionally, each experiment was run only once. Table 5-6 provides a list of these parameters. The parameters used to train the neural network are slightly different than the ones used to calibrate the empirical model. This was simply a result of random trial and error.

Three parameters were used as input: feed rate, spindle speed, and depth to diameter ratio. The target values were chosen as the force and torque. Thus, the input was a 500x3 column matrix and the target was a 500x2 column matrix. The network was trained using 70% of the samples for training (350 samples), 15% of the samples for validation (75 samples), and 15% of the samples for testing (75 samples). The default hidden layer transfer function (sigmoid function) and the output layer transfer function (linear function) were left unchanged. Similarly, the default training algorithm (Levenberg-Marquardt backpropagation algorithm) remained unaffected. A default 10 neuron network was first used. A basic schematic of the network showing the 3 inputs, 10 neuron hidden layer, output layer, and 2 outputs can be seen in Figure 5-7.

Experiment #	Feed Rate (*f*) [mm/sec]	Spindle Speed (*N*) [RPM]
1	1.0	1000
2	1.5	1100
3	1.5	1250
4	1.75	1500
5	2.0	1000

Table 5-6: The experiment operating parameters used to train the ANN.

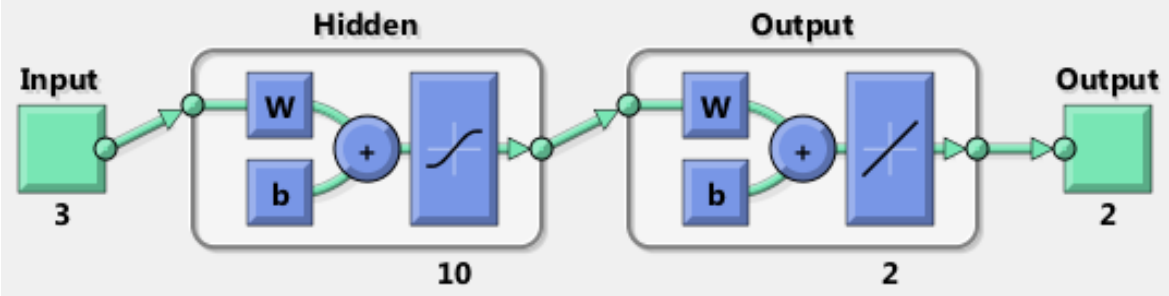

Figure 5-7: Schematic of the initial design of the neural network.

The above network was trained using the input and target data previously specified. The resulting network's performance produced small mean square error (MSE) and acceptable regression R-value for each training, validation, and testing. These results can be seen in Figures 5-8 and 5-9, respectively. As can be seen from Figure 5-8, the mean square error for training,

validation, and testing all rapidly decline before setting on acceptable MSE of approximately 0.0001. This indicates that the network was properly trained and will produce accurate results.

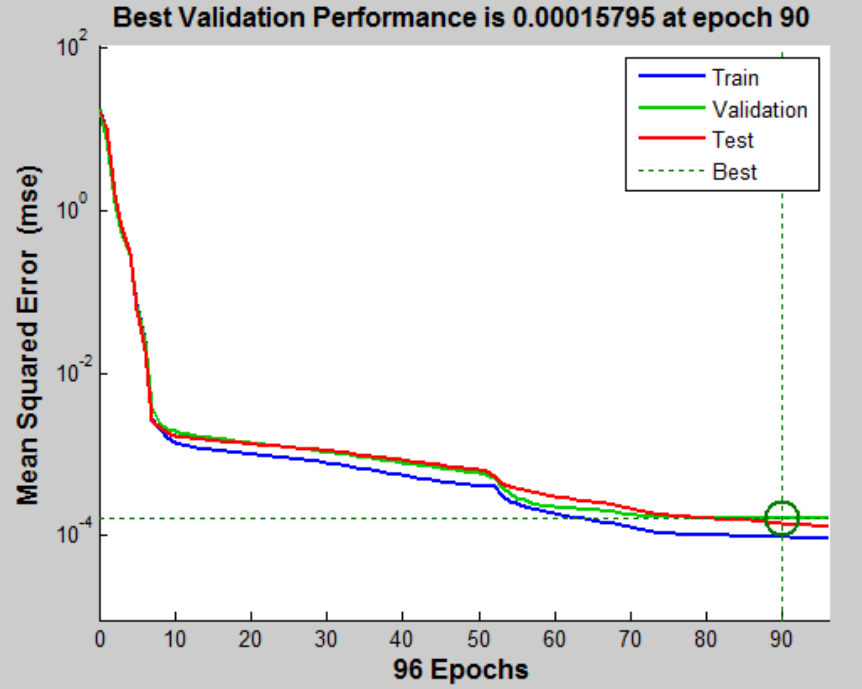

Figure 5-8: Plot of mean square error versus time for neural network training, validation, and testing.

Depicted in Figure 5-9 are the linear regression results for network training, validation, testing, and a plot providing the results of all three. As can be seen from this figure, all four plots display nearly perfect regression with R-values approximately equal to 1. Once again, this provides a measure of the network's training and accuracy indicating that the network has been appropriately trained. The next step was to test the network to determine the number of neurons required to provide the optimal solution.

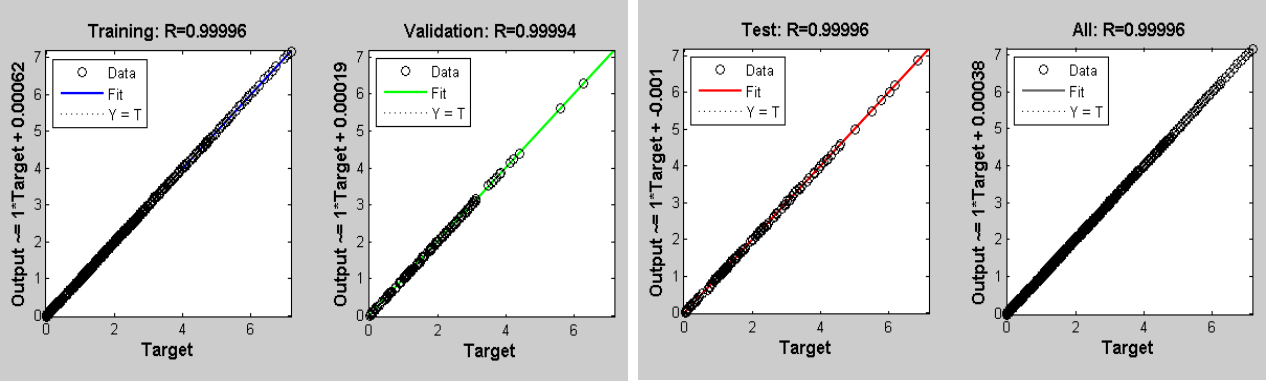

Figure 5-9: Plots of the linear regression results for network training, validation, testing, and the total.

5.4.1 Network Neuron Sensitivity Analysis

Analogous to the mesh sensitivity analysis conducted in Chapter 3, a network neuron sensitivity analysis is a process to determine how sensitive a particular network is to the number of hidden layer neurons it has. The number of neurons used in the hidden layer of a neural network is primarily based on the sample data used for training. An example of multi-neuron hidden layer is illustrated in Figure 5-10 where ***h*** is the input vector, ***W*** is the weight matrix, and ***b*** is the bias vector. In general, increasing the number of neurons in the hidden layer increases the flexibility and processing power of the system. In turn, this also increases the complexity of the network and can result in large processing times for network training and simulation. Additionally, having too many neurons in the hidden layer of the network is similar to having a system of equations with more equations than unknowns. As it is with linear algebra, this situation introduces redundancy to the system and reduces its ability to generalize. Alternatively, the use of too few neurons in the network's hidden layer can result in insufficient network training and improper fitting of the data. Thus, it is important to determine the optimal number of hidden layer neurons that will be used by the network. This process of finding the optimal number of neurons is called a network neuron sensitivity analysis.

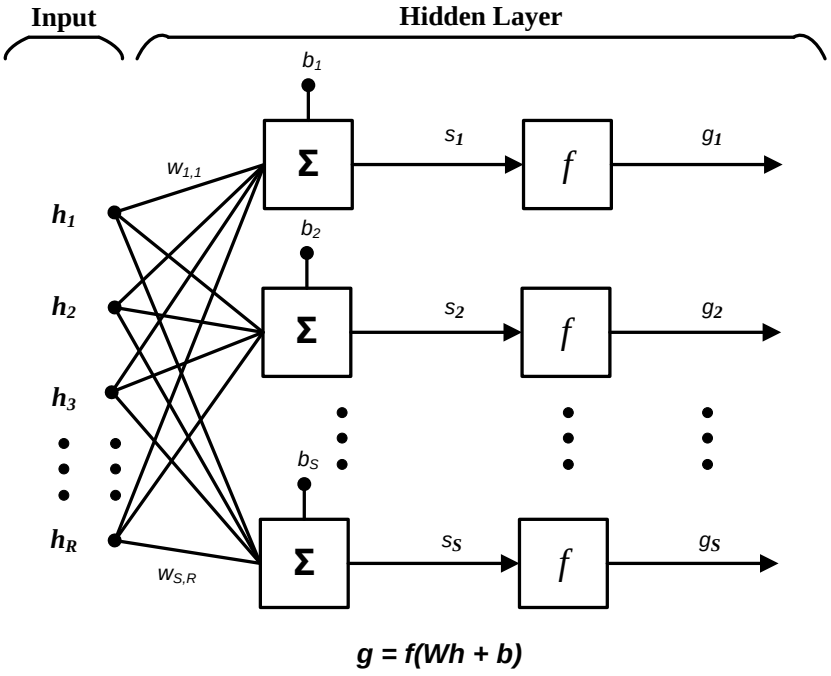

Figure 5-10: A schematic of a multi-neuron hidden layer artificial neural network.

The first step in this analysis was to select the range of hidden layer neurons to use to determine the sensitivity of the network. A simple one neuron hidden layer was chosen as the low end of the range.

To compare the difference between the varying neuron networks, each network was build and a validation simulation was performed. After each network was created, the mean squared error for the training of that network was recorded. The training error was shown to decrease as the number of neurons increased. To validate the network, two different sets of experimental data that were not used for the network training were used as validation inputs. The operating parameters that were used to generate these inputs appear in Table 5-7.

Validation #	Feed Rate [mm/sec]	Spindle Speed [RPM]
1	1.75	1250
2	2.0	1500

Table 5-7: Operating parameters used for network sensitivity and validation.

A network simulation was run using the operating parameters above and the depth to diameter ratio, *z*, as inputs to produce the outputs: force and torque. The network outputs were then evaluated by calculating the mean square error of the output compared to the experimental data collected using the same input parameters. More specifically, the output data from the network was plotted next to the experimental data and the mean-squared error was calculated to determine the difference between these two signals. This value was compared to the training error that was recorded after that specific network had been created. This provided a basis for comparing the sensitivity of the networks as the neurons increased. In theory, the ideal network is established when the values for the training error and validation error are at their lowest.

The above procedure was repeated for networks ranging from 1 neuron to 10 neurons. Some examples of the network output compared to the experimental results can be seen in Figure 5-11. Figures 5-11a and 5-11c depict examples of a single neuron networks which show good validation results and, by contrast, Figures 5-11b and 5-11d show two examples of a 10 neuron network which validated poorly.

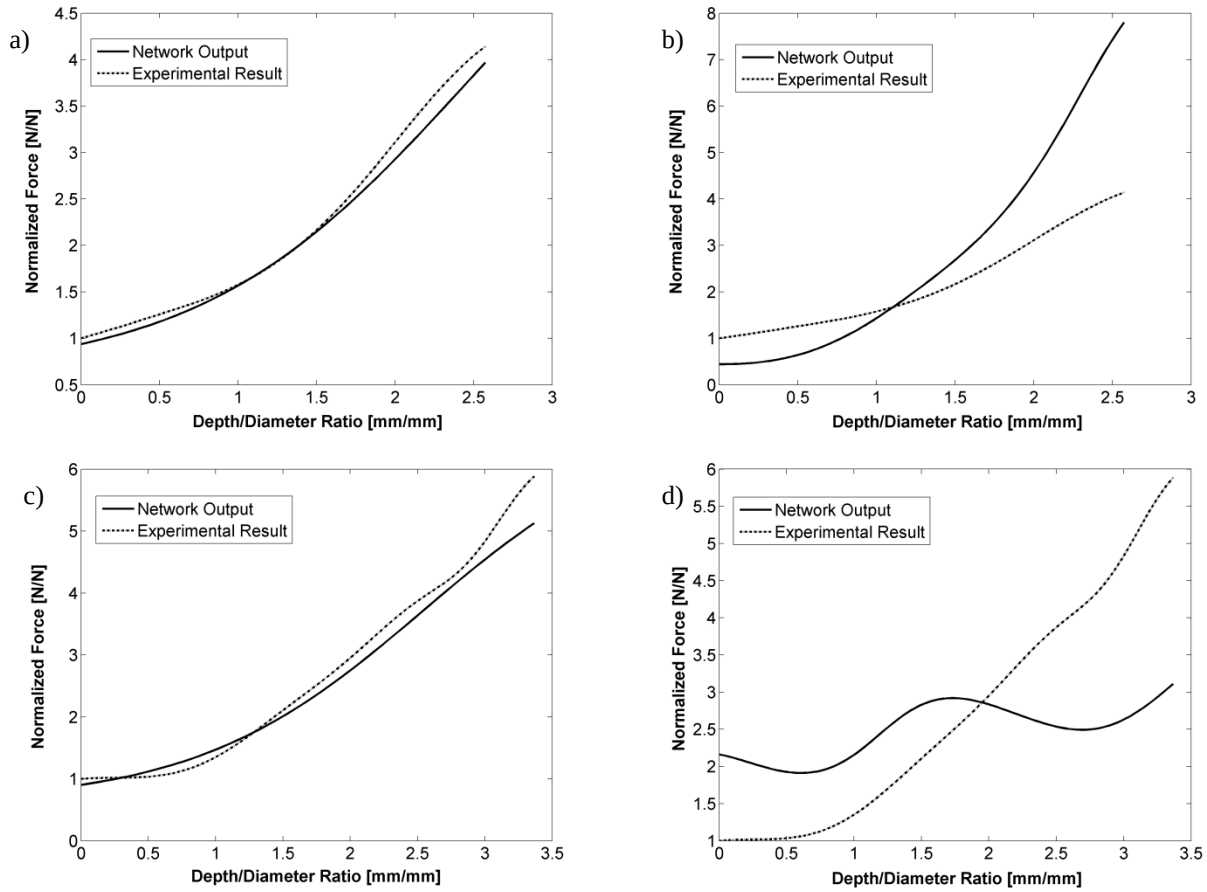

Figure 5-11: Plots of neuron sensitivity validation displaying the results of a) a single neuron network using validation parameters 1, b) a ten neuron network using validation parameters 1, c) a single neuron network using validation parameters 2, and d) a ten neuron network using validation parameters 2.

The training MSE and validation MSE were collected and compared using networks with 1 to 10 neurons. Recall that the validation was repeated using two different operating parameters to confirm the most accurate result. The training and validation errors were plotted together for both validation parameters to visually confirm the deviation. These plots and their corresponding table of values are depicted in Figure 5-12 for validation 1 and in Figure 5-13 for validation 2. These figures show that, as was expected, the training error is decreasing as the amount of neurons increase. Furthermore, the plots display the validation error deviating from the training error as the neurons are increased. The point at which this deviation occurs is the point of interest as training error and validation error are both at a low value. As it can be seen from the figures, this point of interest occurs at approximately two neurons. It was concluded that a two neuron network would be most optimal since it provided the lowest validation error whilst maintaining a low training error for both sets of validation parameters.

# of Neurons	Training Error	Validation Error
1	0.0348261	0.0152
2	0.0253324	0.0084
3	0.0131331	0.0718
4	0.00882103	0.443
5	0.00525807	0.0242
6	0.00151365	1.1693
7	0.00125416	0.4418
8	0.00037107	0.4885
9	0.00037653	0.3438
10	0.00036356	1.18746

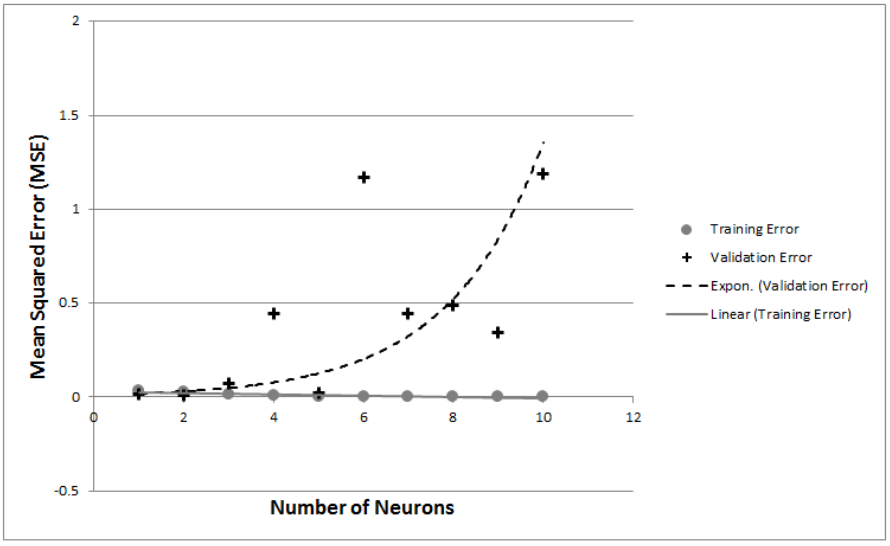

Figure 5-12: Plot depicting validation MSE versus number of hidden layer neurons using validation 1 parameters.

# of Neurons	Training Error	Validation Error
1	0.0348261	0.0592
2	0.0253324	0.0483
3	0.0131331	0.667
4	0.00882103	1.638
5	0.00525807	801.1055
6	0.00151365	1.2782
7	0.00125416	0.1158
8	0.00037107	1.6869
9	0.00037653	2.5124
10	0.00036356	7.0127

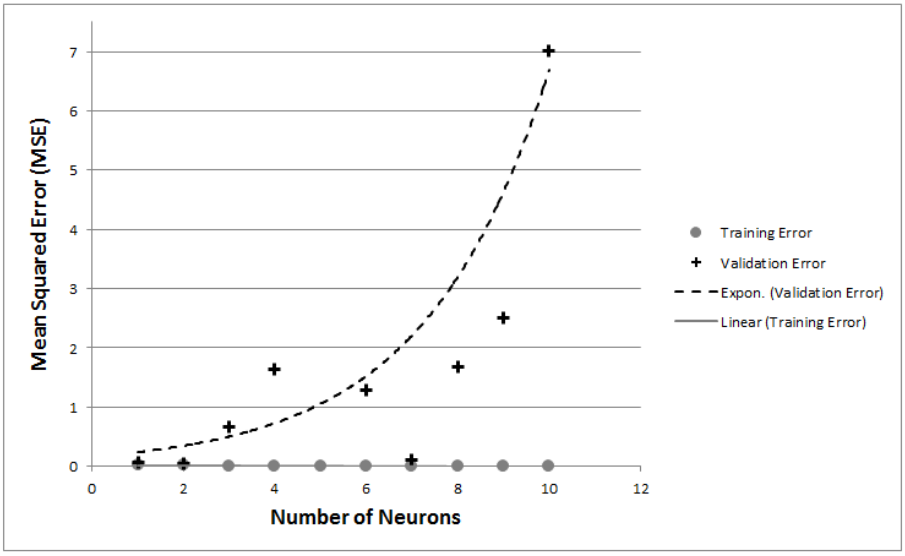

Figure 5-13: Plot depicting validation MSE versus number of hidden layer neurons using validation 2 parameters.

5.5 Artificial Neural Network Validation

With the ANN properly trained using a two-neuron hidden layer, the network's accuracy at predicting the chip-evacuation thrust force and torque was evaluated. The validation procedure was similar to the methodology followed for validating the empirical formulation. The feed rates and spindle speeds used to obtain this data were presented in Table 5-7. Two experimental trials

were run for each of the two sets of operating parameters. The newly acquired data was processed and plotted against the predicted chip-evacuation force and torque output from the network. The results of this validation are presented in Figures 5-14 and 5-15 for the data gathered using validation 1 parameters and in Figures 5-16 and 5-17 for the data gathered using validation 2 parameters.

As can be seen in the Figures 5-14 to 5-17, the two-neuron artificial neural network predicts the chip-evacuation thrust force and torque for the drilling of bovine bone well. To quantify this precision, the coefficient of determination was calculated for both trials using each of the two validation parameters. These R-squared values appear in Table 5-8.

Feed Rate (*f*) [mm/sec]	**Spindle Speed (*N*) [RPM]**	**Trial #**	**R^2 for Force Output**	**R^2 for Torque Output**
1.75	1250	1	0.9900	0.9579
		2	0.9315	0.9925
2.0	1500	1	0.9717	0.9376
		2	0.9834	0.9543

Table 5-8: The coefficients of determination, R2, for the force and torque network outputs for each of the four validation experiments.

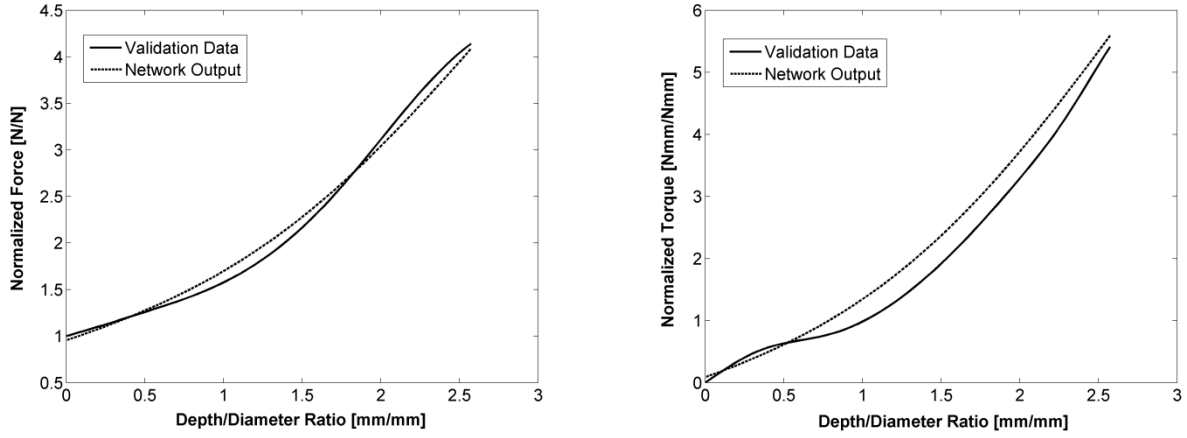

Figure 5-14: Trial one of the comparison of experimental validation data versus the predicted artificial neural network output for force and torque using a feed rate of 1.75mm/sec and spindle speed of 1250RPM.

Based on the relatively high R-squared values presented in Table 5-8, it can be concluded that the output obtained for the two-neuron artificial neural network is acceptable for estimating the increased thrust force and torque experience while drilling bovine bone. As was the case with the empirical formulation, the network's prediction of thrust force appears to be slightly more accurate with an average R-squared value of 0.9692 while the network's prediction of torque

reported an average R-squared value of 0.9606. In either case, both showed highly acceptable results throughout the validation process.

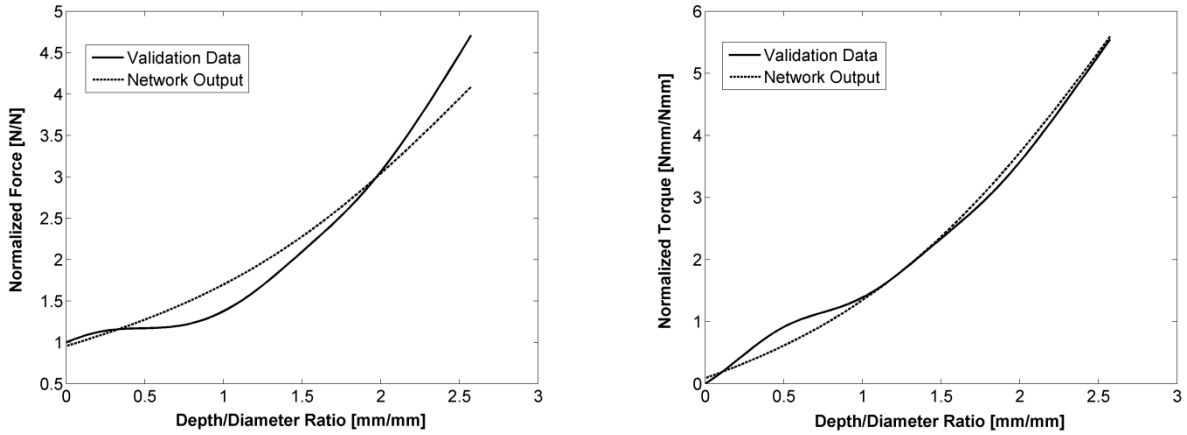

Figure 5-15: Trial two of the comparison of experimental validation data versus the predicted artificial neural network output for force and torque using a feed rate of 1.75mm/sec and spindle speed of 1250RPM.

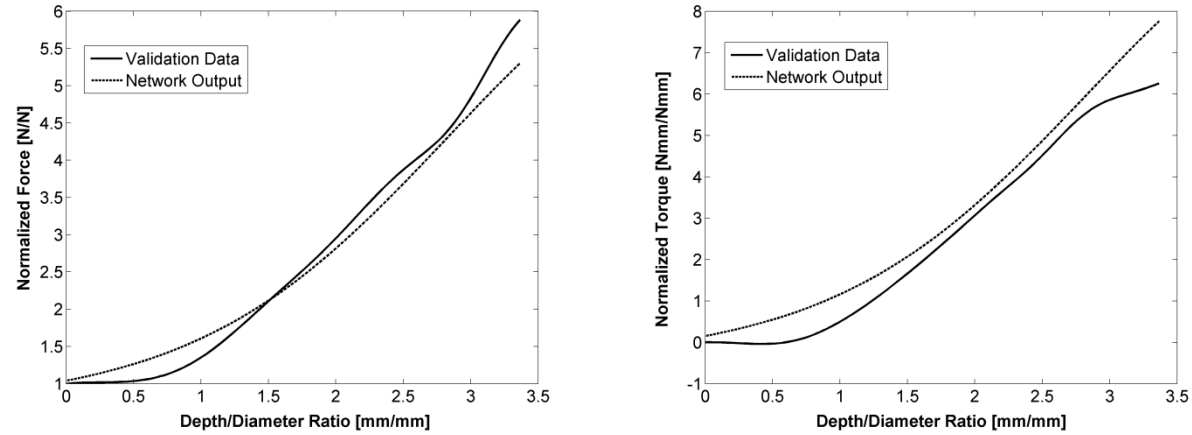

Figure 5-16: Trial one of the comparison of experimental validation data versus the predicted artificial neural network output for force and torque using a feed rate of 2.0mm/sec and spindle speed of 1500RPM.

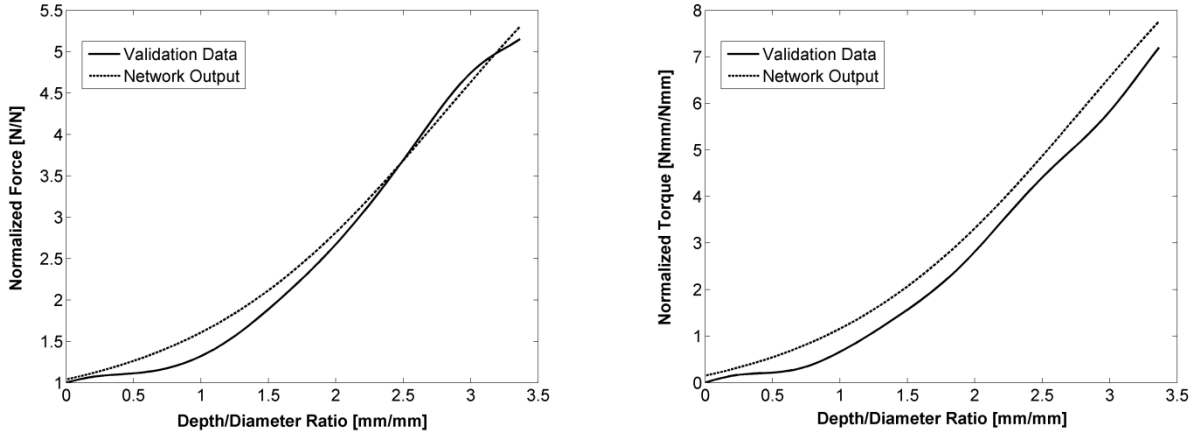

Figure 5-17: Trial two of the comparison of experimental validation data versus the predicted artificial neural network output for force and torque using a feed rate of 2.0mm/sec and spindle speed of 1500RPM.

5.6 Empirical Chip-Evacuation Model Calibration – Human Bone Drilling

Once it was established that chip-evacuation force and torque models could be developed for the drilling of bovine bone, it was decided to apply the same methodology in order to obtain similar models for the drilling of human bone. This would be advantageous since models calibrated via the drilling of human bone would provide a more realistic representation for use in orthopaedic haptic simulation systems.

Human femur bone specimens were provided by St. Michael's Hospital (Toronto, ON, CA) and were delivered in a similar condition as the bovine bones. Specifically, each bone had been cut mid-diaphysis in to approximately 2 inch segments as depicted in Figure 5-18. The human bones were stored in a freezer prior to experimentation in the same identical manner as the bovine bone specimens. A total of 16 left femur bone specimen were provided and their specifications including age, sex, and a variety material properties are provided in Table 5-9.

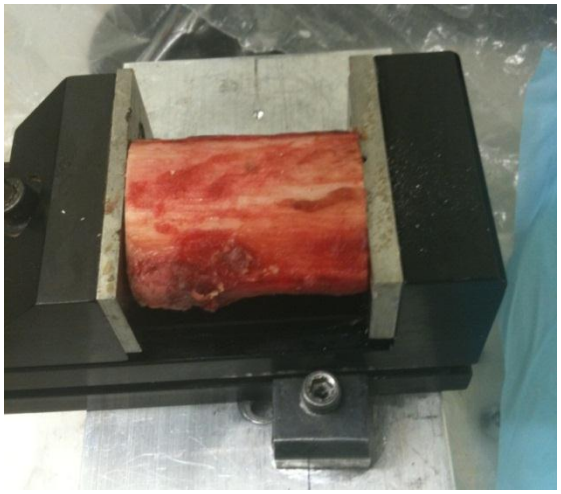

Figure 5-18: Human femur bone specimen loaded in to vice prior to experimentation.

The calibration experiments for the drilling of human bone were conducted in a similar manner as the experiments for the drilling of bovine bone outlined in Chapter 4. One difference was a slight change in the operating parameters. As was done for the experiments for the drilling of bovine bone, five sets of operating parameters within the typical range of orthopaedic surgery practices were selected from the literature [9, 13, 18]. These parameters are presented in Table 5-10. Experiments were conducted on the 16 bones using all 5 operating parameters for a total of 80 experiments.

Identification Code	Side	Gender	Age	Neck [g/cm^2]	Ward's [g/cm^2]	Trochanter [g/cm^2]	Total Bone Mineral Density (BMD) [g/cm^2]
M-6349	L	M	81	0.844	0.635	0.955	1.022
M-6134	L	M	93	0.804	0.591	0.771	0.843
F-64-08	L	F	43	1.078	0.971	1.016	1.196
F-14-08	L	F	70	0.689	0.455	0.668	0.789
F-22-09	L	F	79	0.556	0.333	0.544	0.669
F-18-09	L	F	80	0.748	0.505	0.705	0.866
F-12-09	L	F	70	0.859	0.619	0.777	0.952
F-11-09	L	F	75	0.470	0.318	0.547	0.638
F-10-09	L	F	72	0.749	0.476	0.793	0.917
F-09-09	L	F	62	0.993	0.739	0.855	1.042
F-08-09	L	F	73	0.850	0.670	0.746	0.927
F-66-08	L	F	87	0.720	0.542	0.721	0.902
1306	L	F	48	1.105	0.897	0.962	1.196
1304	L	M	67	1.051	0.800	1.039	1.163
1332	L	F	45	1.114	0.987	1.066	1.193
6238	L	F	79	0.880	0.584	0.863	0.999

Table 5-9: Specification data for each of the 16 human femur bone specimen used for experimentation.

Experiment #	Feed Rate (f) [mm/sec]	Spindle Speed (N) [RPM]
1	1.75	1000
2	1.75	1250
3	2.0	1000
4	2.0	1500
5	2.25	1500

Table 5-10: Experiment operating parameters used to calibration of the human bone drilling model.

After the data was collected, it was processed by normalizing and filtering as was done previously to the bovine bone data. A complete set of results for these experiments are available in Appendix C. As it can be seen for Figures C-6 to C-10 of Appendix C, the experimental data collected for the chip-evacuation force and torque for the drilling of human bone showed much larger variation than the data collected for the drilling of bovine bone. This can be attributed to the differing sex, age, weight, etc. of the donors.

A nonlinear least-squares optimization was performed on each data set using Eq. 4.4. This provided the optimized coefficients of friction, μ_f and μ_w, for the drilling of human bone. The results of this optimization for all 5 sets of operating parameters are presented in Table 5-11.

Feed Rate (f) [mm/sec]	Spindle Speed (N) [RPM]	μ_f	μ_w
1.75	1000	0.1491	1.6630
1.75	1250	0.0919	0.5581
2.0	1000	0.1538	1.0874
2.0	1500	0.0998	0.5209
2.25	1500	0.1692	2.4016

Table 5-11: The results of nonlinear least-squares optimization used to determine the coefficients of friction for the drilling of human bone for all calibration operating parameters.

The results presented in Table 5-11 display some variation in the trending of the μ_f and μ_w values. There are some trends that are similar to the trends seen in the drilling of bovine bone. As the spindle speed was increased while the feed rate remained constant, both coefficients of friction decreased. This was expected as discussed in Chapter 2. Additionally, as was seen during the drilling of bovine bone, as the feed rate increased while the spindle speed remained constant, the coefficient of friction between the drill flute and the bone chip, μ_f, increased. This trend was also expected since it was shown that the friction between the bone chip and the drill's flute is strongly dependent on the transverse velocity (feed rate).

With the determination of the coefficients of friction, the system of equations (Eqs. 4.8 and 4.9) were solved to yield the constants of the power law model. The results of these calculations are presented in Table 5-12.

i	0	1	2	3
a_i (μ_f)	63.4835	-102.7063	-9.1059	14.2482
b_i (μ_w)	193.8661	-290.1804	-27.1961	40.6326

Table 5-12: The constants of the power law model.

The power law constants presented in Table 5-12 can be substituted into Eq. 4.5 to yield:

$$\ln \mu_f = 63.4835 - 102.7063 \ln(f) - 9.1059 \ln(N) + 14.2482 \ln(f) \ln(N), \quad (5.8)$$

$$\ln \mu_w = 193.8661 - 290.1804 \ln(f) - 27.1961 \ln(N) + 40.6326 \ln(f) \ln(N). \quad (5.9)$$

Equations 5.8 and 5.9 can be used to determine the coefficients friction, μ_f and μ_w, for any feed rate, f, and spindle speed, N. Once the coefficients of friction have been calculated, they may be substituted back into Eqs. 3.16 and 3.19 to evaluate the chip-evacuation force and torque at any depth during the drilling of human bone, respectively.

5.7 Empirical Chip-Evacuation Model Validation – Human Bone Drilling

Because of the limited supply of human femur bone, a validation experiment using a single set of operating parameters was performed. As was done for the validation of the bovine bone drilling models, the parameters used to validate the human bone drilling models were selected as values different but with the same range as the ones which the models were calibrated. Specifically, a feed rate of 2.0mm/sec and a spindle speed of 1250RPM were the parameter selected to validate the human bone drilling models.

The validation experiments were run and the obtained data was processed as was done before. The results of two trials for chip-evacuation thrust force and torque are presented in Figures 5-19 and 5-20. In the same plots overlaying the experimental results are the functions generated by calibrated empirical model.

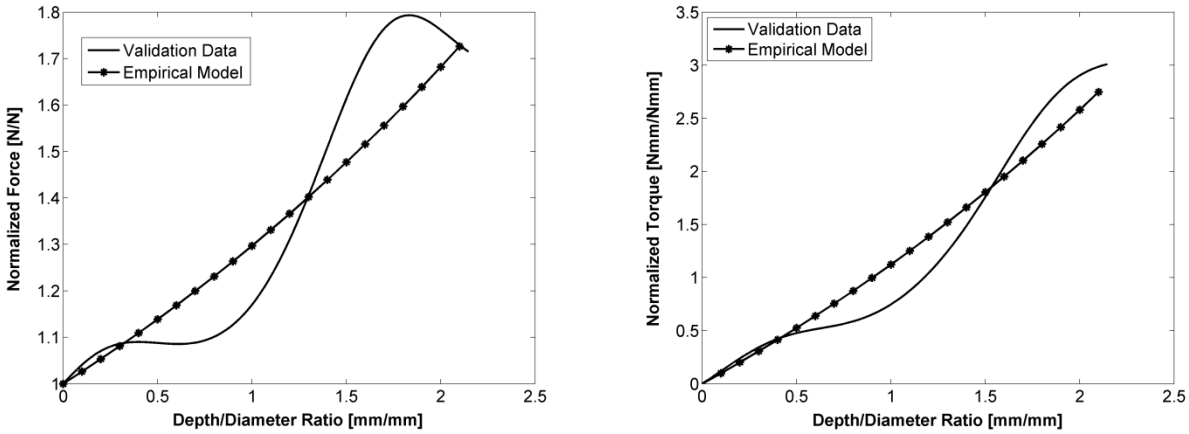

Figure 5-19: Trial one of the comparison of experimental validation data versus the predicted empirical model for force and torque using a feed rate of 2.0mm/sec and spindle speed of 1250RPM.

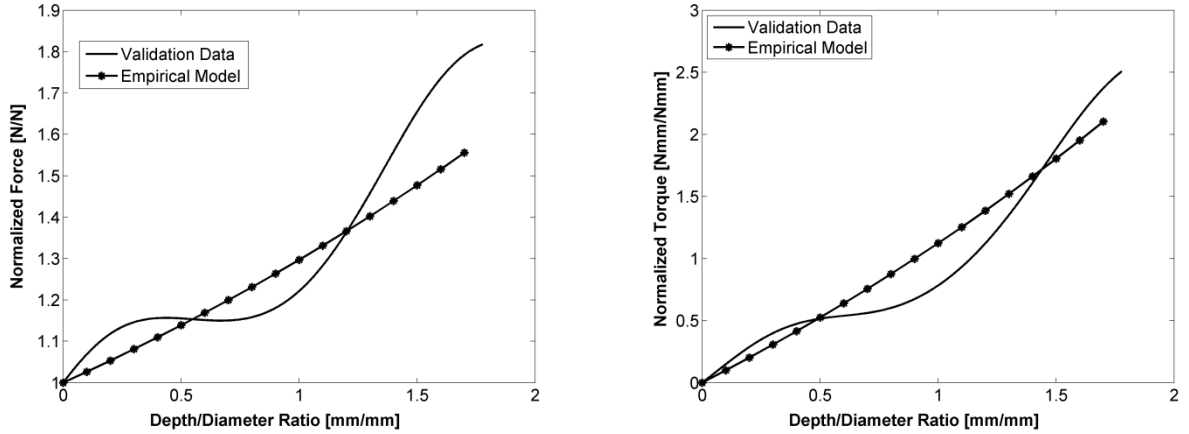

Figure 5-20: Trial two of the comparison of experimental validation data versus the predicted empirical model for force and torque using a feed rate of 2.0mm/sec and spindle speed of 1250RPM.

As can be seen in Figures 5-19 and 5-20, the calibrated empirical model for the drilling of human bone does well to approximate the chip-evacuation thrust force and torque. As was done with the validation for the drilling of bovine bone, the accuracy of the results for the drilling of human bone can be measured by calculating the coefficient of determination. The R-squared values comparing the force and torque validation data with the empirical model for both validation trials are presented in Table 5-13.

Feed Rate (*f*) [mm/sec]	**Spindle Speed (*N*) [RPM]**	**Trial #**	**R^2 for Force Model**	**R^2 for Torque Model**
2.0	1250	1	0.7415	0.9148
		2	0.6185	0.9035

Table 5-13: The coefficients of determination, R^2, for the force and torque models for each of the two validation experiments.

The results presented in Table 5-13 show that, although the empirical model does estimate the thrust force and torque for the drilling of human bone, there is some discrepancy between the experimental results and the output from the empirical model. This is more apparent with the force prediction model, having an average R-squared value of 0.6800, opposed to the torque prediction model which reported an average R-squared value of 0.9092.

This discrepancy can be attributed to the variation in material properties of the bones that were used for calibration and validation. As indicated in Table 5-9, the sex and age of the human bone donors varied quite a lot which would result in the overall strength and hardness of the bones to also vary significantly. This affects the consistency of the thrust force greatly as softer bones would require less force while harder bones would require more force. The chip-evacuation torque is not as greatly affected by this variation since it is more dependent on rotation velocity than material hardness. To eliminate this discrepancy, the bone specimens used for experimentation should have all been of the same sex and close in age. Unfortunately, this was not possible as the access to human bone specimens is limited and, thus, experiments could only be conducted on the samples that were provided. Although the empirical models show some inaccuracies, it can still be concluded that the models provide an acceptable approximation for the chip-evacuation thrust force and torque experienced during drilling of human bone.

5.8 Comparison of Results

With the calibration and validation of three models (two developed drilling bovine bone and one developed drilling human bone), this section will investigate the similarities and differences between them. Specifically, this section will compare the results of the empirical model versus the artificial neural network for the drilling of bovine bone, the results of the empirical model for the drilling of bovine bone versus the empirical model for the drilling of human bone, and how each of three compare to the currently used models from the literature.

5.8.1 Empirical Model versus Artificial Neural Network

Both the ANN and the empirical prediction models displayed excellent results during the validation process. An additional set of validation results were obtained in order to compare the methods directly. The experimental data was collected using a feed rate of 1.75mm/sec and a spindle speed of 1250RPM which represents one of the sets of parameters that both models were validated with. The raw experimental data for thrust force and torque were plotted and appear in Figure 5-21. Overlaying the experimental data in Figure 5-21 are the values obtained from the empirical and ANN models using the same above operating parameters.

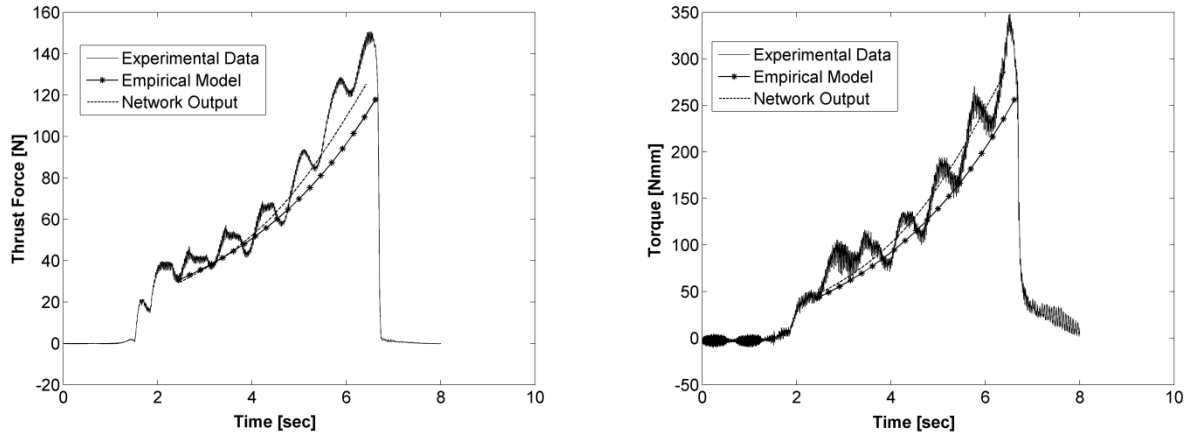

Figure 5-21: Raw experimental force and torque data with a comparision of the empirical model and ANN results.

The results presented in Figure 5-21 show that both the empirical and neural network models do well to predict the thrust force and torque when drilling bovine bone. In this particular example, it appears that the ANN provides a slightly better estimate for both force and torque. To

truly compare these models, it would be helpful to have them in the same empirical form. The following section will expand the neural network to allow for this comparison.

5.8.2 Drilling of Bovine Bone versus Drilling of Human Bone

The empirical models developed to predict the thrust force and torque while drilling bovine bone and human bone were calibrated independently using different bones. This makes the comparison of these models quite difficult since they cannot be shown together predicting the outcome of a single bone drilling operation. The best way to compare these models is to examine the differences in the results of the calibration and validation procedures and to discuss how these differences came to be.

The first point of interest is the coefficients of friction, μ_f and μ_w, obtained via calibration. The variation of the coefficient of friction between the bone chip and the drill's flute, μ_f, for the drilling of bovine bone is approximately 0.2112±0.0091. The coefficient of friction, μ_f, for the drilling of human bone was found to be approximately 0.1328±0.0346. These results suggest that μ_f for both models have relatively low variation and are increasing and/or decreasing appropriately with the increase/decrease of the feed rate and spindle speed. Additionally, the mean value of μ_f for the drilling of bovine bone is almost twice that of human bone. This implies that flow of bovine bone chips along the drill's flute encounters greater resistance than the flow of human bone chips.

The same comparison can be made regarding the coefficient of friction, μ_w. The variation of the coefficient of friction between the bone chip and the wall of the hole for the drilling of bovine bone is approximately 0.5826±0.0299. This is compared to the variation of μ_w obtained for the drilling of human bone which is approximately 1.2438±0.7986. These results suggest that coefficient of friction, μ_w, for the drilling of bovine bone has low variation and is increasing/decreases relative to the feed rate and spindle speed. In contrast, the variable μ_w for the drilling of human bone displays large variation and increases/decreases irregularly. Also, the mean value of μ_w for the drilling of human bone is over twice that of the mean value of μ_w when drilling bovine bone. This is the opposite that was seen when comparing the coefficient μ_f.

The comparison of these variations provides a very significant explanation as to why the model for the bovine bone validated very well where as the model for the human bone did not

validate nearly as well. As was mentioned earlier, the relatively poor correlation for the validation of the human bone model and the large variation in the friction coefficient, μ_w, can be attributed to the inconsistencies in material properties of the human bone specimens. The donors of the femur bones used for calibration and validation experiments varied between male and female and had large variation in age. This resulted in a large disparity of bone strength and hardness between specimens which was not present in the experiments involving the drilling of bovine bone. For these reason, it can be concluded that, although the presented models do sufficiently predict the chip-evacuation force and torque experience during the drilling of human bone, experiments conducted on specimens of the same sex and of similar age would have generated much more accurate results.

5.8.3 Empirical Model Comparisons to the Literature

The models developed were compared to those previously reported in the literature. Additional experimental data was collected for this comparison. The data was collected using a feed rate of 2.0mm/sec and a spindle speed of 1000RPM. Additionally, as all of the currently used models were developed via the drilling of animal bone, bovine bone was selected for this experiment. Lastly, as all of currently used models were developed empirically, only the presented empirical model for the drilling of bovine bone will be used as a comparison.

Of the force prediction models currently being used in orthopaedic haptic simulation systems, two were selected for this comparison. The two models that were chosen were Allotta [12] and Chi [15]. These force prediction models were selected because of their widely accepted use in current orthopaedic haptic simulation systems and their ease of implementation. The experimental data was collected and plotted alongside the proposed model, Allotta's model, and Chi's model. The result of this comparison appears in Figure 5-22.

As can be seen in the figure, the empirical model developed in this work is the only one that can mimic the clogging effect when drilling bone. Both Allotta and Chi's models do well to predict the initial cutting force but fail to capture the exponential increase in force that follows. This is because both models describe the thrust force as being constant once the initial cutting force is achieved. The experimental data displays a much different trend as drill flute clogging causes the force to increase with time.

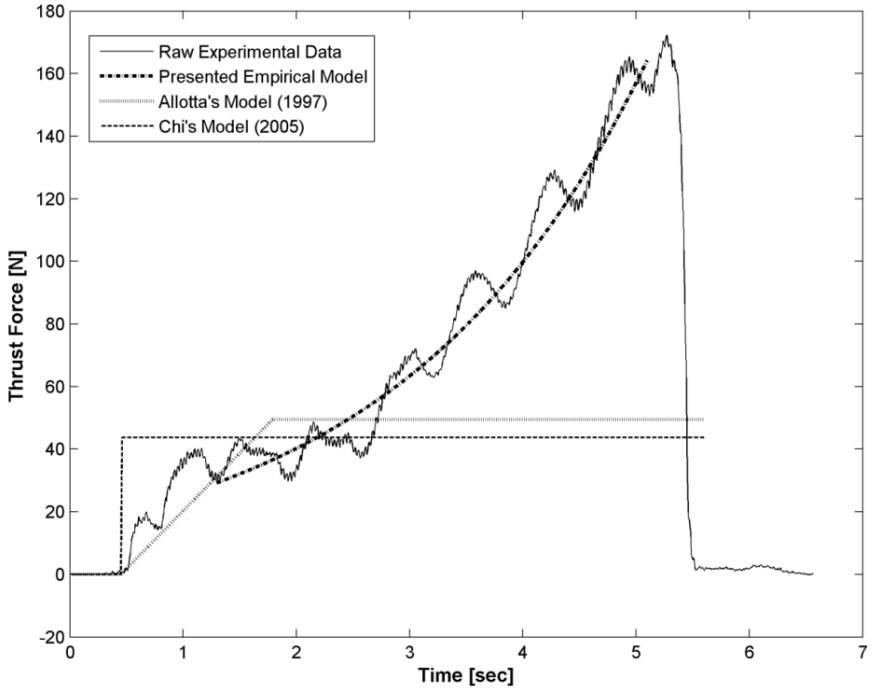

Figure 5-22: Plot comparing the experimental results of the drilling of bovine bone with the output of several thrust force prediction models.

5.9 Empirical Model Implementation into FEA Simulation

The proposed models were used as dynamic force and torque functions acting at various locations of a solid femur bone model. The resulting deflections and equivalent stresses were obtained. As a comparison, the solid model was then statically loaded using the thrust force and torque prediction models found in the literature. The resulting deflections and equivalent stresses for this loading were also obtained. The following are the results of this comparison.

5.9.1 FEA Simulation Solution and Post-Processing

The force and torque predictions from the developed models were used in the FEA simulation of a femur bone by adding a dynamic force and torque function to the three locations on the bone: mid-diaphysis, the proximal end, and the distal end. Similar to the conditions used for the model's calibration and validation experiments, only unicortical drilling of the femur was imposed using a feed rate of 2.0mm/sec and an assumed spindle speed of 1500RPM. The simulation time was set to 3 seconds which is the approximate time required to drill unicortical using a feed rate of 2.0mm/sec. Additionally, the simulation step size was set to 0.1 seconds which provided an acceptable 30 points of data without resulting in long computational wait

times. Figure 5-23 displays the results of this simulation for the maximum deflection experienced while drilling mid-diaphysis. Included in this figure is a screenshot of the physical deflection experienced by the simulated femur bone and a plot indicating this deflection as a function of drilling time.

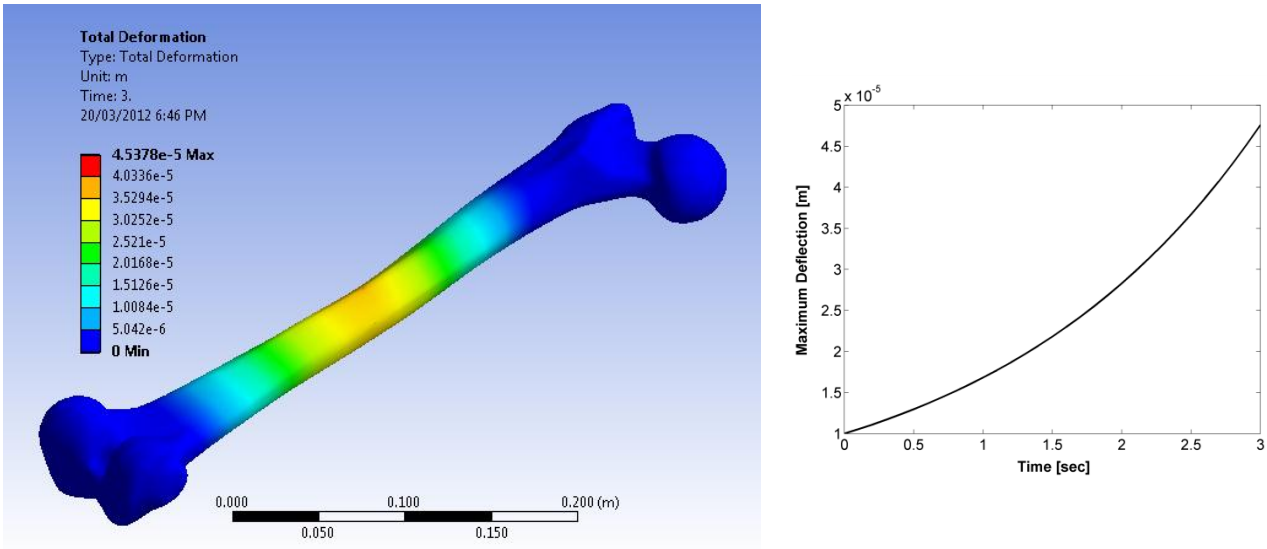

Figure 5-23: The result of the FEA simulation using the presented force and torque models while drilling mid-diaphysis.

As can be seen from Figure 5-23, the maximum deflection occurs at the location where the drill bit contacts the bone and was found to be approximately 0.0453mm. Also depicted in this figure is a plot displaying the maximum deflection as a function of time. This plot illustrates that the maximum deflection changes exponentially with time. This was expected since the presented deflection is a result of the exponential force and torque loading. As a comparison, Figure 5-24 displays the results of the same analysis using Allotta's force and torque formulations. As these functions are constant with respect to time, they were imposed in the simulation as static force and torque loads.

Figure 5-24 shows the maximum displacement experienced by the femur bone as a result of the static loading provided by Allotta's models. This was found to be 0.0095mm. Additionally, a plot depicting this deflection as a function of time is also presented in this figure. The results indicate that the maximum deflection experience by the bone as a result of dynamic loading is more than 4 times that of the deflection resulting from static loading. This difference is

significant. The maximum deflections for the three locations using the two models are presented in Table 5-14.

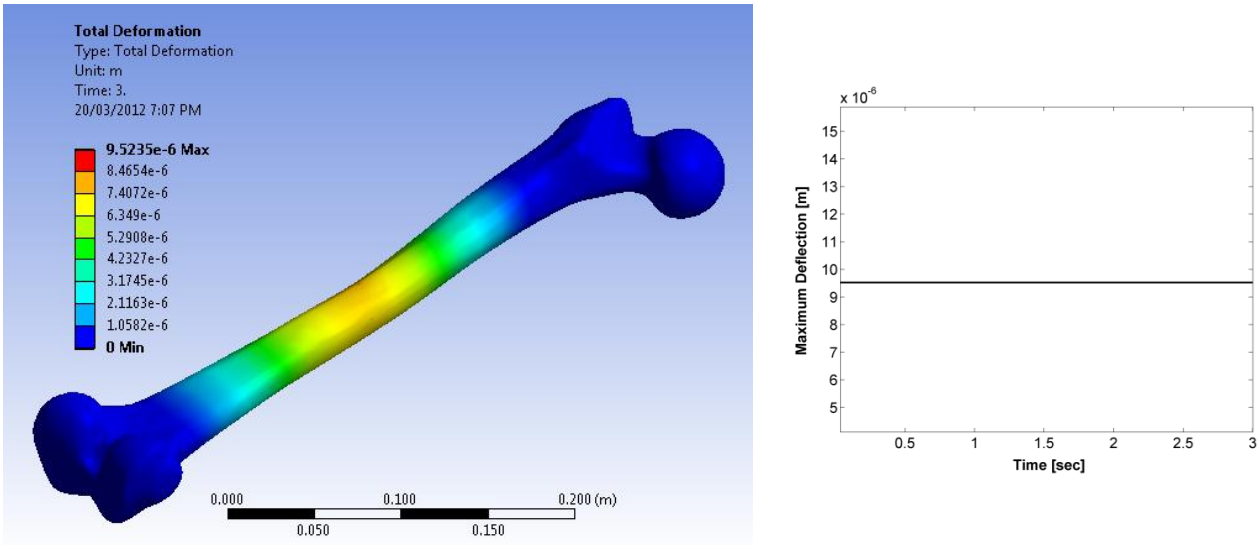

Figure 5-24: The result of the FEA simulation using Allotta's [12] force and torque models while drilling mid-diaphysis.

Simulations were also performed to obtain the equivalent or von-Mises stress due to the dynamic force and torque loading over the 3 second simulation time. The resulting maximum von-Mises stress was found to be 21.811MPa. A simulation was also run to obtain the equivalent stress due to the static force and torque loading. The results of this simulation revealed a maximum von-Mises stress of 4.581MPa. Plots of the resulting maximum equivalent stress as a function of time for each loading technique are provided in Figure 5-25.

Location on Bone	Maximum Deflection using Presented Models [mm]	Maximum Deflection using Allotta's Models [mm]
Mid-Diaphysis	0.04538	0.009524
Proximal End	0.006244	0.001312
Distal End	0.01252	0.002639

Table 5-14: The maximum deflection at the mid-diaphysis, proximal end, and distal end using the two models.

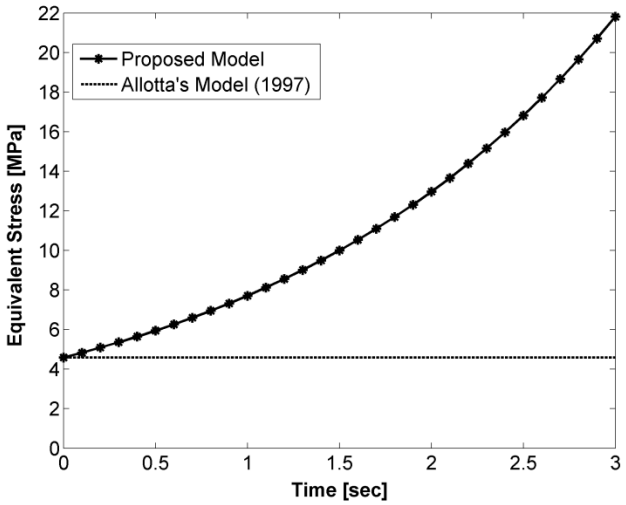

Figure 5-25: Plot of the resulting maximum equivalent stress comparing dynamic loading versus static loading.

As was the case with deflection, the plots in Figure 5-25 display the equivalent stress using the presented empirical model as exponentially increasing with time; on the contrary, the equivalent stress using Allotta's model is shown as being unchanged over time. Additionally, similar to the results obtained for deflection, the maximum equivalent stress resulting from the dynamic loading is almost 5 times greater than the maximum stress experienced when the femur bone is statically loaded. In both cases, the maximum stress is well below the point of failure but, with the inclusion of additional loading, bone damage or failure could occur and would be undetected in simulations using Allotta's model. Additional simulations were performed with the loads placed at the proximal and distal ends of the femur bone. The resulting maximum equivalent stresses for both loading methods are presented in Table 5-15.

Location on Bone	Maximum Equivalent Stress using Presented Models [MPa]	Maximum Equivalent Stress using Allotta's Models [MPa]
Mid-Diaphysis	21.8116	4.5813
Proximal End	0.3071	0.0642
Distal End	0.1856	0.0391

Table 5-15: The maximum equivalent stress at the mid-diaphysis, proximal end, and distal end using the two models.

6 Conclusion and Future Work

6.1 Summary of Contributions

The contributions of our research can be summarized as follows:

- Models developed for the drilling of metal were adopted and expanded to include the clogging effect experienced during the drilling of bone.
- Empirical formulations for the chip-evacuation thrust force and torque experienced while drilling bovine bone were calibrated and successfully validated.
- Artificial neural network models for the chip-evacuation thrust force and torque experienced while drilling bovine bone were fully trained and successfully validated.
- Empirical formulations for the chip-evacuation thrust force and torque experienced while drilling human bone were calibrated and successfully validated.
- A finite element simulation was conducted to determine the deflection and equivalent stress resulting from application of the proposed empirical model.

6.2 Concluding Remarks

Empirical chip-evacuation force/torque prediction models based on the force balance of a differential chip section were calibrated using a set of calibration experiments. Non-linear least squares regression, and a pair of power law equations was used to define the coefficients of friction, μ_f and μ_w in the model. The models were validated through additional experiments. An average R-squared value of 0.9546 validated the force prediction model and an average R-squared value of 0.9209 validated the torque prediction model. It was concluded that these models can predict the force and torque for the drilling of bovine bone.

Artificial neural network models were also constructed for predicting the force and torque seen during the drilling of bovine bone. The results of the validation procedure revealed high average R-squared values for both force (0.9692) and torque (0.9606).

The same empirical models that were established for the drilling of bovine bone were re-calibrated and validated through the drilling of human bone. It was shown through validation that these models obtained an average R-squared value 0.6800 for the force model and 0.9092 for the

torque model. It was concluded that the established models were acceptable for predicting the chip-evacuation force and torque for the drilling of human bone but more accurate results could have been obtained had greater control on specimen biological variations been employed.

It was found that the neural network model performed slightly better than the empirical model for a single comparison test. A comparison was made between the empirical model for drilling bovine bone with two models from the literature. This comparison showed that neither of the formulations taken from the literature was able to accurately predict the experimental thrust force.

The presented models were then incorporated into a finite element simulation to provide dynamic loading on a femur bone. These results were compared to those obtained using one of the static models from the literature. It was found that the deflection and equivalent stress were nearly five times greater when applying the dynamic loading of the presented models.

6.3 Future Work

Through this research it was discovered that there exists large variation in the results obtained for the drilling of both human and bovine bone. This was shown experimental as large sample populations were required for statistical model calibration for the drilling of both materials. The variations found in the results depend on many factors including age, weight, height, sex, etc. of the donor. It was shown through the drilling of bovine bone that, if these factors are kept relatively the same, the variations are minimal. On the contrary, it was shown through the drilling of human bone that, if these factors are not properly controlled, the variation of results can be rather large. Controlling these factors is possible during experimentation but is not always possible in real life applications. A more in-depth analysis could be conducted to determine if these variations can be quantified in some manner to allow for conclusions based on experimental results to translate more accurately to real life applications. A study of this nature specifically on the drilling of bone has yet to be published.

Appendix A – Basic Calculations

Calculating drill bit cone length:

$$l = \frac{D}{2}\left(\tan\frac{\beta}{2}\right)^{-1} = \frac{2.7}{2}\left(\tan\frac{90^{\circ}}{2}\right)^{-1} = 1.35\text{mm}. \quad \textbf{(A.1)}$$

Calculating drill flute cross-sectional area:

$$S = \frac{\pi\left(\frac{D}{2}\right)^{2} - A1}{2} = \frac{\pi\left(\frac{2.7}{2}\right)^{2} - 2.81}{2} = 1.46\text{mm}^{2}. \quad \textbf{(A.2)}$$

Calculating the angle formed between the flute face and the cutting plane:

$$\theta = \sin^{-1}\left(\frac{D5}{D4}\right) = \sin^{-1}\left(\frac{0.40}{0.89}\right) = 26.7^{o}. \quad \textbf{(A.3)}$$

Calculating degrees-of-freedom for use in Chi square hypothesis test [50]:

$$\text{Degrees-of-freedom} = j - 1 - k, \quad \textbf{(A.4)}$$

where j is the number of groups or bins and k is the number of parameters estimated from the data. Here, the data was discretized into 10 bins (j = 10) and the mean and standard deviation were estimated from the data (k = 2). Thus:

$$\text{Degrees-of-freedom} = 10 - 1 - 2 = 7. \quad \textbf{(A.5)}$$

Appendix B – Normality Test Data

Raw Normality Test Data:

Trial #	Exponential Constant (p)	Initial Cutting Force (F_o)
1	0.40046	21.587
2	0.552	19.919
3	0.42778	24.57
4	0.32302	26.962
5	0.57875	19.082
6	0.34081	26.935
7	0.41247	25.025
8	0.54535	21.546
9	0.51703	22.851
10	0.48991	23.716
11	0.48104	25.877
12	0.54411	23.848
13	0.48365	23.427
14	0.5057	23.98
15	0.59143	24.958
16	0.54135	22.973
17	0.43654	29.45
18	0.3879	28.668
19	0.50494	28.713
20	0.45055	27.886
21	0.56752	28.507
22	0.54958	23.769
23	0.51483	28.649
24	0.50203	25.708
25	0.18928	33.333
26	0.5482	26.579
27	0.58994	23.364
28	0.27149	31.635
29	0.38808	33.711
30	0.44399	23.355

Table B-1: The exponential constant, p, and the initial cutting force (F_o) for all normality test data.

Initial Cutting Force Standardized Data for Chi Square Test:

Trial #	Initial Cutting Force (F_o)	Standardized Force
1	21.587	-1.141000444
2	19.919	-1.605294737
3	24.57	-0.31067078
4	26.962	0.355151732
5	19.082	-1.838276946
6	26.935	0.347636177
7	25.025	-0.184019759
8	21.546	-1.152412953
9	22.851	-0.789161123
10	23.716	-0.548385005
11	25.877	0.053137758
12	23.848	-0.511642291
13	23.427	-0.62882928
14	23.98	-0.474899577
15	24.958	-0.20266947
16	22.973	-0.755201948
17	29.45	1.047696219
18	28.668	0.830023474
19	28.713	0.842549399
20	27.886	0.61235073
21	28.507	0.785208497
22	23.769	-0.533632249
23	28.649	0.82473475
24	25.708	0.00609595
25	33.333	2.128544386
26	26.579	0.248542191
27	23.364	-0.646365575
28	31.635	1.655899475
29	33.711	2.233762158
30	23.355	-0.64887076
Xbar = 25.6861		
Sigma = 3.592548998		

Table B-2: The initial cutting force and standardized cutting force used for a Chi Square test for normality.

Exponential Constant Standardized Data for Chi Square Test:

Trial #	Exp Constant (*p*)	Standardized Exponential Constant
1	0.40046	-0.705393356
2	0.552	0.84686605
3	0.42778	-0.425548252
4	0.32302	-1.498629257
5	0.57875	1.120872511
6	0.34081	-1.316402156
7	0.41247	-0.582372137
8	0.54535	0.778748556
9	0.51703	0.48866022
10	0.48991	0.210863763
11	0.48104	0.120006294
12	0.54411	0.766046948
13	0.48365	0.14674113
14	0.5057	0.3726044
15	0.59143	1.250756695
16	0.54135	0.737775627
17	0.43654	-0.335817539
18	0.3879	-0.834048352
19	0.50494	0.364819543
20	0.45055	-0.192309856
21	0.56752	1.005841014
22	0.54958	0.822077428
23	0.51483	0.46612511
24	0.50203	0.335011738
25	0.18928	-2.86855913
26	0.5482	0.807941768
27	0.58994	1.235494279
28	0.27149	-2.026463011
29	0.38808	-0.83220457
30	0.44399	-0.259505459
Xbar = 0.469324333		
Sigma = 0.097625435		

Table B-3: The exponential constant, p, and standardized exponential constant used for a Chi Square test for normality.

Appendix C – Experimental Data

Processed Experimental Bovine Bone Data Sets with Outliers Removed:

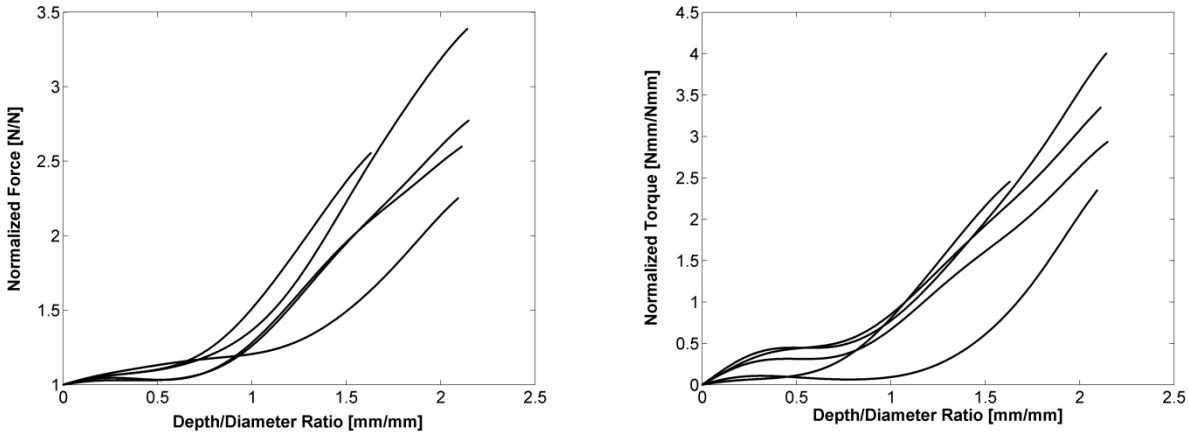

Figure C-1: Processed experimental data for the drilling of bovine bone using a feed rate of 1.0mm/sec and a spindle speed of 1000RPM.

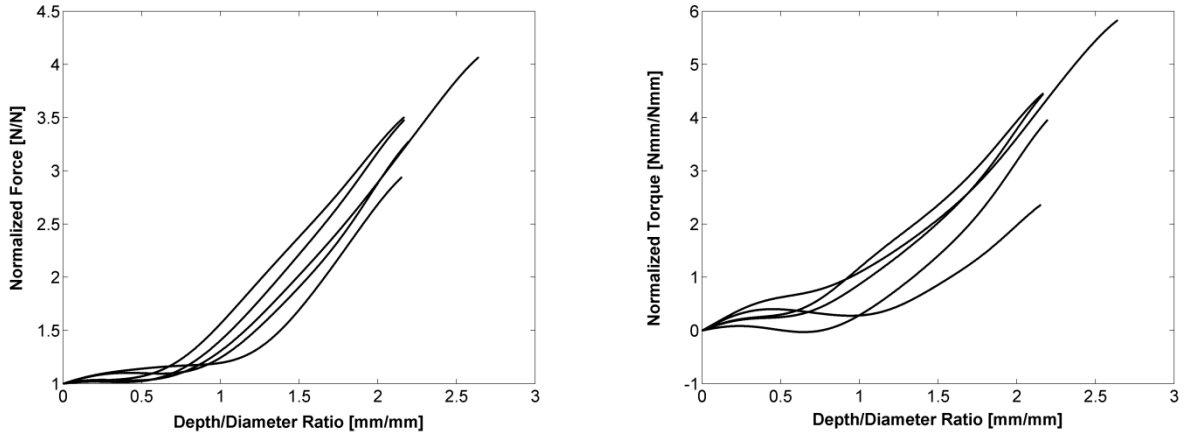

Figure C-2: Processed experimental data for the drilling of bovine bone using a feed rate of 1.5mm/sec and a spindle speed of 1100RPM.

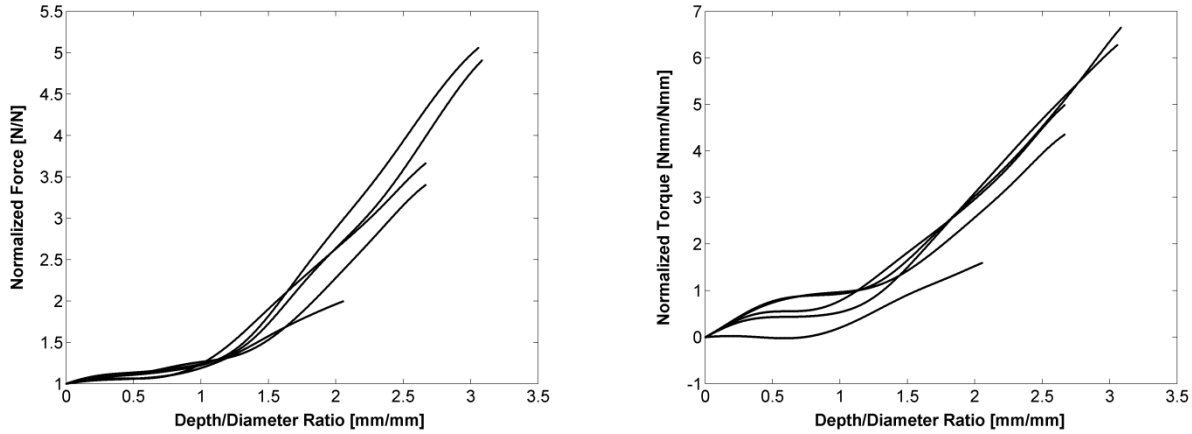

Figure C-3: Processed experimental data for the drilling of bovine bone using a feed rate of 1.5mm/sec and a spindle speed of 1250RPM.

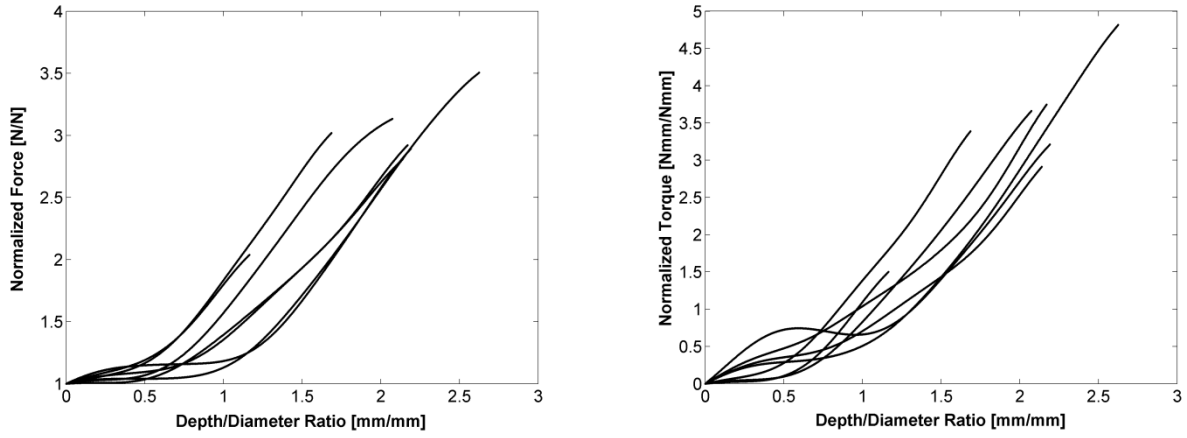

Figure C-4: Processed experimental data for the drilling of bovine bone using a feed rate of 1.75mm/sec and a spindle speed of 1500RPM.

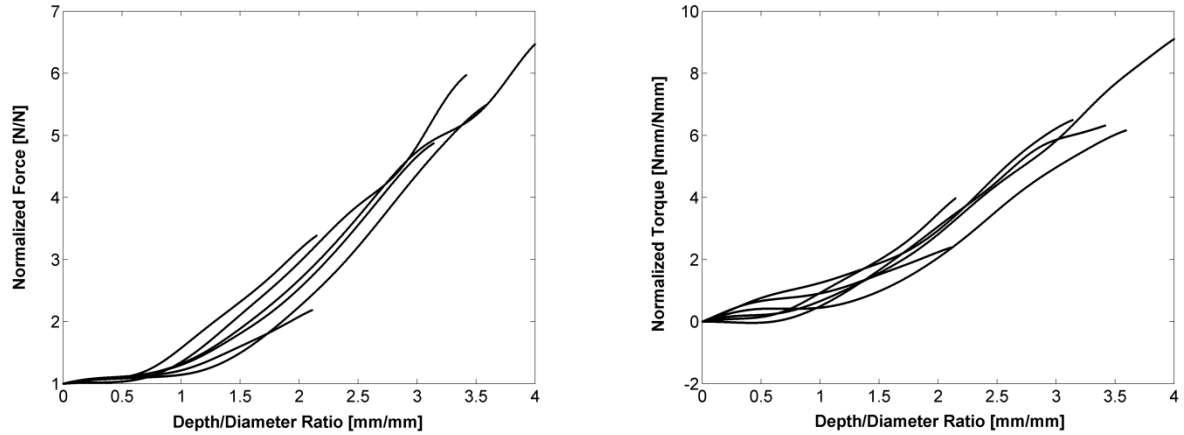

Figure C-5: Processed experimental data for the drilling of bovine bone using a feed rate of 2.0mm/sec and a spindle speed of 1500RPM.

Processed Experimental Human Bone Data Sets with Outliers Removed:

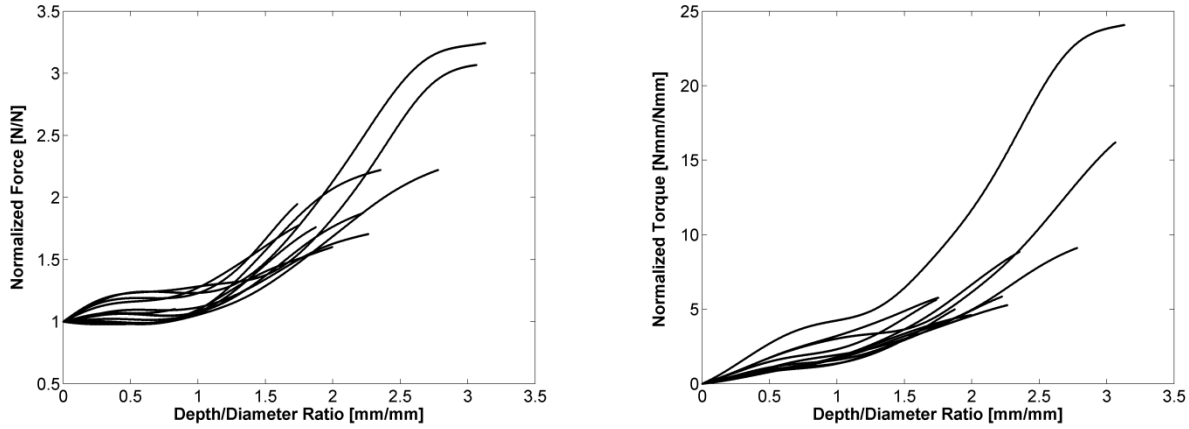

Figure C-6: Processed experimental data for the drilling of human bone using a feed rate of 1.75mm/sec and a spindle speed of 1000RPM.

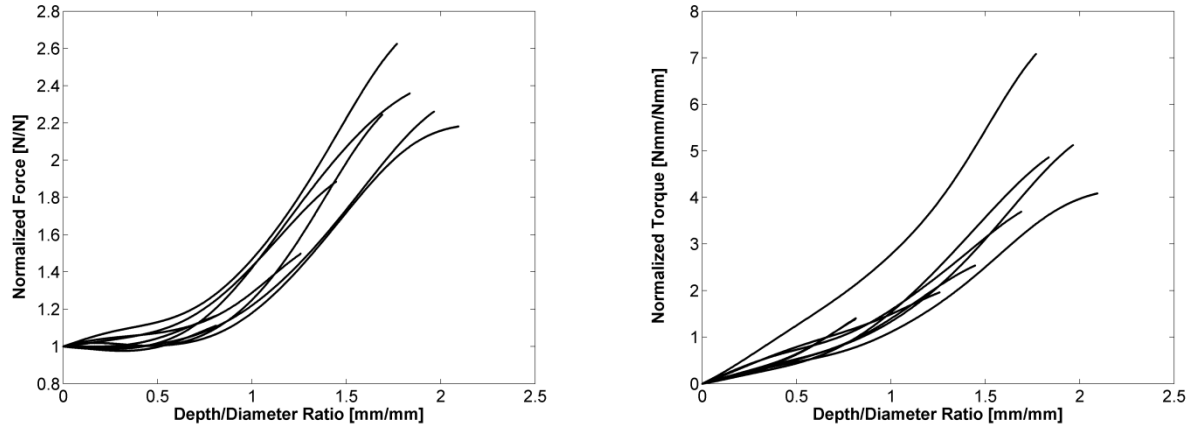

Figure C-7: Processed experimental data for the drilling of human bone using a feed rate of 1.75mm/sec and a spindle speed of 1250RPM.

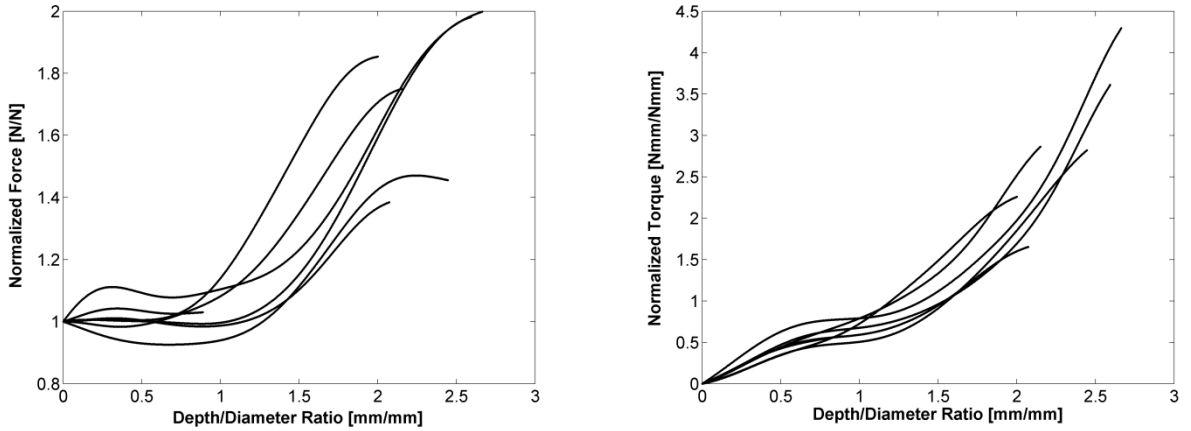

Figure C-8: Processed experimental data for the drilling of human bone using a feed rate of 2.0mm/sec and a spindle speed of 1000RPM.

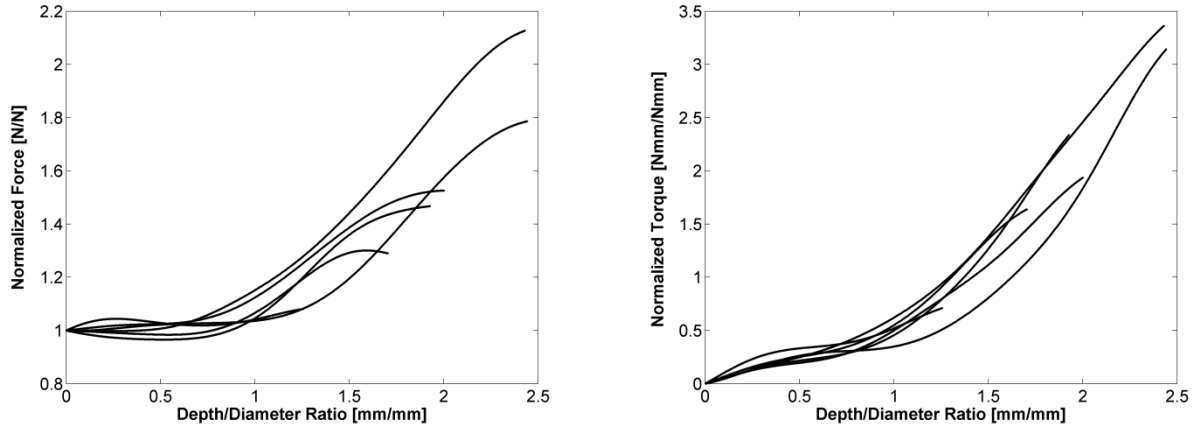

Figure C-9: Processed experimental data for the drilling of human bone using a feed rate of 2.0mm/sec and a spindle speed of 1500RPM.

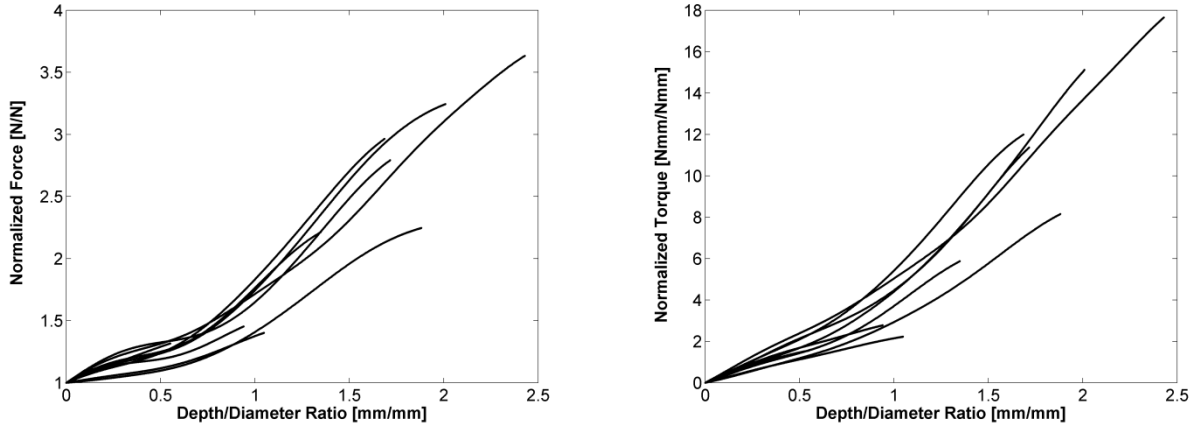

Figure C-10: Processed experimental data for the drilling of human bone using a feed rate of 2.25mm/sec and a spindle speed of 1500RPM.

References

[1] Elstrom, J.A., Virkus, W.W., and Pankovich, A.M. (2006). *Handbook of Fractures*: 3rd Ed. New York: McGraw-Hill, 264–313.

[2] Marti, A., Fankhauser, C., Frenk, A., Cordey, J., Gasser, B. (2001). Biomechanical evaluation of the less invasive stabilization system for the internal fixation of distal femur fractures. *Journal of Orthopaedic Trauma* 15(7), 482–487.

[3] Prayson, M.J., Datta, D.K., Marshall, M.P. (2001). Mechanical comparison of endosteal substitution and lateral plate fixation in supracondylar fractures of the femur. *Journal of Orthopaedic Trauma* 15(2), 96–100.

[4] Booth, K.C., Donaldson, T.K. Dai, Q.G. (1998). Femoral neck fracture fixation: a biomechanical study of two cannulated screw placement techniques. *Orthopedics* 21(11), 1173–1176.

[5] Uhl, R.L. (1989). The biomechanics of screws. *Journal of Orthopaedic Research* 18(12), 1302–1307.

[6] Powers M.J. (2006). *The Mechanics of Bone Drilling: Experiment and Finite Element Predictions*, PhD thesis, University of Calgary, Canada.

[7] Kincaid, J. P., & Westerlund, K.K. (2009). Simulation in education and training. In: *Proceedings of the 2009 Winter Simulation Conference*, edited by M. D. Rossetti, R. R. Hill, B. Johansson, A. Dunkin, and R. G. Ingalls, Piscataway, New Jersey, 273-280.

[8] Hsieh, M. S., Tsai, M. D., & Yeh, Y. D. (2006) An amputation simulator with bone sawing haptic interaction. *Applications Basis and Communications* 18(5), 229–236.

[9] Wiggins, K. L. & Malkin, S. (1976). Drilling of bone. *Journal of Biomechanics* 9(9), 553-559.

[10] Shaw, M. C. & Oxford, C. J. JR. (1957). On the drilling of metals 2: the torque and thrusting drilling. *Transactions of the ASME* 1(79), 139-148.

[11] Cook, N. H. (1966). *Manufacturing Analysis*. Redding, Massachusetts: Addison-Wesley.

[12] Allotta, B., Giacalone, G., & Rinaldi, L. (1997). A hand-held drilling tool for orthopedic surgery. *IEEE/ASME Transactions on Mechatronics* 2(4), 218-229.

[13] Jacob, C. H., Berry, J. T., Pope, M. H., & Hoaglund, F. T. (1976). A study of the bone machining process – drilling. *Journal of Biomechanics* 9(5), 343-349.

[14] Peng, X., Chi, X., Ochoa, J. A., & Lew, M. C. (2003). Bone surgery simulation with virtual reality. In: *ASME 2003 Design Engineering Technical Conferences and Computers and information in Engineering Conference*, Chicago, Illinois, 1105-1113.

[15] Chi, X., Niu, Q., Thakkar, V. S. & Leu, M. C. (2005). Development of a bone drilling simulation system with force feedback. In: *Proceeding of ASME 2005 International Mechanical Engineering Congress and Exposition*, Orlando, Florida, 83-89.

[16] Tsai, M. D., Hsieh, M. S., & Tsai, C. H. (2007). Bone drilling haptic interaction for orthopedic surgical simulator. *Computers in Biology and Medicine* 37(12), 1709-1718.

[17] Niu, Q., Chi, X., Leu, M. C., & Ochoa, J. A. (2008). Image processing, geometric modeling and data management for development of a virtual bone surgery system. *Computer Aided Surgery* 13(1), 30-40.

[18] Chi, X., Niu, Leu, M. C., & Ochoa, J. A. (2004). Modeling of haptic rendering for virtual bone surgery. In: *Proceeding of ASME 2004 International Mechanical Engineering Congress and Exposition*, Anaheim, California, 139-146.

[19] Esen, H., Yano, K., & Buss, M. (2004). A virtual environment medical training system for bone drilling with 3 DOF force feedback. In: *Proceedings of the 2004 IEEE/RSJ International Conference on Intelligent Robots and Systems*, Sendai, Japan, 3631-3636.

[20] Agus, M., Giachetti, A., Gobbetti, E., Zanetti, G., & Zorcolo, A. (2003). Real-time haptic and visual simulation of bone dissection. *Presence: Teleoperators and Virtual Environments*, 12(1), 110-122.

[21] Vankipuram, M., Kahol, K., McLaren, A., & Panchanathan, S. (2010). A virtual reality simulator for orthopedic basic skills: a design and validation study. *Journal of Biomedical Informatics*, 43(5), 661-668.

[22] Goldstein, S. A. (1987). The mechanical properties of trabecular bone: dependence on anatomic location and function. *Journal of Biomechanics* 20(11-12), 1055-1061.

[23] Hall, S. (2007). *Basic Biomechanics*, 5th Ed. Boston: McGraw Hill, pp. 88.

[24] Curry, J. (1998). *Handbook of Biomaterial Properties*. London: Chapman & Hall, pp. 3-14.

[25] Keaveny, T. M. (1998). *Handbook of Biomaterial Properties*. London: Chapman & Hall, pp. 15-23.

[26] Armarego, E. J. A., & Brown, R. H. (1969). *Machining of Metals*. Englewood Cliffs, New Jersey: Prentice-Hall.

[27] Image of orthogonal cutting. Retrieved September 21st, 2011, from: http://engineeronadisk.com/notes_manufact/cuttinga7.html

[28] Strenkowski, J. S., Hsieh, C.C., & Shih, A. J. (2004). An analytical finite element technique for predicting thrust force and torque in drilling. *International Journal of Machine Tools and Manufacture* 44(12-13), 1413-1421.

[29] Mellinger, J.C., Ozdoganlar, O.B., DeVor, R.E., & Kapoor, S.G. (2002). Modeling chip-evacuation forces and prediction of chip clogging in drill. *Journal of Manufacturing Science and Engineering* 124(3), 605-614.

[30] Hobkirk, J. A., & Rusiniak, K. (1977). Investigation of variable factors in drilling bone. *Journal of Oral Surgery* 35(12), 968-973.

[31] Karalis, T. & Galanos, P. (1982). Research on the mechanical impedance of human bone by a drilling test. *Journal of Biomechanics* 15(8), 561-581.

[32] Abouzgia, M. B. & James, D. F. (1995). Measurements of shaft speed while drilling through bone. *Journal of Oral Maxillofacial Surgery* 53(11), 1308-1316.

[33] Subramanian, K., & Cook, N. H. (1977). Sensing of drill wear and prediction of drill life. *Journal of Engineering for Industry - Transaction of ASME* 99(2), 295–301.

[34] Morin, E., Masounave, J., & Laufer, E.E. (1995). Effect of drill wear on cutting forces in the drilling of metal-matrix composites. *Wear* 184(1), 11-16.

[35] Augustin, G., Zigman, T., Dalvila, S., Udilljak, T., Staroveski, T., Brezak, D., & Babic, S. (2011). Cortical bone drilling and thermal osteonecrosis. *Clinical Biomechanics* in press.

[36] Tadmor, Z., & Gogos, C. (1979). *Principles of Polymer Processing*. New York: Wiley.

[37] Long, W. M. (1960). Radial pressures in powder compaction. *Powder Metallurgy* 1(6), 73-86.

[38] Reddy, J.N. (1988). *The Finite Elements Analysis for Engineering Design*, New York: Springer-Verlag.

[39] Zdero, R., Keast-Butler, O., Schemitsch, E.H., (2010). A biomechanical comparison of two triple-screw methods for femoral neck fracture fixation in a synthetic bone model, *Journal of Trauma*, [Epub ahead of print].

[40] Holmes, C.A., Edwards, W.T., Myers, E.R., Lewallen, D.G., White, A.A. (1993). Biomechanics of pin and screw fixation of femoral neck fractures. *Journal of Orthopaedic Trauma*, 7(3), 242–247.

[41] Kauffman, J.I., Simon, J.A., Kummer, F.J., Pearlman, C.J., Zuckerman, J.D., Koval, K.J. (1999). Internal fixation of femoral neck fractures with posterior comminution: a biomechanical study. *Journal of Orthopaedic Trauma*, 13(3), 155–159.

[42] Blair, B., Koval, K.J., Kummer, F., Zuckerman, J.D. (1994) Basicervical fractures of the proximal femur: a biomechanical study of 3 internal fixation techniques. *Clinical Orthopaedics and Related Research*, 306(1), 256 –263.

[43] Aminian, A., Gao, F., Fedoriw, W.W., Zhang, L.Q., Kalainov, D.M., Merk, B.R. (2007) Vertically oriented femoral neck fractures: mechanical analysis of four fixation techniques. *Journal of Orthopaedic Trauma*, 21(8), 544 –548.

[44] Baitner, A.C., Maurer, S.G., Hickey, D.G., et al. (1999) Vertical shear fractures of the femoral neck. A biomechanical study. *Clinical Orthopaedics and Related Research*, 367(1), 300–305.

[45] Springer, E.R., Lachiewicz, P.F., Gilbert, J.A. (1991) Internal fixation of femoral neck fractures: a comparative biomechanical study of Knowles pins and 6.5-mm cancellous screws. *Clinical Orthopaedics and Related Research*, 267(1), 85–92.

[46] Stankewich, C.J., Chapman, J., Muthusamy, R., et al. (1996) Relationship of mechanical factors to the strength of proximal femur fractures fixed with cancellous screws. *Journal of Orthopaedic Trauma*, 10(4), 248 –257.

[47] Model 2000/2010 Deluxe 8-Direction Mill, Sherline Products Inc. Available at: http://www.sherline.com/2000pg.htm

[48] Force/Torque Installation and Operation Manual, ATI Industrial Automation. Available at: http://ati-ia.com

[49] Sedlin, E. D., & Hirsch, C. (1966). Factors affecting the determination of the physical properties of femoral cortical bone. *Acta Orthopaedica Scandinavica* 37(1), 29-48.

[50] Rosner, B. (2006). *Fundamentals of Biostatistics*, 6th Ed. Belmont, California: Duxbury, 125-134.

[51] Huiskes, R., & Van Rietbergen. (2005) *Biomechanics of Bone In: Basic Orthopaedic Biomechanics and Mechano-Biology*: Third Edition, V.C. Mow and R. Huiskes (Eds.), Lippincott Williams and Wilkins, Philadelphia, PA, 123-179.

[52] Nise, N. S. (2008). *Control Systems Engineering*. Hoboken (NJ): John Wiley & Sons, Inc.